Master's Thesis

Computational Science and Engineering

École Polytechnique Fédérale de Lausanne

Politecnico di Milano

European Space Agency

Galactic Cosmic Rays Characterization with ESA Planetary Missions

Author:
Thomas Rimbot
(thomas.rimbot@epfl.ch)
(thomas.rimbot@outlook.com)

Supervisors:
Dr. Olivier Witasse (ESA)
Pr. Martin Jaggi (EPFL)
Pr. Luca Formaggia (PoliMi)

Acknowledgements

Abstract

Galactic cosmic rays (GCRs) represent a major challenge for space exploration. Composed of highly energetic charged particles, they can cause damage to electronics devices and biological systems, motivating the need of designing efficient spacecraft shielding and astronaut suits. This work presents two ways of characterizing GCRs fluxes with observations from ESA planetary missions. In a first part, focus is set on a dedicated radiation monitoring instrument: the RADiation-hard Electron Monitor (RADEM) onboard the JUICE spacecraft. Simulations are run using a particle-through-matter modeling framework to characterize the Heavy-Ion Detector Head (HIDH)'s response to particle fluxes. In particular, the instrument's field of view, geometric factors and estimated count rates are derived. In a second part, the use of engineering data for GCRs characterization is investigated with the *Venus Express* mission. This data comes from the error detection and correction system which responds to highly energetic charged particles hitting the spacecraft's memory devices. This work proposes a first-of-a-kind analysis of GCRs at Venus over a long period of time and demonstrates the use of this data in its characterization by correlation analysis. In particular, the results suggest a near-instantaneous effect of the solar activity on GCRs fluxes close to the Sun.

Contents

Figure 1: Artist's impression of the JUICE spacecraft in the Jovian system, consisting of the four Galilean moons Io (left), Europa (far right), Ganymede (top right) and Callisto (bottom left). Credit: Artist M. Caroll.

1   Introduction

Space exploration is one of the major current and future challenges of humanity. The *European Space Agency* (ESA) and national space agencies like the *National Aeronautics and Space Administration* (NASA) launch regular missions to push the limits of human knowledge, answer long asked scientific questions and develop engineering technologies; and private companies like *SpaceX* aim at colonizing other planets in the next decades. This master thesis has been conducted in collaboration between École Polytechnique Fédérale de Lausanne (EPFL), Politecnico di Milano (PoliMi) and ESA. During this 6-months work, two major scientific ESA missions have been launched: *JUpiter ICy moons Explorer* (JUICE) [11], dedicated to the characterization of the icy moons of Jupiter and their possible habitability; and EUCLID, which will map the universe in search of dark matter and dark energy. Manned missions are also represented in the current scientific scenery, as 2022 marked the beginning of the *Artemis* program, aiming at reestablishing human presence on the moon after the last *Apollo 17* mission in 1972. Finally, space stations such as the *International Space Station* (ISS) are orbital laboratories enabling permanent human presence in space.

The space environment is harsh in multiple aspects. A non-exhaustive list includes extreme positive and negative temperatures (JUICE will experience temperatures from $-230°$ C to $+250°$ C), various size debris dangerous for any spacecraft or human, and ultra-vacuum. These make space exploration extremely hazardous. Another aspect to consider is radiation. On Earth, the atmosphere absorbs or reflects most of the radiation that is deadly to humans, allowing life to thrive. In space and to varying degrees on other planets, no such natural protection is present. Thus, careful understanding of the space radiation environment is necessary to design appropriate counter-measures for astronauts and spacecrafts. Several sources contribute to the radiation environment with a wide variety of charged particle species. At the high-end of the energy spectrum are particles coming from *Galactic Cosmic Rays* (GCRs). They originate from galaxies and, depending on their properties, can penetrate our solar system [2]. Because of their high energy, they are particularly hazardous to electronics systems and humans, thus motivating the need to accurately characterize them [45].

In order to characterize galactic cosmic rays and the space radiation environment in general, some spacecrafts carry *radiation monitors*. These instruments are built to detect high energy charged particles with specialized detectors. Processing the resulting data allows to understand the environment around the spacecraft. As the mission JUICE has just been launched on April 14th 2023, its radiation monitor, the *RADiation-hard Electron Monitor* (RADEM) [50], should be accurately characterized for future studies. It is composed of four detector heads which will be further described in the relevant sections. One of them, the *Heavy-Ion Detector Head* (HIDH), was not studied yet. The main goal of this project was to run simulations of particle interactions with the HIDH and analyse the resulting data to characterize the detector's properties. This implied simulating GCRs fluxes to identify their most abundant elements, developing a first order computation framework to better understand the underlying processes of particles-detector interactions, and running advanced simulations with a dedicated software (`Geant4` [17, 18, 26]) to characterize the detector's properties in multiple settings. The main parameters of interest were the detector's lower thresholds, which give a lower bound on the deposited energy of a particle interacting with the detector to register the hit. This allowed to describe the effect of these lower thresholds on the detector's geometric factors and count rates for GCRs fluxes. The analysis was done following the principles used to characterize another radiation monitor, the *BepiColombo Environment Radiation Monitor* (BERM) onboard the *BepiColombo* spacecraft targeting Mercury [23]. These will be detailed in the relevant section in this thesis.

Another focus of this work was the use of engineering parameters in GCRs characterization at Venus. These parameters are the *Error Detection And Correction* (EDAC) cumulative counters, used for detection and correction of errors induced by highly energetic charged particles hitting a spacecraft's memory devices. It had already been demonstrated in [37] that the slope of this counter exhibits a clear anti-correlation with the *SunSpots Number* (SSN) for *Mars Express* and *Rosetta* data. This is of particular importance because GCRs are known to be anti-correlated with the solar activity, hence suggesting that EDAC slopes actually correlate with GCRs intensity variation. In this study, these results are reproduced on *Venus Express* data, validating the anti-correlation of EDAC slopes with the solar activity. This procedure is also further investigated and used to show that these results imply a near-instantaneous influence of solar modulation on cosmic rays fluxes at Venus. As long duration radiation data at Venus is not available to this day, this work represents one of the first characterization of galactic cosmic rays so close to the Sun over a long period of time.

This thesis is structured as follows. In section 2, the theoretical framework needed to develop this study is detailed. It gives a general overview of the space radiation environment with its three main contributors: galactic cosmic rays, solar energetic particles and trapped particles. The relevant ESA missions are then introduced, followed by the theoretical foundation of particles-detector interactions for radiation monitoring in space. The following two sections are dedicated to radiation monitoring with JUICE: section 3 presents the numerical tools and modeling approach used and developed, from GCRs fluxes simulations to RADEM measurements and data analysis, and section 4 presents the results of these simulations and how they were used to characterize the detector's properties. The second part of this project is then developed in section 5, which is dedicated to the characterization of GCRs at Venus using EDAC data and describes the whole data processing and analysis required for this part. Conclusions and final thoughts are discussed in section 6.

2   Theoretical framework

This section presents the theoretical framework needed to investigate the datasets used in this work. Its objective is to define all the terms in the title of the thesis. First, the main object of interest, galactic cosmic rays, is introduced together with a general description of the space radiation environment. Then, the relevant missions are described: *JUpiter ICy moons Explorer* (JUICE), *Venus Express*, *Mars Express* and *Rosetta*, with the focus set on JUICE as it represents the main mission of interest in this project and the work conducted at ESA. Finally, the analysis part is introduced, with elements of radiation monitoring and the error detection algorithm used for GCRs characterization with *Venus Express*.

2.1   Space radiation environment

This project proposes to characterize galactic cosmic rays by analyzing data obtained by planetary missions. However, cosmic rays are just a part of the space radiation environment which is actually a result of various sources, both local and external. The three main contributors are galactic cosmic rays, solar particle events and trapped particles. This diversity of processes creates a rich environment which can be very harsh on electronics and biological systems because of the large range of particles, their deposited energy density and their flux. Electrons, protons and ions populating the radiation environment span a wide energy range, from 10^5 eV[1] for plasma to 10^{20} eV for the most energetic cosmic rays [9]. Figure 2 summarizes the particles and energies of the space radiation environment.
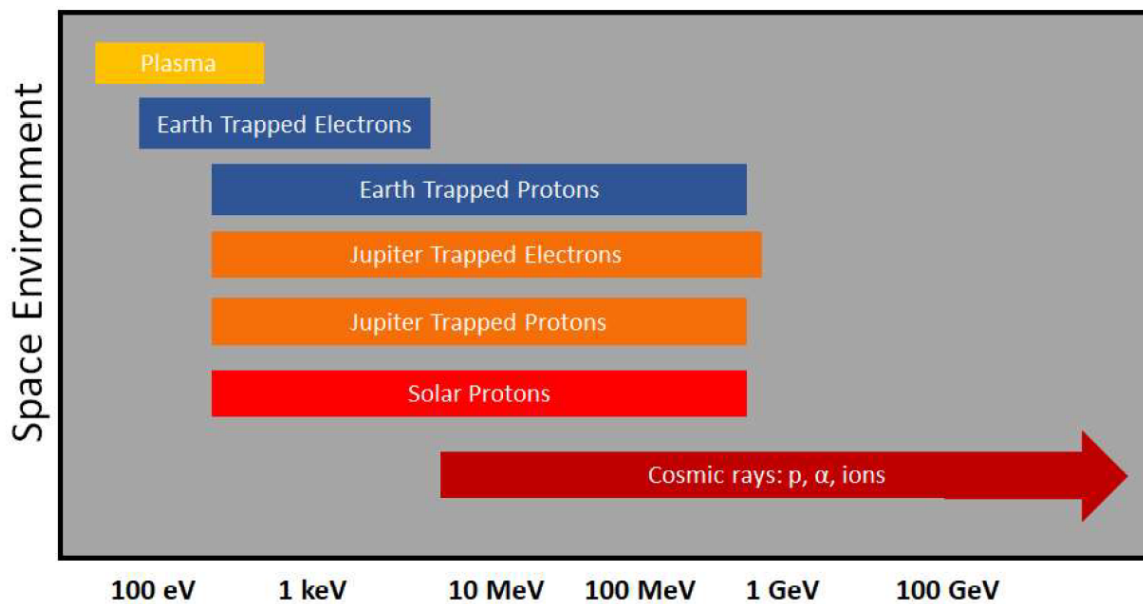
Figure 2: Space radiation environment around Earth, Jupiter and the Sun with typical energy ranges. Credits: [50, 54].

This subsection describes the three main radiation sources in space, with emphasis on their origin and effects at Earth and Jupiter.

---

[1]$1eV = 1.602 \times 10^{-19}$J

2.1.1 Galactic cosmic rays

At the high-end of the energy spectrum, *Galactic Cosmic Rays* (GCRs) are a major contributor to the space radiation environment. Figure 3 reports the composition of a GCRs flux measured by several experiments. Each line represents the abundance of a particular element. It can be seen that the flux consists mostly of protons and Helium ($z = 2$) nuclei [24], but heavier ions with $z > 2$ are also present with varying abundance [61]. While their origin is not perfectly understood, it is thought that GCRs emanate from supernova remnants resulting from powerful star explosions in distant galaxies [2]. They are then accelerated and propagated through the space medium and may cross our Solar System.

The GCRs flux is nearly constant and isotropic, but relatively low compared to other sources. It is estimated around 4 particles/cm^2/s in space [50] against the constant background flux of 2×10^8 particles/cm^2/s from solar wind particles. Nevertheless, they are not to be neglected as their energy range represents important risks for spacecrafts because highly energetic particles can fully pass through their shielding and hit and damage internal components [45]. Indeed, galactic cosmic rays can reach energies up to hundreds of GeV^2 while solar wind particles's energies do not go above a few GeV (cf Figure 2). This motivates the need of accurately modeling and characterizing them.

Because of their high energy, GCRs are particularly hazardous to electronics, but also to biological systems. On Earth, both the atmosphere and magnetosphere shield the planet's surface from GCRs fluxes. Planetary objects also induce a *shadowing effect*. They block part of the cosmic rays flux, which impacts the measurement behind these objects with respect to the incoming direction of the rays. Finally, the solar activity exerts an important modulation on them, as described in the next subsubsection. The solar cycle's periodicity creates a long-term variation, and solar events like *Interplanetary Coronal Mass Ejections* (ICMEs) can deflect low energy GCRs with their strong magnetic field. This effect is known as *Forbush Decrease* [30].

2.1.2 Solar activity and radiations

Our host star has an important influence on the radiation environment in the Solar System. As described in [62], the Sun is far from being in a static state but is instead subject of many active processes. These processes can range from short intense eruptions to long term variations, and properties such as solar winds and surrounding magnetic fields are also to be considered. All these effects play an active role in radiation production and modulation and are grouped under the term *Solar Activity*.

The dominant effect is the solar activity's 11-years periodic cycle, known as *Schwabe Cycle*. During this period, the dipolar solar magnetic field flips, leading to temporary increased strengths for the higher orders of the magnetic field, *i.e.* quadrupole, ocutpole etc. Sunspots, space weather, geomagnetic properties are examples of solar processes, and they all vary in different ways. The *Solar Wind* [46] expands and creates the *Heliosphere* [24], a region dominated by the solar activity. This wind carries the Sun's magnetic field, creating a surrounding zone known as the *Heliospheric Magnetic Field* (HMF). It is to be noted that the HMF exhibits a 22-years periodicity due to a change in polarity at the end of each Schwabe

---

^{2}1GeV = 10^3MeV = 10^9eV
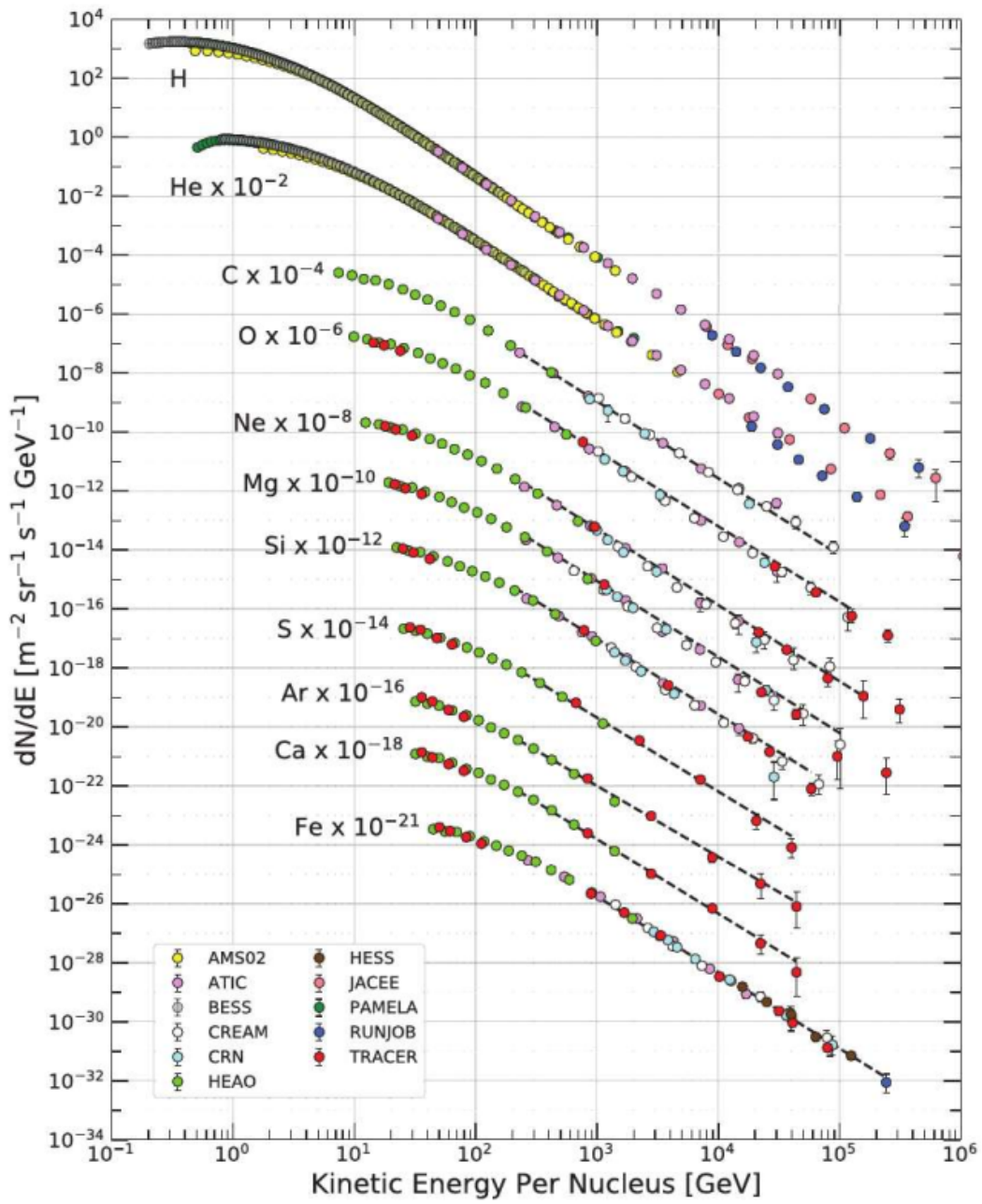
Figure 3: Galactic cosmic radiation measured by several experiments showcasing the abundance of each element. Plotted as particles per energy-per-nucleus against energy-per-nucleus. From [34, 50].

cycle [33]. When crossing through the Solar System, galactic cosmic rays interact with the solar wind and the magnetic field. The heliospheric transport of GCRs is described by Parker's theory [47]. Several processes come into play, including diffusion, convection and drift of cosmic rays particles by the solar winds and the HMF. Most particles are directly reflected back into space, while others diffuse into the solar wind where they remain for long periods of time, losing some of their energy. All of these phenomena induce a variation in the GCRs intensity and energy spectra. In particular, the galactic cosmic rays intensity is heavily modulated by the solar activity with an observed variation of more than 20%. Figure 4 depicts the Sunspots Number (top) as a representative of the solar activity together with the cosmic rays count rate measured by ground-based radiation monitors (bottom) over the period of time 1950-2017. There is a clearly visible anti-correlation between the two, as the aforementioned processes lead to a global decrease of the GCRs particle flux. A more intense solar activity implies more interactions with these particles and therefore decreases the cosmic rays intensity. This effect is referred to as *Solar Modulation* and will be focused on in section 5. An important characteristic of the solar modulation is that it is not instantaneous. The GCRs intensity variation is known to lag behind the solar cycle. The actual value of this time-lag is however not accurately defined and varies from a few months to 1 year depending on the source, with some even mentioning negative values [3, 37, 38].

The solar wind is made of continuously released charged particles travelling to up to 0.25% of the speed of light (about 800km/s). However, the Sun also produces charged particles known as *Solar Energetic Particles* (SEPs) associated with extreme events, namely *Solar Flares* and ICMEs. During these events, the Sun releases big quantities of such particles with high energies (electrons, protons and ions), contributing to the radiation environment in the Solar System. Particle detectors tend to exhibit big sudden increases when these events occur (cf Figure 5), as a lot of particles are emitted at the same time. The intensity of such events is more important in the inner Solar System and gets negligible when going to the outer Solar System as the energy density of the solar radiation follows an inverse square law with respect to heliocentric distance [5]. However, even interplanetary missions to the outer Solar System have a cruise phase within the inner region and are therefore subject to these events.

2.1.3   Trapped particles

Like Earth, Jupiter has a *Magnetosphere*, a region around the planet generated by the planet's internal magnetic field. This region is defined by the magnetic field lines, which cannot cross each other due to Alfvén's theorem [1]. The magnetic field line topology is subject to solar wind forcing, *i.e.* the combined effect of dynamic pressure of the oncoming solar wind particles and the magnetic pressure of the *Interplanetary Magnetic Field*. This leads to a magnetosphere that is compressed on the dayside and elongated on the nightside, reminiscent of the deflection of a running river by a large boulder.

Earth's magnetosphere, as depicted in Figure 6, is a result of a process known as *Dungey cycle*: as the solar wind approaches the planet, it crosses the *Bow Shock* region and deflects around the *Magnetopause*. Within the inner magnetosphere, the planetary magnetic field lines exhibit a majorly dipolar structure. Charged particles coming from Earth's exosphere and solar winds can then enter the magnetosphere via a process called *reconnection*. The plasmasphere of Earth then envelopes the *Van Allen belts*. Particles entering the Van Allen belts regions might get trapped along the local magnetic field lines and follow them in a
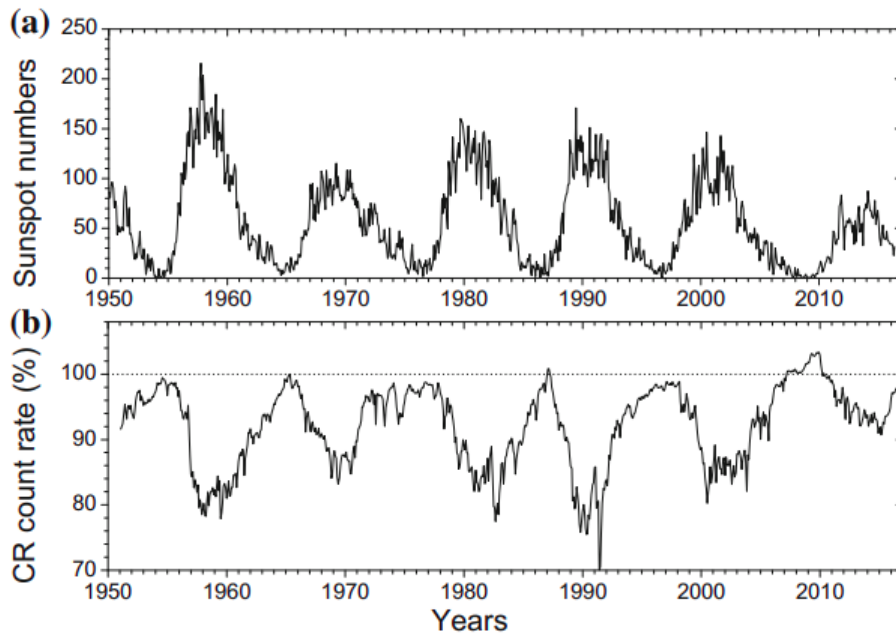
Figure 4: Cyclic variations of the solar activity and the galactic cosmic rays flux between 1951 and 2017. Top: Sunspots numbers scaled with 0.6 factor for readability. Bottom: GCRs flux measured as the count rate of a neutron monitor. 100% count rate corresponds to May 1965. From [62].

swirling motion, staying inside this zone for varying time periods and gaining energy with each bounce. If their energy gets high enough, they behave akin to radiation. Some highly energetic particles can reach low altitudes and interact with Earth's upper atmosphere, creating the northern lights. Others can escape the magnetosphere by reaching the outer-most field lines and following them to outer space. The concentration of such highly energetic particles creates an important radiation environment around the Earth. Additional sources have to be considered as well. For instance, Earth itself is producing particles in the form of plasma, and these stay trapped inside the belts, contributing to the radiation environment.

Figure 6 also displays the magnetospheres of Mercury, Jupiter and Saturn. The scaling gives an estimate on the wide range of sizes of these objects. The magnetosphere of Mercury is heavily compressed on the planet's dayside, as the solar wind's influence is stronger close to the Sun. Intense events like Interplanetary Coronal Mass Ejections can even push the magnetosphere below the surface of the planet. Jupiter's magnetosphere is enormous compared to the others and is, in fact, the largest object in the sky. If it were visible to the naked eye, it would cover approximately the area of a thumb for a human observing the sky.

The particular mission of interest in this study is JUICE, described in the next section. Its objective is the Jupiter system (*Jovian* system). Therefore, it is interesting to describe the radiation environment around this planet. Jupiter is a *gas giant*, *i.e.* a large planet mostly composed of Hydrogen and Helium [44]. These objects all exhibit a planetary magnetic field. The radiation environment at Jupiter is harsher and more complex than at Earth, as the Galilean moons Io and Europa are known to emit plasma particles which get trapped inside the gas giant's huge magnetosphere. The Jovian system is also peculiar as it contains the only moon within our Solar System known to have a magnetosphere: Ganymede, which

7
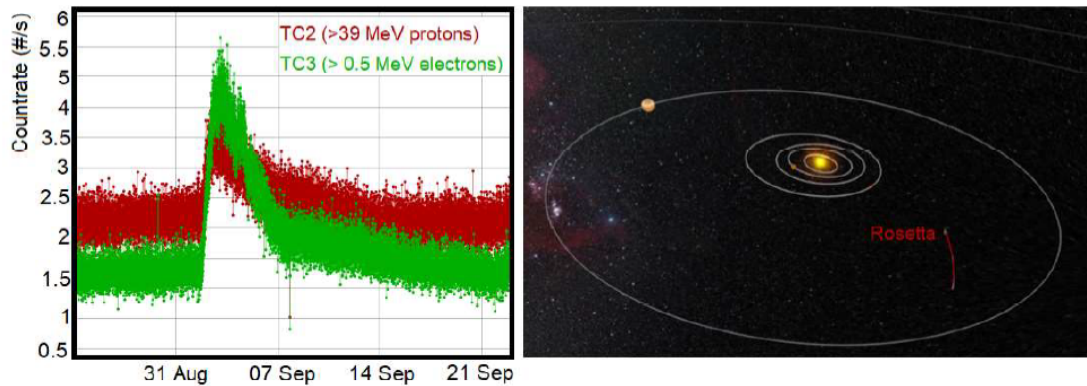
Figure 5: Rosetta's radiation monitor measurements during the September 2nd 2014 solar particle event (left) and its location in the Solar System (right). The monitor exhibits a clear sudden spike in the registered counts during this event. From [50].

also influences the radiation environment. A general representation is displayed in Figure 7. The magnetic field lines coming from Jupiter are depicted and form the shape described previously, with an elongated tail behind the planet with respect to the Sun. The color gradient represents the intensity of the magnetic field along these lines. The positions of the four moons are displayed together with the plasma torus formed around Io's orbit. Finally, JUICE's and *Europa Clipper*'s trajectories are represented for comparison.

The presence of radiation belts is conditioned by the existence of a magnetic field around the planet which can trap particles. Since Mars and Venus do not have a magnetic field, they do not have radiation belts surrounding them either, meaning that the radiation environment around these planets is mainly due to galactic cosmic rays. This will be especially relevant for the analysis conducted in section 5.

2.2 Relevant ESA missions

The data used in this project is related to several ESA missions, three of them being *planetary* ones, *i.e.* orbiting a specific planet. The last one, *Rosetta*, had an orbit around a comet. These missions are briefly described in this subsection, with emphasis on JUICE as it is the main subject of this work.

2.2.1 JUICE

The Jovian system is extremely diverse, be it chemically, geologically or magnetically with a large range of dynamic interactions [25]. Its four big Galilean moons present interesting features as well, such as icy shells, volcanic activity, possible subsurface oceans, magnetospheres etc. Several missions have studied this system in the past, with for instance Jupiter fly-bys by the *Voyager* probes or dedicated planet orbiting by *Juno* and *Galileo*. *Europa Clipper* is a soon-to-be-launched NASA mission towards one of its largest moons.
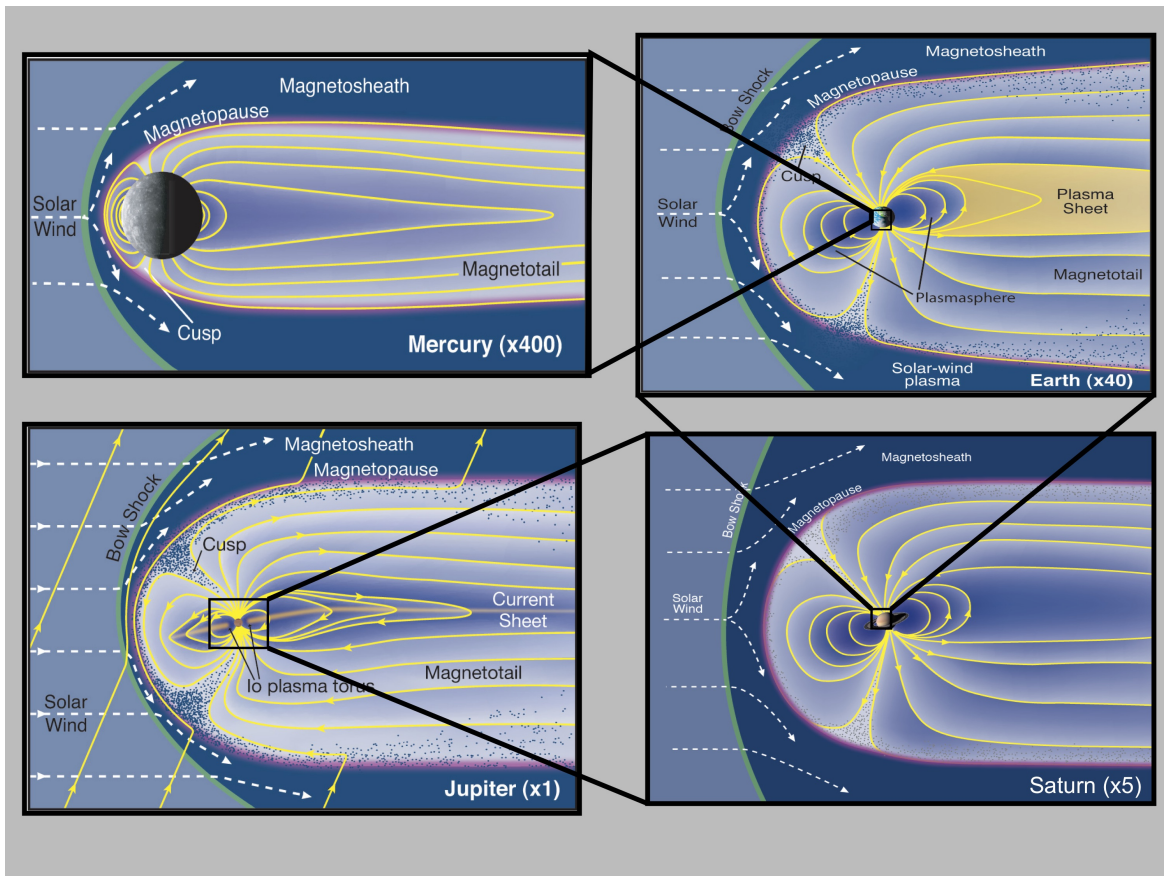
Figure 6: Magnetospheres of Mercury, Earth, Jupiter and Saturn. The black squares linking the pictures are here to represent the scales of these magnetospheres.

JUpiter ICy moons Explorer (JUICE) [16] is the first large mission of ESA's *Cosmic Vision* Programme, aiming at extending our knowledge on the emergence of life in the universe, its origin and fundamental laws. After eight years of transfer from its launch on April 14th 2023 and several gravity assists, JUICE will focus on the Jovian system and Jupiter's three icy moons: Ganymede, Europa and Callisto. These moons are of interest because previous studies have shown that they likely present subsurface oceans under their icy crusts [22], which could represent potential habitable environments outside of the Sun's habitable zone. JUICE will mainly address two science themes: **The emergence of habitable worlds around gas giants** within the possibly habitable environments on the three moons; and **The Jupiter system as an archetype for gas giants** with the Jovian atmosphere, magnetosphere and satellite interactions. It will expand on the knowledge acquired thanks to the previous *Juno* and *Galileo* missions, and answer some of the questions which arose from them.

JUICE is an ESA-led mission with contributions from the United States (NASA), Japan (JAXA) and Israel (ISA) space agencies. Many engineering challenges came with the project, which required precise design decisions to meet the requirements. Firstly, being an outer Solar System mission means that the spacecraft will be much less exposed to the Sun than missions closer to its center, like for instance *BepiColombo*, flying to Mercury. In particular, the sunlight is estimated to be 25 times weaker than on Earth. Huge solar panels had to be designed to fit the energy requirements of the spacecraft and its instruments: 85 m^2 of solar arrays organized in two cross-formations on both sides of the spacecraft carry out this role. Secondly, the Jupiter environment is very harsh, being one of the most intense
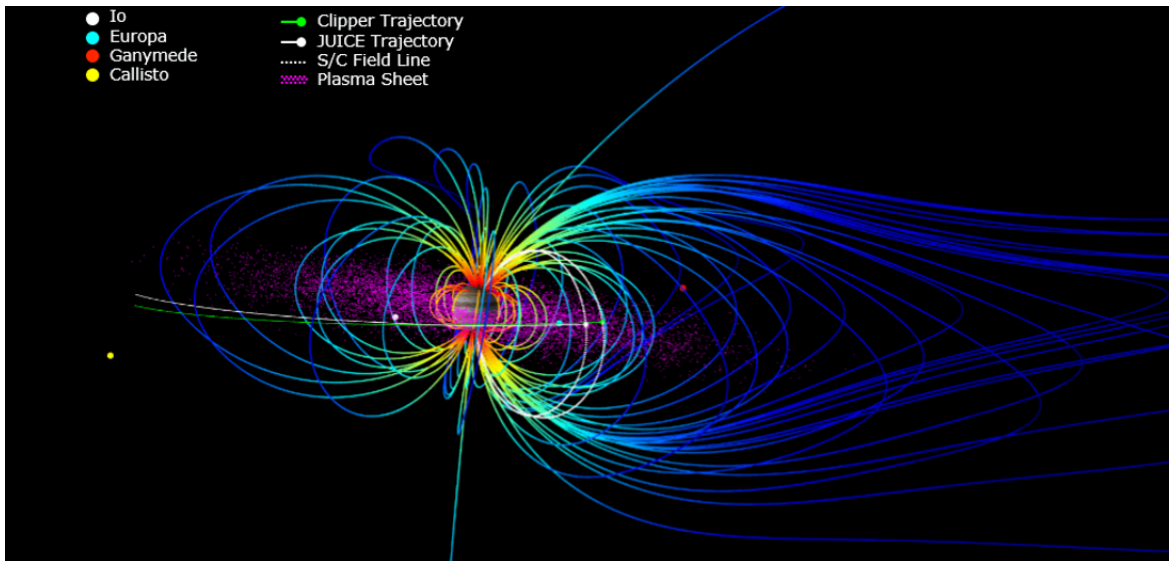
Figure 7: Jupiter's magnetosphere and moon interactions. The magnetic field lines are colored to represent the field intensity and the purple dots correspond to the plasma sheet surrounding the gas giant. JUICE's and Europa Clipper's trajectories are represented as the two curved white and green lines respectively. The four Galilean moons of the Jovian system are depicted as well. From [36].

radiation environment in the Solar System. This required particularly strong shielding of sensitive electronic devices. The temperature gradient during the mission is also important, with temperatures ranging between +250°C during the Venus flyby and −230°C at Jupiter, which motivated the use of a novel *Multi-Layer Insulation* for thermal isolation. Finally, the long distance slows down data transfer, with a communication roundtrip of about 90 min. A 2.5-m antenna is included to send data and onboard computers are dedicated for general data transfer and independent issue solving. JUICE is displayed in Figure 8. The human figure next to it gives an estimate of the huge scale of the spacecraft.
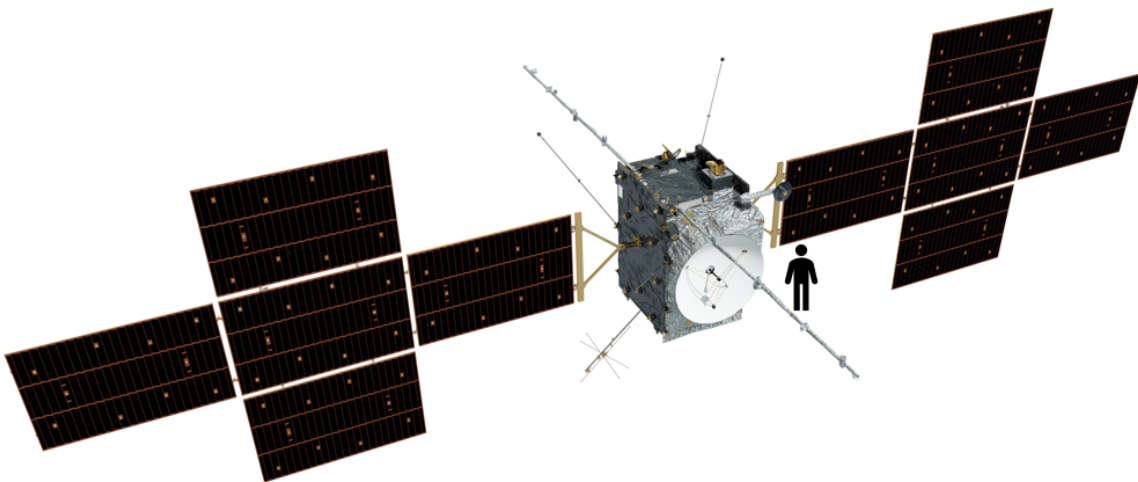
Figure 8: JUICE spacecraft next to a human figure for scale reference.

As one of ESA's most ambitious missions, JUICE's scientific payload is made of ten state-of-the-art instruments divided into three packages. The *Remote Sensing Package* contains imaging devices for analyzing Jupiter and its moons' properties such as atmosphere, geological history, chemistry and their interactions. As its name suggests, it is dedicated to remote sensing, *i.e.* characterization of these properties by looking at the objects from a distance, as the spacecraft is orbiting them and not landing on them. On the contrary, the *In-situ Package* has been designed for *in-situ* analysis of the environment around the planet in which the spacecraft will evolve. It will study the radiation environment, the magnetosphere and the electric field surrounding the planet and its moons, most notably Ganymede. Finally, the *Geophysical Package* is dedicated to exploring the moons' surface and subsurface with a laser altimeter and a radar sounder. The list of JUICE's scientific instruments is presented in Table 1.

Table 1: JUICE's scientific instruments. Adapted from [11].

Package	Instrument	Full name
Remote sensing	JANUS	Optical camera system
	MAJIS	Moons And Jupiter Imaging Spectrometer
	UVS	UV imaging Spectrograph
	SWI	Sub-millimeter Wave Instrument
Geophysical	GALA	GAnymede Laser Altimeter
	RIME	Radar for Icy Moons Exploration
	3GM	Gravity and Geophysics of Jupiter and Galilean Moons
In-situ	PEP	Particle Environment Package
	J-MAG	JUICE-MAGnetometer
	RPWI	Radio and Plasma Wave Investigation

Additional instruments are also present for housekeeping purposes, referred to as *Support Instruments*. The first one is an experiment dedicated to radio waves included in the form of the *Planetary Radio Interferometer and Doppler Experiment* (PRIDE). The other one is the *RADiation-hard Electron Monitor* (RADEM). As this project is about radiation monitoring for galactic cosmic rays, this instrument is the point of focus of this study and will be described in more details in subsubsection 2.3.3. It is displayed in Figure 9. RADEM is placed on the back of the spacecraft, with its four detector heads facing outwards. This work was dedicated to the characterization of the *Heavy-Ion Detector Head* (HIDH), which is the second one starting from the back of the picture, pointed at by a red arrow. It will be further detailed in the following sections.

In February 2023, the JUICE spacecraft arrived in Kourou, french Guyana and underwent a series of tests prior launch. It was then mounted on the Ariane 5 launcher and encapsulated in the fairing, ready for takeoff. The launch date was set to April 13th 2023 at exactly 14:15:01. However, the procedure was aborted a few minutes before due to weather constraints. The next day, on April 14th 2023, the restarted launch sequence went as planned and JUICE took off onboard the rocket. After the orbit insertion by Ariane 5, the spacecraft sent its first signal (Figure 10), marking the beginning of ESA's control on it. The solar arrays and all the mechanical systems then deployed as planned.
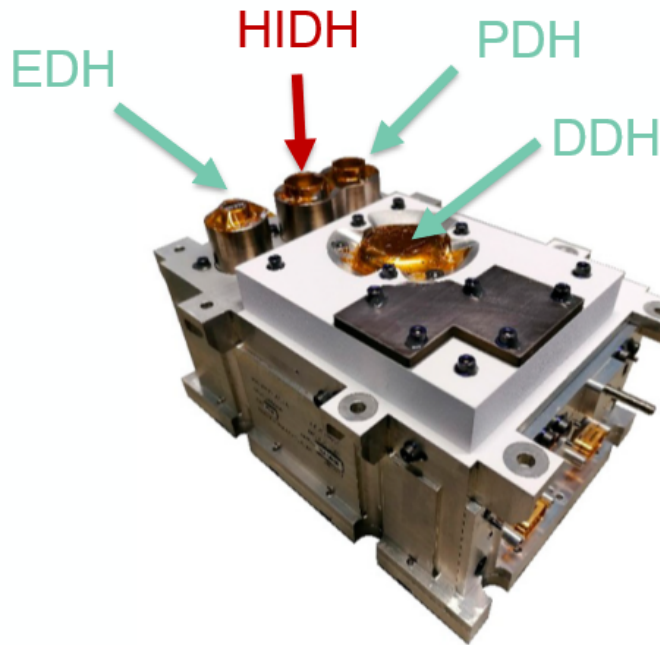
Figure 9: JUICE's radiation monitor: RADEM. The three metallic cylinders in the back of the picture and the rounded metallic center piece are the detector heads used for particle analysis. These will be described in subsubsection 2.3.3 Credit: EFAFEC.

After these first procedures, the *Commissioning Phase* started, *i.e.* the period of time at the beginning of a mission during which all instruments are tested to make sure they function nominally in space. It ended in the middle of July 2023. During this phase, RADEM's response to telecommunication commands and radiation monitoring performance were tested. Overall, the instrument worked as expected, but a few issues were found. In particular, the monitor did not respond to some commands. More importantly in the context of this work, no signal was received from the first of the two diodes of the HIDH. This malfunctioning of the detector would greatly impact the quality of the cosmic rays detection by RADEM. These issues are still under investigation. The original plan was to use this data for comparison with the simulation results presented in this thesis. However, the available data from this period is very limited and there are uncertainties related to the configuration of the HIDH during this time. It was thus not used in this work.

2.2.2 *Mars Express*

First ESA mission to the Red planet, *Mars Express* [13] takes its name from the record time and cost needed to build it with respect to similar missions. After its launch in June 2003, it went into orbit around Mars in December of the same year and started its operations. Since then, it provided many 3D views of the planet, facilitating the mapping of its surface and study of its geological and topographical properties. It most notably made significant contributions to the proof of past liquid water on Mars and its recently active volcanism [10]. Additional contributions of this mission include the discovery of Mars' aurorae and an in-depth characterization of its moon Phobos [4].
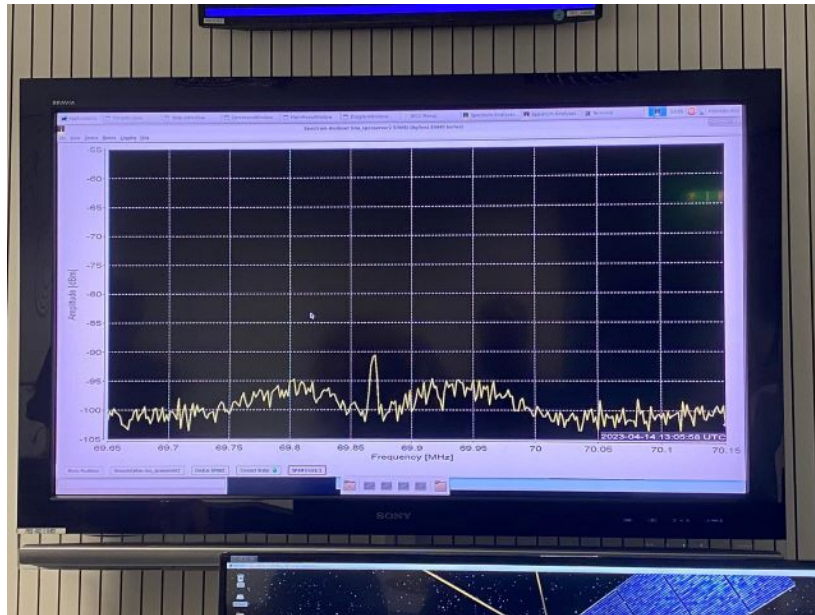
Figure 10: First signal sent by JUICE. This signal marks the beginning of ESA's control on the spacecraft and created some tension in the control rooms, as it took longer than expected to arrive. From [12].

Mars Express has been a key actor in reinforcing NASA-ESA relations, as it provided communication with the United States' agency rovers on the surface and mapped the *Curiosity* rover's landing site. Finally, *Mars Express* is still active and preparing the way for ESA's next ambitious Mars mission: the orbiter-rover collaboration *ExoMars*.

This mission is of interest here thanks to a previous study described in [37] involving the error detection and correction procedure implemented on it. While this procedure leverages housekeeping data, it holds some scientific value in the characterization of galactic cosmic rays, hence its presence in this work. Dedicated sections can be found further in this thesis.

2.2.3 *Venus Express*

Built around the design of the previous mission, *Venus Express* [15] was ESA's first mission to our nearest planetary neighbour. After its launch in November 2005, it operated in orbit around the planet between April 2006 and its fuel exhaustion in December 2014. Its main objectives were the study of Venus' atmosphere, plasma environment and surface. In particular, it realized a series of aerobraking maneuvers to enter the atmosphere at 130 km above ground and characterize its density. As can be seen in Figure 11, *Venus Express* is heavily based on its predecessor *Mars Express*.

As for *Mars Express*, the interest of this mission here is its error detection and correction procedure, which will be detailed in section 5.

13
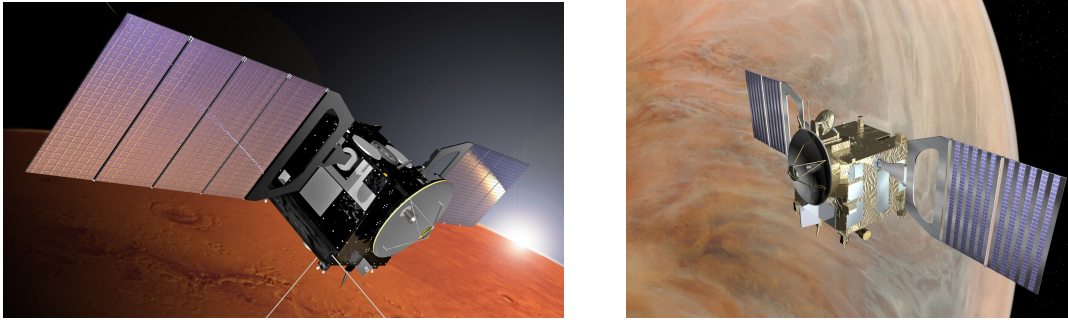
Figure 11: Mars Express (left) and Venus Express (right) spacecrafts. Their similar designs stem from the efficient and fast building procedure developed for Mars Express and reused for Venus Express.

2.2.4 *Rosetta*

Contrary to the above-described missions, *Rosetta* [14] is not a planetary mission. This mission targeted the comet 67P/Churyumov–Gerasimenko to investigate its local plasma environment, map its peculiar "duck"-shaped body and deliver the surface probe *Philae*. It launched in March 2004, arrived at the comet in August 2014 and delivered its lander in November 2014. It was the first ever mission to follow and rendezvous with a comet, and to deploy a probe on its surface (Figure 12).

Rosetta was studied in this project for the same reason as the two previous *Express* missions: its error detection and correction procedure. It was particularly interesting because its trajectory away from the Sun gave access to a much larger distance range to assess this variation.
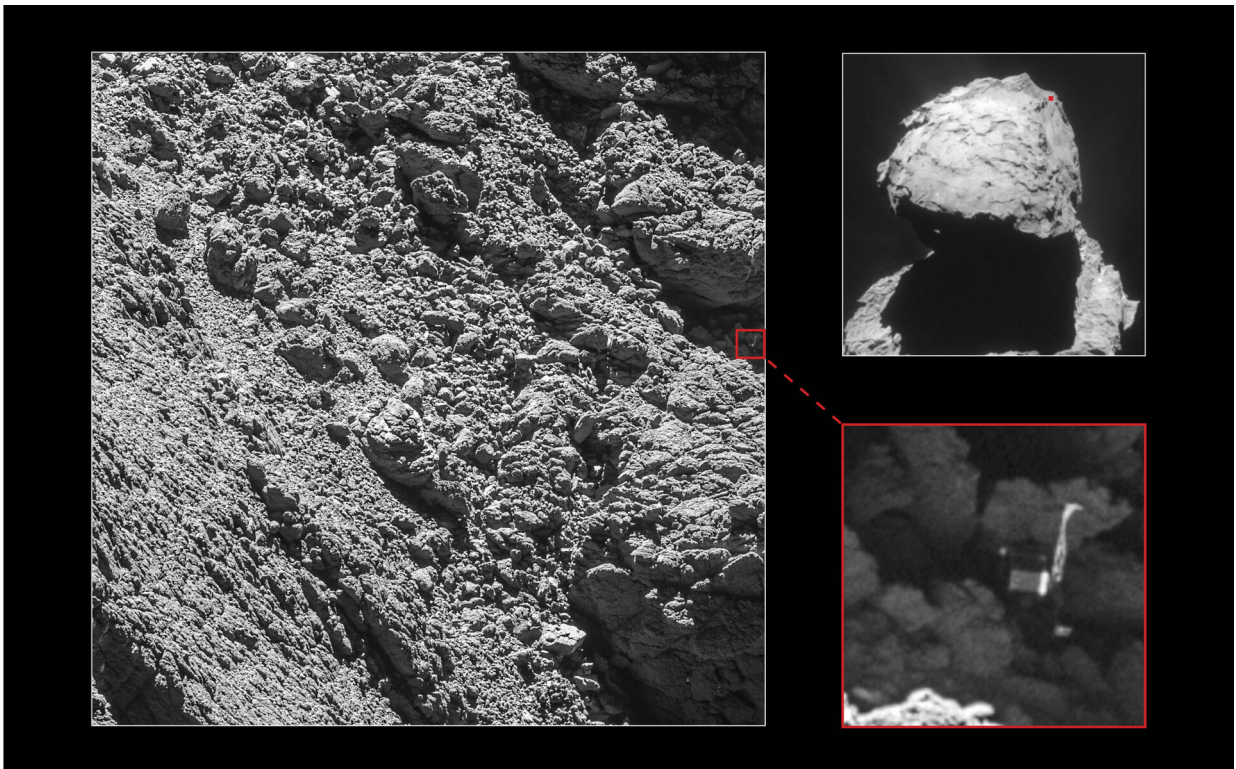
Figure 12: Picture of Philae on the comet, taken from the Rosetta spacecraft.

2.3 Analysis and characterization of space particles interactions with a spacecraft

As described in subsection 2.1, the space environment is full of radiation of various origins which can be hazardous to spacecrafts, requiring an appropriate shielding in order to survive the duration of the mission and stay operational. Radiations are monitored with dedicated housekeeping instruments such as RADEM. As this project is about characterizing galactic cosmic rays through these instruments, it is necessary to introduce the fundamentals of particle-detector interactions and to give an overview of JUICE's radiation monitor. Finally, as previously mentioned, particles can also have an impact on some spacecraft components, especially when these are not shielded because of mass budget constraints. This can introduce errors, which have to be taken into account in order to accurately interpret the data.

2.3.1 Electromagnetic interactions

Photons and charged particles interact with electronics components via a set of electromagnetic interactions during which they lose energy. These interactions contribute to the *Total Ionizing Dose* (TID) in electronics components which is a source of degradation. As they depend on the type of particles, their energy range, and the medium, these same processes are also leveraged for detection purposes. This subsubsection gives a brief overview of some of the electromagnetic interactions relevant in this context. It is based on subsection 3.1 in [50].

Photons

The contribution of photons to the space radiation environment is minimal. However, they can be produced by charged particles interactions in materials (high energy electrons). They interact with matter by three main processes depending on their initial energy:

- Photoelectric Effect: the emission of electrons when electromagnetic radiation hits a material. (Low energy phenomenon)

- Compton Scattering: the scattering of a photon after its interaction with a charged particle, resulting in an energy decrease. (Medium energy phenomenon)

- Pair production: creation of an electron-positron pair from a photon passing through an external Coulomb field. (High energy phenomenon)

These particles will not be considered in the rest of this thesis. However, their influence might be implicitly taken into account in the subsequent particle physics simulations.

Electrons

As previously discussed, electrons are an important part of the space radiation environment. They lose energy via two main processes. Firstly, they can collide with other particles in the material and can either ionize, excite or displace the atoms in the structure. The average energy loss per unit of length is represented by the *Stopping Power* of the medium and is different for each particle and each material. In particular, the stopping power is proportional to the density of the material. Because of their low mass, electrons lose more energy per collision than heavier charged particles. Secondly, electrons can emit radiation after being accelerated in the electrostatic field of atoms. This process is known as *Bremsstrahlung*.

Heavy charged particles

Protons and heavier charged particles also lose energy via scattering and radiation. The rate of energy loss is described by the *Beth-Bloch* formula. An example of stopping power curve computed from the *National Institute of Standards and Technology* (NIST) [34] is displayed in Figure 13 for proton particles in Silicon. As seen from the figure, the stopping power is higher for particles with lower energies than for particles with higher energies. The actual process is more complex and outside the scope of this thesis. Intuitively, high energy particles exhibit high velocities, thus travelling faster through the medium and interacting less with it. They hence tend to deposit less energy, corresponding to a lower stopping power.
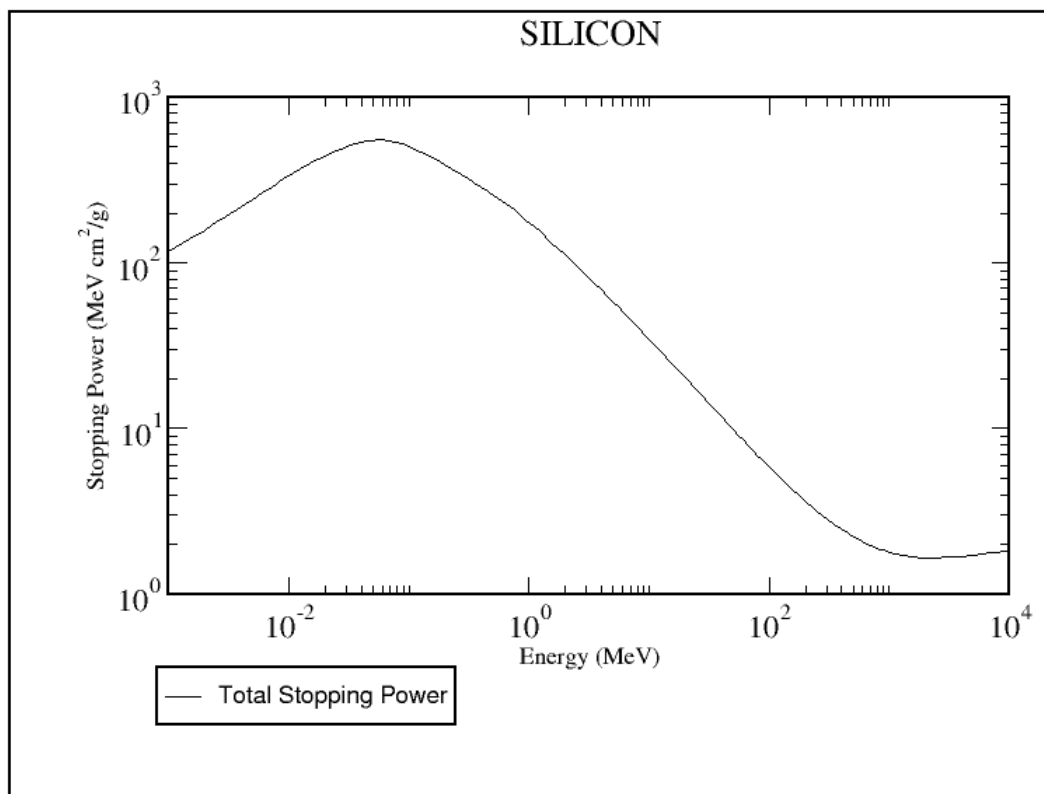
Figure 13: Stopping power for proton particles inside a Silicon medium. From [34].

When an energetic charged particle passes through a semiconductor material like the Silicon diodes used in RADEM, it loses energy and frees *electron-holes pairs* in the process [19]. The *particle's range* is defined as the total path length travelled in the semiconductor before the particle loses all of its energy and comes to rest. Associated to this phenomenon is a charge deposition of the particle on the electronics material known as *direct ionization*. This ionization is the main cause of upsets in memory circuits [56] for heavy charged elements. As the main goal of this thesis is to characterize the *Heavy-Ion Detector Head*, the focus will be set on these heavy elements coming from galactic cosmic rays.

2.3.2 Elements of particles-space detector interactions

RADEM contains detector heads referred to as *Stack Detectors* which follow the concepts of the *Standard Radiation Environment Monitor* (SREM) [42] and the *Multi-Function Spectrometer* (MFS) [21]. Namely, each head is an arrangement of layers through which the particles pass one after the other. As the particle goes through the layers, it loses energy by coloumbic deposition and, to a lesser extent, nuclear interactions. The layers can serve two primary roles: purely slowing down the particle (absorbers) or measuring the deposited energy (Silicon diodes). Because of the stacked configuration, the more energetic the particle is, the deeper it goes in the detector. The initial energy can then be inferred from the deepest diode it interacted with.

The deposited energy depends on the material of the layer and the nature of the particle through the stopping power P of the medium, its density ρ, and the length l travelled by the particle. Mathematically, the deposited energy E_d of a particle with primary energy E_0 can be found via:

$$E_d = \max(E_0, P \cdot \rho \cdot l). \tag{1}$$

The final energy of the particle after passing through the diode is then obtained via a simple substraction:

$$E_f = E_0 - E_d. \tag{2}$$

If $E_f = 0$, *i.e.* the particle deposited all of its energy into the layer, it embedds itself into the medium. Otherwise, it continues its way through the detector, and possibly exits it. Finally, the energy can be converted to induced charge via electron-hole pairs creation. The conversion rate is given by the *Transfer Energy T_E* of the material (*e.g.* 3.6 eV/pair for Silicon). Multiplying the result by the electrons elementary charge ($e = 1.60217663 \times 10^{-19}$C) gives the final induced charge I_c by the particle on the medium.

$$I_c = e \cdot \frac{E_d}{T_E} \tag{3}$$

This is useful because thresholds on RADEM are defined in terms of induced charge [51].

In the case of RADEM, diodes are made of Silicon (Si) and absorbers made of Aluminium (Al) or Tantalum (Ta). The actual heads configurations are detailed in the next section, but the general concept is as follows. The first layers are made of alternating layers of Aluminium absorbers to slow down particles and Silicon diodes to measure the induced charge. Then, the bottom layers use Tantalum absorbers instead, which tend to slow down particles more than the Aluminium ones.

2.3.3 Radiation monitoring on *JUICE*

RADEM is a radiation monitor developed for analyzing energetic particles present in the harsh radiation environment around Jupiter, with particle energies much higher than those found in the Van Allen belts. Its main goal will be to study the dynamics of the Jovian radiation belts, understand trapped particles in plasma with their energy gains and losses, monitor the space weather across the Solar System, and compare the Jupiter and Earth radiation environments.

Electronics

The front-end electronics structure of RADEM relies on an *Application-Specific Integrated Circuit* (ASIC) called the ASIC VATA466 [58]. The ASIC has 4 Low-Gain channels and 32 High-Gain channels. The Low-Gain channels have one charge discriminator each which act as lower charge thresholds, and the High-Gain channels have two charge discriminator acting as lower and upper charge thresholds. The channels are connected to 22-bit counters which register their outputs as pulse heights. In the case of the HIDH, each of the two diodes is connected to one of the Low-Gain channels, so that only lower thresholds can be set.

The ASIC also implements a *coincidence scheme* which allows to make a connection between the outputs of different channels. If a hit is registered in several different channels within a small time period, it is assumed that the same particle was responsible for all of them. The possible hold time of the coincidence units can take values in $[50, 600]$ ns. The HIDH is made of two diodes, so that two *coincidence modes* are available:

1. No coincidence: the diodes are completely independent, any measurement on one diode does not influence the other.

2. 1-1 coincidence: a particle hit on the second diode D2 is only registered if the particle interacted with the first diode D1 as well. This allows to only consider the particles going through both diodes.

In this work, only the first mode is considered, without coincidence. This is especially relevant as the current issues on the HIDH's first diode do not allow to use the 1-1 coincidence mode. However, the procedure and considerations made in the following sections are also applicable to a 1-1 coincidence mode. The results are expected to be similar as well.

Detectors

RADEM will focus on energetic particles using its four detector heads which allow for discrimination between different types of particles and for characterization of their directional dependence. These detector heads are the following:

- The *Electron Detector Head* (*EDH*): designed for electrons in the energy range $[0.3, 40]$ MeV[3];

- The *Proton Detector Head* (*PDH*): designed for protons in the energy range $[5, 250]$ MeV;

---

[3] $1\text{MeV} = 10^6\text{eV}$

- The *Heavy-Ion Detector Head* (*HIDH*): designed for ions in the energy range [8, 670] MeV. It allows discrimination of heavy ions (atomic number $z \geq 2$) up to Oxygen ($z = 8$);

- The *Directionality Detector Head* (*DDH*): designed for measuring electron directions and characterize the angular dependence of electron fluxes [51] .

The DDH has been designed following the findings of *Juno*'s *Energetic Particle Detector* (EPD), which observed a strong angular variability in electron fluxes in the Jovian system. More details are available in [50] and [51]. In this work, the focus is set on the other three detector heads, which are based on a standard Silicon stack detector similar as the ones used in SREMs [42]. They are composed of an arrangement of $300\mu m$-thick Silicon (Si) diodes, with Aluminium (Al) and Tantalum (Ta) absorbers. The schematics taken from [50] are displayed in Figure 14. The general configuration of the three RADEM detector heads is as follows:

- EDH: eight Silicon diodes with fours Aluminium absorbers of increasing size in the upper layers, and three larger Tantalum absorbers on the bottom. It is surrounded by an 8 mm Copper collimator with an approximate 15° field of view;

- PDH: similar to the EDH. The dimensions are different to account for the difference in particles.

- HIDH: only two diodes and one Aluminium absorber. Differentiation with the other particles is done thanks to their difference in energy using the embedded software.

Since heavy elements interact more with matter than lighter elements, hence depositing more energy, the HIDH is composed of less layers than the PDH and EDH.
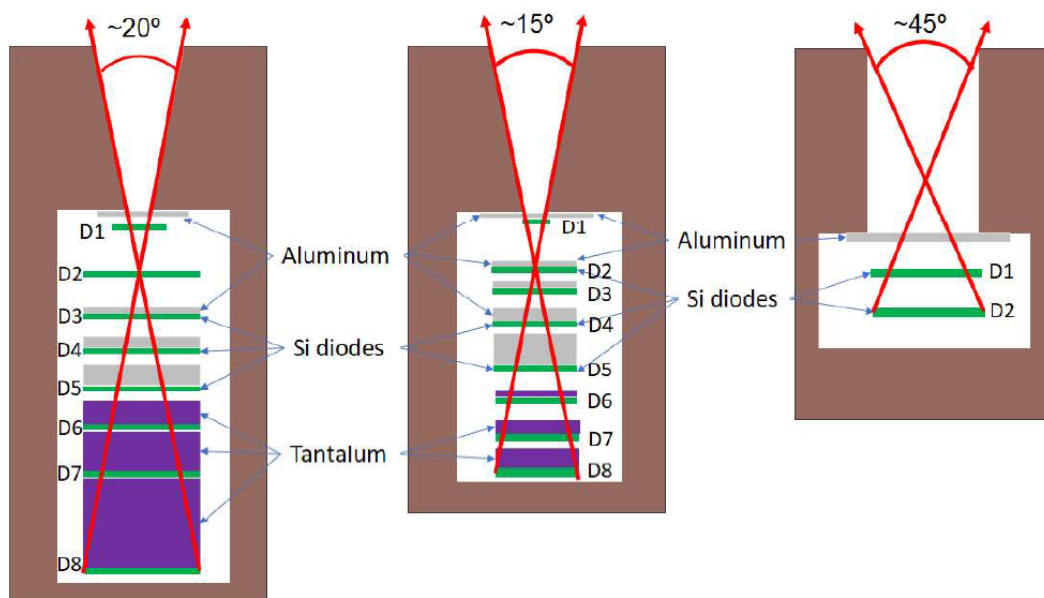
Figure 14: Schematics of the PDH (left), EDH (center) and HIDH (right). From [50].

As previously mentioned, the diodes are connected to channels set with lower thresholds, *i.e.* charge values C_0 such that only particles inducing at least $C \geq C_0$ fC on the diode are considered. These thresholds can take values in a range $[C_{\min}, C_{\max}]$ which depends on the detector head. However, accessing this range in a continuous manner is not possible. Indeed, the corresponding information is stored in a fixed number of bits N referred to as *Digital Analog Converter* (DAC). This implies that the charge thresholds C can only be incremented by a value

$$\Delta C = \frac{C_{\max} - C_{\min}}{2^N - 1}. \tag{4}$$

To specify a given charge threshold on a diode, an integer value t (with the units of DAC) is set in the range $[0, 2^N - 1]$. Then, the corresponding charge value C (in fC) is deduced using Equation (4) via

$$C = C_{\min} + t \cdot \Delta C. \tag{5}$$

Since this work focuses on the HIDH, values for this head are considered in the following. The thresholds in units of DAC are referred to as t_1 and t_2, respectively for diodes 1 and 2. From the technical report, the configuration of the HIDH is as reported in Table 2. The current threshold values reported correspond to the current configuration on the detector onboard the JUICE spacecraft.

Table 2: HIDH configuration.

Parameter	Symbol	Value	Unit
Number of bits DAC	N	10	-
Minimum charge threshold	$C_{\min}$	0	fC
Maximum charge threshold	$C_{\max}$	22800	fC
Current threshold diode 1	t_1	52	DAC
Current threshold diode 2	t_2	244	DAC
Radius aperture	R_0	0.6	cm
Radius diode 1	R_1	0.6	cm
Radius diode 2	R_2	0.6	cm
Depth diode 1	l_1	2.42	cm
Depth diode 2	l_2	2.84	cm

2.3.4 Detector properties

Several properties are of interest to characterize the detector. This work focuses on three of them: the *Field of View*, the *Geometric Factors* and the *Count Rates*. This part reports the definitions of these quantities and describes how to infer them from simulations.

Field of view

The *Field of View* (FOV) of a detector is defined as the solid angle through which it is sensitive to incoming particles. From Figure 14, the HIDH's FOV is $\eta = 45°$. As can be seen on Figure 15, the maximum angle an incoming particle can make with the vertical to interact with both diodes is half of the field of view: $\theta = \frac{1}{2}\eta = 22.5°$. Therefore, the FOV of

the HIDH can be validated from the simulations by computing the value of θ for all particles interacting with both diodes. This is done in subsubsection 4.3.3. Note that the angle values are expected to be slightly higher for the first diode, as the FOV is defined from the second diode (cf Figure 14). Indeed, because more particles interact with the first diode than with the second diode, the first one covers a wider range and thus a wider angle.
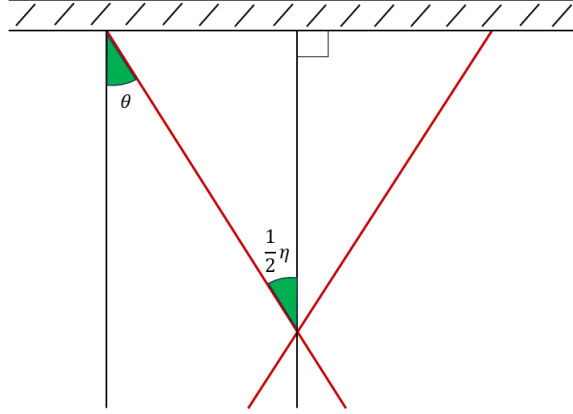
Figure 15: Abstract FOV η of a detector and maximum angle of a particle θ. θ and $\frac{1}{2}\eta$ are alternate interior angles, making them equal.

Geometric factor

The response functions of the detector's channels (or equivalently of the diodes) are defined in terms of the channels' *Geometric Factors* as a function of the primary energy of the incident particles. According to [59], the geometric factor G of a channel relates its counting rate R to the intensity of the radiation I when isotropy is assumed via a simple proportionality rule:

$$R \;=\; GI. \tag{6}$$

The geometric factor is a function of the particle's primary energy and represents the probability that a particle with given energy E can interact with the diode. Under assumptions described in [59], it can be computed as an integral over the solid angle of the field of view ω as:

$$G \;=\; \int_{\Omega} \int_{S} \mathrm{d}\omega \mathrm{d}\sigma \cdot r, \tag{7}$$

where $\mathrm{d}\sigma \cdot r$ is the effective surface element of the diode looking into ω.

Because its diodes are not directly exposed to the space environment but are rather placed inside the detector, the HIDH configuration corresponds to a two elements telescope with the first element being the detector's top aperture and the second element being the diode of interest. In that case, the domain Ω is limited by the top element and the surface S is the surface of the diode. [59] gives an explicit formula by direct integration of Equation (7). From there, the ideal geometric factor G_i of each diode $i \in \{1, 2\}$ can be computed from their radii R_i and and depths l_i as:

$$G_i \;=\; \frac{1}{2}\pi^2[R_0^2 + R_i^2 + l_i^2 - \sqrt{(R_0^2 + R_i^2 + l_i^2)^2 - 4R_0^2 R_i^2}], \; i = 1, 2. \tag{8}$$

The values of the relevant radii and depths are reported in Table 2.

Equation (8) describes how to compute the theoretical ideal value of the geometric factor for a given diode. However, the effective geometric factor is different in reality, as it depends on the particles' primary energy, their distribution and their interactions with the diodes. It can be computed from the simulations according to Equation (4.1) in [6]. For a source area A and isotropic angular distribution of source particles, the effective geometric factor $\tilde{G}_i(E)$ of a channel for particles with primary energy E is found via:

$$\tilde{G}_i(E) \quad = \quad A\pi \frac{N_i(E)}{N(E)}, \tag{9}$$

where $N_i(E)$ is the number of particles with primary energy E interacting with channel i and $N(E)$ is the total number of source particles with this energy. Because the angle π represents the solid angle of the source particles, it is expressed in units of *stereoradiants* (sr). Since the area A is in cm^2, the geometric factor has units of cm$^2\cdot$sr.

Count rates

Another interesting property of the detector is the channels' *Count Rates*, *i.e.* the number of counts a channel registers each second, in s^{-1}. It was already mentioned in Equation (7) as R and can be computed according to Equation (5.1) in [6]. The count rate R_i of a channel i is inferred from the local particle flux $\varphi(E)$ and the effective geometric factor $\tilde{G}_i(E)$ via:

$$R_i \quad = \quad \int_0^\infty \varphi(E) G_i(E) \mathrm{d}E. \tag{10}$$

In practice, the effective count rate $\tilde{R}_i$ is computed from the effective threshold from Equation (9) and the energy E only takes values in a given interval $[E_{\min}, E_{\max}]$ so that:

$$\tilde{R}_i \quad = \quad \int_{E_{\min}}^{E_{\max}} \varphi(E) \tilde{G}_i(E) \mathrm{d}E. \tag{11}$$

Note that $\varphi(E)$ has units of MeV^{-1}sr^{-1}cm^{-2}s^{-1}. Multiplying it with $\tilde{G}_i(E)$ and integrating over the primary energy E indeed yields a result in units of s^{-1}. The resulting count rate is a single real number representing the number of counts per second on the channel.

2.3.5   Error detection and correction

A spacecraft holds multiple scientific instruments, and consequently memory devices to store information. These components usually cannot be shielded due to the physical properties of the particles and the strict mass budgets on the spacecraft. As previously mentioned, direct ionization of the electronics components happens when high energy particles interact with them. If one of these particles hits the memory circuit, it can create sufficient charge in a transistor to change its state and effectively corrupt the information stored in memory. This type of error is typically non-destructive, also called *soft error*, and is known as a *Single Event Upset* (SEU) [56].

Soft errors can be corrected by reprogramming the circuit or restarting a program. This is done through an *Error Detection And Correction* (EDAC) algorithm onboard the spacecraft [27]. A corresponding EDAC counter is increased by 1 unit each time a correction is done. This increasing counter represents the number of detected and corrected errors due to SEUs. There is a relatively steady cumulative EDAC increase attributed to the continuous presence of cosmic rays as only high energy particles are expected to trigger SEUs. However, the counter can exhibit sporadic sudden increases due to SEP events, during which a lot of these particles hit the spacecraft and induce SEUs. Protons in the Earth radiation belts can have a similar effect as well.

The EDAC counter data is ordinarily used for housekeeping but not as scientific value. However, as only highly energetic particles mostly coming from the GCRs induce an increase in the counter, the relationship between EDAC variation and GCRs intensity is worth exploring. In fact, [37] established it, making use of the connection between the SEUs and the presence of GCRs in the vicinity of the spacecraft. The procedure was developed on data coming from *Mars Express* and *Rosetta*, based on the fact that these spacecrafts did not enter radiation belts during their mission time. In December 2022, the EDAC data from *Venus Express* was recovered. As Venus does not have radiation belts either, the increasing EDAC counter on *Venus Express* is expected to only capture the influence of galactic cosmic rays particles on memory devices. This motivated the testing and further investigation of GCRs characterization with EDAC counters. The results of this investigation are reported in section 5.

3 Numerical tools and modeling approach

This section describes the numerical tools used for simulation and data analysis in this project. It first reports the framework used for generating GCRs fluxes and understanding which particles to simulate: `PyCREME`, based on the ISO15390 GCRs model. Then, the two simulation frameworks are presented: `FOCom-PDI`, a custom-developed first order computation scheme for particle-detector interaction; and `Geant4`, the CERN-developed reference simulation software for the passage of particles through matter. Finally, it presents `ROOT`, the data analysis tool used to process the simulation results.

3.1 `PyCREME` for GCRs flux generation

The first step towards simulating the interaction of GCRs fluxes with the RADEM detector is to know which particles should be considered and their energy. Thus, it is necessary to understand the composition of GCRs. This is what `PyCREME` [52] is used for. Based on the ISO15390 model [60], it allows to generate GCRs particle fluxes and evaluate which elements are the most abundant together with their energy ranges. To do so, it leverages the known anti-correlation between the GCRs intensity and the solar cycle [43]. Based on this relationship, it uses the Sunspots Number information from an input date to generate the corresponding GCRs flux.

3.2 First order computation with `FOCom-PDI`

To get an initial idea before moving on to the main simulation software, a first order computation framework was developed in `Python3` to simulate particle-detector interactions. It is composed of several modules modelling the various systems in play. This section describes the general architecture implemented for this simulation procedure. The package is referred to as `FOCom-PDI`, standing for *First Order Computation for Particle-Detector Interactions*.

3.2.1 The `Particle` class

A particle's characteristics are encapsulated in a dedicated class containing the necessary attributes (atomic number, initial and current energy) to follow the particle during the simulation. A `Particle`'s name is set via its atomic number and a reference to the symbols list in a separate file.

```python
class Particle :
    def __init__(self, z, initial_energy):
        self.z = z
        self.energy = initial_energy
        self.initial_energy = initial_energy
        self.name = csts.Element_Symbol[z]

    def update_energy(self, new_energy):
        self.energy = new_energy
```

Listing 1: `Particle` class.

3.2.2 The `Detector` class and its modules

Particles interact with the detector by passing through different layers defined by their material and thickness. A `Layer` contains attributes describing its material (atomic number Z), `thickness` and `density`. It also holds an attribute for the energy deposited by the particle when passing through it. This class implements the interaction between a particle and a detector layer given a step size representing the path length travelled by the particle in the layer. In particular, the method `compute_stopping_power()` reads the stopping power curve for a given particle considering the layer's material. It then performs an interpolation to estimate the stopping power corresponding to the particle's exact energy given the discrete data. The deposited energy of the particle is computed in the `absorb_energy()` method. Note that a particle cannot deposit more energy than it currently holds at each step. Therefore, if a particle deposits all of its energy, it embeds itself into the material and the simulation stops.

```python
class Layer:
    def __init__(self, Z, density, thickness) -> None:
        self.Z = Z
        self.thickness = thickness
        self.density = density
        self.name = csts.Element_Symbol[Z]

        self.deposited_energy = 0

    def compute_stopping_power(self, particle):
        # Read the stopping power
        Energy, StoppingPower, _ = RSP.ReadElementSP(particle.z, self.Z)

        # Convert energy in MeV
        Energy = Energy * csts.AtomicMass[particle.z-1]

        # Gather results in a df
        stopping_power_curve = pd.DataFrame({"Energy":Energy, "Stopping power":StoppingPower})

        # Interpolate stopping power curve
        stopping_power = np.interp(particle.energy,
        stopping_power_curve["Energy"], stopping_power_curve["Stopping power"])

        return stopping_power * self.density

    def absorb_energy(self, particle : prt.Particle, distance):
        stopping_power = self.compute_stopping_power(particle)

        # Compute deposited energy
        deposited_energy = stopping_power * distance
        final_energy = particle.energy - deposited_energy

        # Check if deposited more energy than initial
        if deposited_energy >= particle.energy:
            deposited_energy = particle.energy
            final_energy = 0

        # Update particle's energy and layer's total deposited energy
        particle.update_energy(final_energy)
        self.deposited_energy = self.deposited_energy + deposited_energy
```

```
41    def simulate_particle_through_whole_layer(self, particle : prt.
      Particle, step_size, display_results=True):
42        self.reset()
43        nb_steps = round(self.thickness/step_size)
44        for _ in range(nb_steps):
45            # Compute energy transfer
46            self.absorb_energy(particle, step_size)
47            if particle.energy == 0:
48                break
49
50        particle_stopped = particle.energy == 0
51
52        return particle_stopped
```

Listing 2: Layer module class.

As described in subsubsection 2.3.2, the detector heads are composed of standard absorbing layers as well as diodes. These diodes are a very important part of the detector, as they allow to convert the particle's deposited energy into induced charge via the creation of electron-hole pairs. The corresponding data is then retrieved and used to evaluate the particle's energy and eventually identify it. A Diode module was thus implemented, inheriting from the Layer class. It specializes it with the induced charge dynamics, in particular through the transfer_energy parameter.

```
1  class Diode(Layer):
2      def __init__(self, Z, density, thickness, transfer_energy) -> None:
3          super().__init__(Z, density, thickness)
4          self.transfer_energy = transfer_energy
5          self.total_deposited_charge = 0
6
7      def absorb_energy(self, particle : prt.Particle, distance):
8          super().absorb_energy(particle, distance)
9          self.update_deposited_charge()
10
11     def simulate_particle_through_whole_layer(self, particle : prt.
      Particle, step_size, display_results=True):
12         self.reset()
13         particle_stopped = super().simulate_particle_through_whole_layer(
      particle, step_size, display_results=False)
14         self.update_deposited_charge()
15
16         return particle_stopped
17
18     def update_deposited_charge(self):
19         nb_electron_hole_pairs = self.deposited_energy/self.
      transfer_energy
20         transfered_charge = nb_electron_hole_pairs * csts.
      elementary_charge # (C)
21         self.total_deposited_charge = transfered_charge * 1e15 # (fC)
```

Listing 3: Diode module class.

Finally, a `Detector` class was implemented as a list of `Layer`s and performs a global simulation of the particle through all of them. Included in Listing 4 is also the definition of the HIDH, following the specifications in [50].

```python
class Detector:
    def __init__(self, name, layers : list[Layer], nb_diodes) -> None:
        self.name = name
        self.layers = layers
        self.nb_diodes = nb_diodes

    def simulate_interaction_particle(self, particle : prt.Particle,
    step_size, display_results=True):
        ...
        for l in self.layers:
            l.reset()
            particle_stopped = l.simulate_particle_through_whole_layer(
    particle, step_size, display_results)

            if particle_stopped:
                break

        diodes, absorbers = self.get_layers_results()
        return particle_stopped, diodes, absorbers

class HIDH(Detector):
    def __init__(self):
        # 1 absorber
        abs1 = Layer(csts.Z_Al, csts.density_Al, 0.01)

        # 2 identical diodes
        thickness_diode = 0.032
        diode1 = Diode(csts.Z_Si, csts.density_Si, thickness_diode, csts.
    transfer_energy_Si)
        diode2 = Diode(csts.Z_Si, csts.density_Si, thickness_diode, csts.
    transfer_energy_Si)

        layers = [abs1, diode1, diode2]

        super().__init__('HIDH', layers, 2)
```

Listing 4: `Detector` class and definition of the HIDH.

3.2.3 Simulation pipeline

This framework is user-friendly. The user must declare the particles and detector to consider along with their parameters and run the simulation. The resulting data is made of the deposited energy of each particle in each diode, the corresponding induced charge and whether the particles stopped or not. These can then be used for processing.

3.3 Advanced simulation with `Geant4`

While the above-described framework is useful to understand the first principles of particles-detector interactions, a dedicated software is necessary to perform accurate simulations and describe more complex configurations. To this end, CERN's `Geant4` software was used in combination with `ROOT` for data analysis. This section gives a brief overview of `Geant4`'s general functioning. More details can be found in [32].

3.3.1 Monte-Carlo simulations for particle physics

`Geant4` is a framework designed to simulate the passage of particles through matter. As is usually the case in high energy particle physics, it relies on *Monte-Carlo* simulations, which assume that the system is described by probability density functions that can be modeled. Instead of solving complicated systems of equations which can take enormous computation time, it performs a large number of experiments using random number generation and builds a statistical result around them.

In the case of particle physics simulations, the Monte-Carlo process is used to follow each particle during its passage through matter. At each step, a particle can interact with the environment in different ways with different probabilities. A random number is generated and, based on it, the behaviour of the particle is decided. An example taken from [57] goes as follows. Assume that the particle is an electron travelling through a gas. At each step, it can ionize the gas with probability p_1, which will result in it losing some momentum and producing new electrons. The associated Monte-Carlo process is:

- Generate a random number $r \in [0, 1]$;

- If $r > p_1$, do nothing: the electron continues on its trajectory;

- If $r < p_1$, simulate ionization: generate new electrons, add them to the simulation list and reduce the initial electron's momentum.

This is repeated at each time step and allows to build a probabilistic model of the particles' interactions with the environment. The result is a statistical distribution assumed to represent the reality. Comparisons with experimental data are conducted to validate these results.

3.3.2 `Geant4` application overview

A `Geant4` application works by implementing several components:

- A *Run Manager*, tasked with controlling the flow of the program and the different events during a run. It is also responsible for initializing the necessary parts of the simulation:

    - The *detector* geometry, material and properties;
    - The *physics* processes and *particles* to be used in the simulation;
    - The *initial event state*, *i.e.* the primary particles properties.

- Optional additional *user-defined actions*, which can be executed during the run;

- An *UI Manager* for visualization purposes.

An example of a `Geant4` simulation output is reported in Figure 16. As described in [7], the setup consists of a target (circle on the left), followed by 6 tracker chambers (cylinders of increasing sizes on the right), all of which contained in a uniform magnetic field. Particles (protons and muons) hit the target and are then deviated by the magnetic field inside the tracker zone (curved trajectories). As `FOCom-PDI`, `Geant4` implements a threshold to kill the particle once it reaches too low energy. This threshold is referred to as *production cut* and is not actually on the particle energy in units of eV. Rather, it has units of length (m) and corresponds to the minimum expected range of the particle in the current material. If the particle is expected to travel less than this range, it is not simulated anymore. This directly correlates to the energy, as higher energy particles go faster and thus travel a wider range. For this work, the defined production cut is 10^{-5} m.
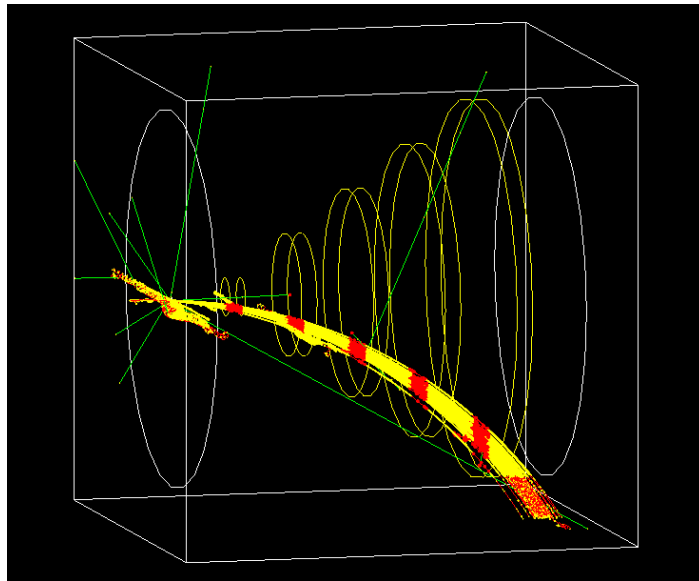
Figure 16: An example simulation output from `Geant4`. *Source: example B2 in the* `Geant4` *documentation [7].*

Many simulations needed to be conducted for this project. Therefore, *macro* files were used to easily set the parameters of the simulation and run them efficiently. The main parameters were:

- Source position and shape. Two types of sources were considered: a point source and a plane source. Their dimensions are given further down in this thesis.

- Source particles angular distribution. Depending on the source, this is necessary to define the orientation of the source particles.

- Source particles energy distribution. As `Geant4` is based on Monte-Carlo principles, the primary energy E of each particle is sampled from a probability distribution $P(E)$. It is defined by its minimum $E_{\min}$, maximum $E_{\max}$ and variation between them. Several options are available, among which *Mono-Energetic* (one fixed value of energy $E_0 = E_{\min} = E_{\max}$ such that $P(E) = \mathbf{1}_{E=E_0}$), *Linear* (with a gradient m such that $P(E) \sim mE$) and *Power Law* (with an exponent α such that $P(E) \sim E^{\alpha}$). An *Inverse Power Law* can also be defined with $\alpha < 0$.

These parameters' values are reported in section 4 in the relevant subsections. The *macro* files were dynamically modified by a custom-written `Bash` script to easily run a sequence of simulations with different initialization parameters. The scripts for the plane source are reported in Appendix B for reference.

3.3.3 `Geant4` simulation model of RADEM

Building on these basic examples allows to develop more complex applications. The goal of this work is to simulate the interactions between the particles and the *Heavy-Ion Detector Head* (HIDH) on RADEM. Figure 17 displays the physical instrument against the `Geant4` model, which had already been developed prior to the start of the project. The three detector heads (respectively for electrons, heavy-ions and protons going in the positive *z* direction) are represented as blue cylinders, while the DDH is the larger blue cylinder in the center of the model. The red portion simulates the effect of the shielding induced by the spacecraft on the instrument.
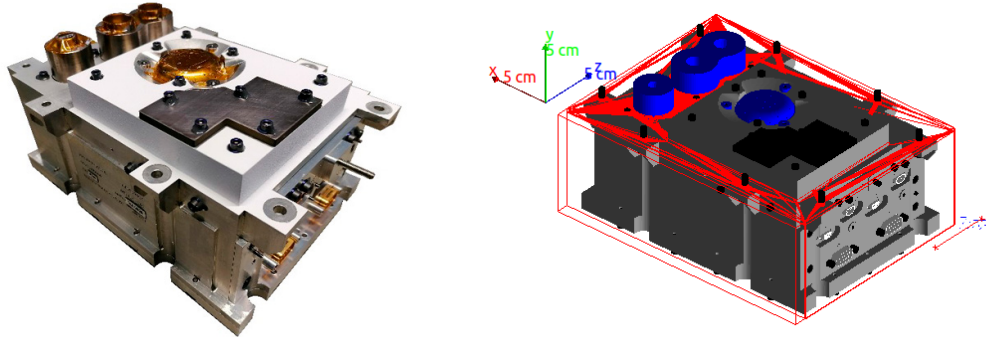
Figure 17: RADEM instrument (left) and its `Geant4` model (right). The blue cylinders are the detector heads and the red parts represent the shielding of the spacecraft around the monitor.

3.4 Data analysis with `ROOT`

`ROOT` [8] is a framework for data analysis, also developed by CERN. It is based on `C++` and provides the user with two main interfaces: an interactive shell for quick execution in a terminal prompt, and a *macro* interface for writing longer scripts. The latter was chosen for convenience. A `Python3` version is available as well, referred to as `PyROOT`. As most of the data analysis in this project was done in `Python3`, this approach was preferred to uniformize the plots and easily transfer data from one program to the other. This was particularly useful when using the `PyCREME`-generated GCRs fluxes in combination with the `Geant4` simulation results. An example of a (simplified) processing script used in this project is available in Appendix C.

4 Numerical simulations of the RADEM response to GCRs particle fluxes

The previous section presented the simulation and analysis tools for this project. This section describes how these tools were used, the simulation settings, the results of these simulations and the conclusions that can be drawn from them. First, the results of the GCRs flux analysis are presented. Then, two simulations settings involving different source shapes are described. The first one, a simple straight beam, gives a comparison between `FOCom-PDI` and `Geant4` simulations in terms of deposited energy. The second one, a plane source, can only be run with `Geant4` and allows to compute various properties of the detector, in particular its field of view, response functions (geometric factors) and count rates. The computations of the count rates are then further extended to account for temporal and spatial variation of the GCRs flux using data generated by `PyCREME`. Finally, an alternative setting on the HIDH is investigated and a conclusion is given. Error analysis and discussion of the simulation parameters are also reported in the relevant subsections.

4.1 GCRs flux analysis with `PyCREME`

Using `PyCREME`, a GCRs flux was simulated for a given date (January 11th 2019). The choice of the date is arbitrary and does not influence the analysis in this section. The variation of the GCRs fluxes over a long period of time will be studied in subsection 4.4. The results are reported in Figure 18. As can be seen, the most abundant elements are Helium ($z = 2$), Carbon ($z = 6$), Nitrogen ($z = 7$) and Oxygen ($z = 8$) with main energy range in $[10^1, 10^3]$ MeV/AMU[4] (black dashed lines). The flux intensity exhibits a bell shape in a double-log depiction, with its peak at around 150 MeV/AMU. Helium fluxes are about two orders of magnitude above the others and Carbon, Nitrogen and Oxygen one order of magnitude above the rest. These results correspond to the ones previously reported in Figure 3.
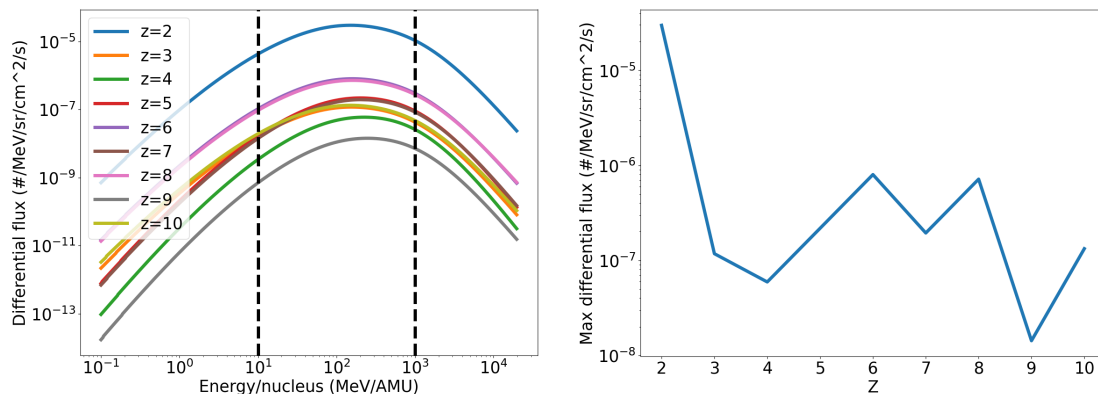
Figure 18: GCRs particle flux simulation with `PyCREME`. Left: differential flux as a function of the primary energy. The most abundant elements are Helium ($z = 2$), Carbon ($z = 6$), Nitrogen ($z = 7$) and Oxygen ($z = 8$) with main energy range in $[10^1, 10^3]$ MeV/AMU (black dashed lines). Right: maximum differential flux for each element. This confirms the findings on the left panel, as the highest peaks are found for $z = 2, 6, 7, 8$.

---

[4]AMU stands for *Atomic Mass Unit* and is approximately equal to the number of nucleons of the considered particle.

This allows to specify the particles used in the simulations. Helium, Carbon, Nitrogen and Oxygen particles were simulated through the detector with energy range $[0.05, 23]$ GeV. The choice of this energy range will be justified in a following subsection. Since most particles are expected to be on the lower end of the energy spectrum, an Inverse Power Law was used for the energy distribution in subsequent simulations. This was also useful for practical reasons, as lower energy particles are stopped more easily in the material. The overall simulations thus took less time and accumulating a significant number of events was easier. Various source shapes were considered for different purposes. The settings and results of these simulations are described in the following subsections.

4.2 Point source `Geant4` simulation and comparison with the first order principles

The first source shape is a point source, resulting in a straight beam of particles shooting right in the middle of the *Heavy-Ion Detector Head*. The `Geant4` setting is shown in Figure 19, where the vertical blue line represents the incoming beam of particles which interact with the different layers and scatter (red lines and yellow dots), depositing energy in the process. The *Shielding* physics list was used for these simulations.
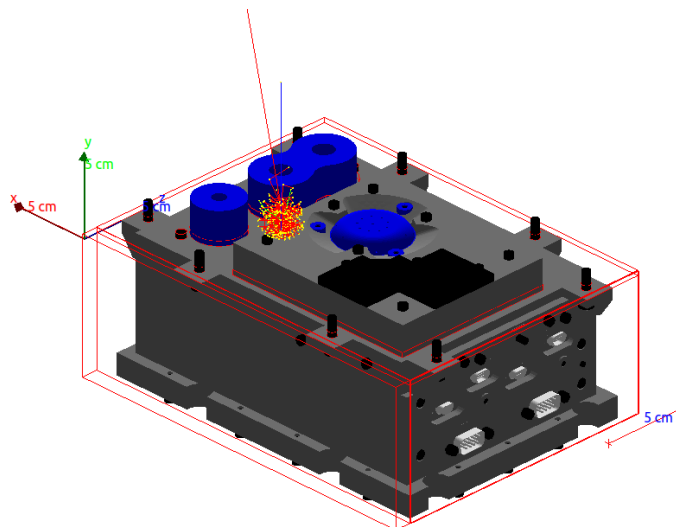
Figure 19: `Geant4` simulation output for a straight beam of Oxygen particles on the HIDH.

By design, `FOCom-PDI` only allows to simulate such a simple setup, so no particular setting was required. For each type of particles (He, C, N, O), the primary energy range $[0.05, 23]$ GeV was simulated with a uniform discrete grid of 500 points. The software performs the computation for the passage of the particle through each layer and keeps track of the deposited energy measured by the two diodes.

The `Geant4` simulations were parameterized following the *macro* file configuration described in subsubsection 3.3.2. The parameter values were set to simulate a point source centered on the HIDH and facing straight down. They are reported in Table 3. As `Geant4` is based on Monte-Carlo simulations, a high number of particles is needed to have significant statistics. 10000 particles of each type were simulated following this requirement.

Table 3: Point source configuration for the `Geant4` simulation.

Parameter	Value
Source type	Beam
Source shape	Circle with 0.05 mm radius
Number of particles	10000
Energy distribution	Uniform in [0.05, 23] GeV

Figure 20 reports the results of these simulations for GCRs particles. The four colored lines each represent an element: Helium (purple), Carbon (blue), Nitrogen (orange) and Oxygen (green) for the HIDH diodes 1 (left subplot) and 2 (right subplot). The objective of these results is solely to get an initial estimate of the particles' interactions with the detector and to compare the two simulation frameworks. This is represented by the two linestyles in the figure. The simple solid lines are the results of the `Geant4` simulations and the lighter lines with black outlines are the `FOCom-PDI` results. A first observation is that the mean deposited energy is consistently higher for heavier elements. This is because these elements tend to interact more with the medium and hence deposit more energy. However, the profiles for all particles follow the same exponential decrease. As a particle's primary energy increases, its speed increases as well and it will travel faster through the medium, interacting less with it and depositing less energy. This trend is also visible in the stopping power in Figure 13. Note that the decrease becomes less important as the energy increases, until it reaches saturation. The trends are the same between diode 1 and diode 2 as no lower deposited energy thresholds are set on them. There is also a difference in the actual values of the mean deposited energy due to the fact that particles have to go through the first diode before reaching the second one, hence losing energy in the process. However, as no thresholds were set, this difference is minimal.

Comparing the output, it can be seen that the first order computation scheme (solid lines with black outlines) yields similar results to the Monte Carlo simulations (simple solid lines), indicating that these principles are indeed correct. There are nevertheless a few noticeable differences. The sudden peaks and drops in the `Geant4` curves come from the use of histogram bins to capture the randomness of the Monte-Carlo process and represent the fluctuations in the statistics. Lower statistics for specific values correspond to fluctuations in the curve. A more important difference is found in the energy cut-offs of the particles. The `FOCom-PDI` curves are non-zero for higher values of the primary energy compared to the `Geant4` ones. This is especially visible on the Carbon (blue) curves. In other words, the minimum deposited energy of a particle must be higher to register a hit using the first principle calculations. The cause of this phenomenon is still uncertain but might come from the approximation used in the first order framework. Several values of the step-size were tested to assess its influence on the results but this did not yield any noticeable variation. Despite these minor differences, the plots validate the first order framework as a good approximation of the `Geant4` model. However, as described in the next section, `FOCom-PDI` cannot be used for accurate characterization of the detector's properties because of its limitations.
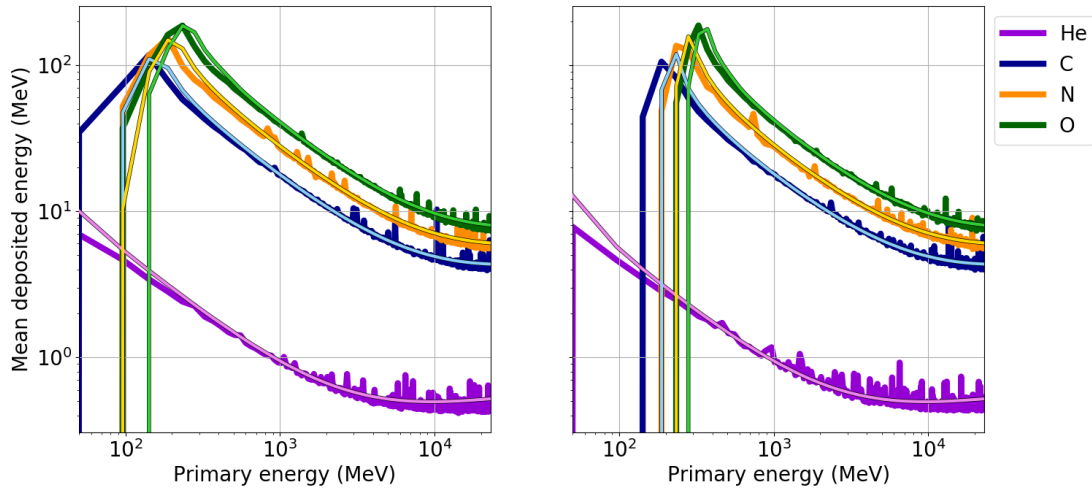
Figure 20: Particle-detector interaction simulation with `Geant4` (simple solid lines) and `FOCom-PDI` (lighter lines with black outlines) between a straight beam of GCRs particles and the HIDH diodes 1 (left) and 2 (right). No lower threshold is set on the diodes.

An important aspect to note is that these simulations were run considering no lower threshold on the diodes. This implies that light elements like Helium are still registered even though their deposited energy would not be enough to trigger a response in the detector. This is also why the actual values and profiles of the two diodes are so similar, as particles with GCRs energies do not lose a lot of energy by going through the first diode.

4.3 Plane source with `Geant4` and characterization of the HIDH response

The goal of the point source setting was to validate the first order framework and get a first idea of the energy deposition profiles in the detector. However particles in space do not collide with the detector in a straight beam in the center of the head but are omni-directional. Consequently, simulations with a more realistic setting assuming an omni-directional flux were performed. From these simulations, detector characteristics like its field of view and count rates were then computed. The following subsubsections are dedicated to this setup. The same analysis on the deposited energy was first performed to obtain the relation between primary energy and deposited energy and evaluate the effect of the deposited energy cutoff (lower threshold). Other detector properties such as the FOV and, more importantly, the geometric factors, were also computed. The justification for the chosen energy range is described in the last subsubsection.

4.3.1 Plane source setting

A simple plane source setting was defined using a square situated 10 mm above the detector and particles uniformly distributed (in position and angle) on it. The *macro* configuration is reported in Table 4. Contrary to the point source case, not all particles will interact with the detector, so a greater number of them had to be simulated.

36

Initially, 10 simulations of 10^5 particles each were run for each element in the energy range $[0.05, 3]$ GeV, amounting to a total of 10^6 particles per element. The primary energy distribution followed an Inverse Power Law with $\alpha = -\frac{1}{4}$. However, it was later apparent that a greater range of energy had to be considered. Indeed, the results in subsection 4.1 show that the energy range of GCRs elements is $[10^1, 10^3]$ MeV/AMU. The corresponding energy range can then be obtained by multiplying this range by the number of nucleons in the relevant elements. For instance, an Oxygen nucleus contains 16 nucleons, so that the maximum energy is around 20 GeV. This was also visible from the computed quantities described in the following subsubsections, as stabilization was not attained for too low energies. A more in-depth analysis is found in subsubsection 4.3.6.

Since simulations involving numerous particles at higher energy require significantly longer computation times, a choice had to be made regarding the number of simulated particles. 10 additional simulations of 10^4 particles each were run, following a uniform distribution in steps of 2 GeV until 23 GeV. In other words, simulation 11 involved 10^4 particles with energy uniformly distributed in $[3, 5]$ GeV, simulation 12 involved 10^4 particles with energy uniformly distributed in $[5, 7]$ GeV and so on until simulation 20 and energy range $[21, 23]$ GeV. These additional simulations thus involved a total of 10^5 particles per element with energy uniformly distributed in $[3, 23]$ GeV.

Table 4: Plane source configuration for the `Geant4` *simulation.*

Parameter	Value
Source type	Plane
Source shape	50 mm × 50 mm rectangle
Source particles angular distribution	Half-sphere towards the detector
Energy distribution	Inverse Power Law $\alpha = -\frac{1}{4}$ in $[0.05, 3]$ GeV, Uniform in $[3, 23]$ GeV

Because of the simulation constraints, there is an important difference in the quantity of available data between energy ranges $[0.05, 3]$ GeV (10^6 particles for a $\simeq 3$ GeV spread) and $[3, 23]$ GeV (10^5 particles for a 20 GeV spread). This influences the statistics and confidence of the subsequent computations. Nonetheless, the results presented in the following subsubsections have a good statistical significance. A more rigorous analysis of the error induced by the Monte-Carlo process is described futher down in this thesis report. It is to be noted that in order to increase readability of the pictures, the parts of the curves corresponding to the lower statistics energy range $[3, 23]$ GeV are smoothed out using a Savitzky-Golay [55] filter of degree 1 with a window of size 21.

Figure 21 displays a graphical representation of the plane source setting with a focus on the HIDH. The second panel represents what is expected from the simulations. The particles originate from the plane with various directions and energies. Particles within the field of view and with an angle less than half of it will almost always penetrate the aperture and interact with the diodes if they pass the absorber. Particles outside the field of view can only interact with the diodes if their energy is high enough to make them penetrate the collimator. These theoretical considerations are compared with the simulations results in subsubsection 4.3.3.
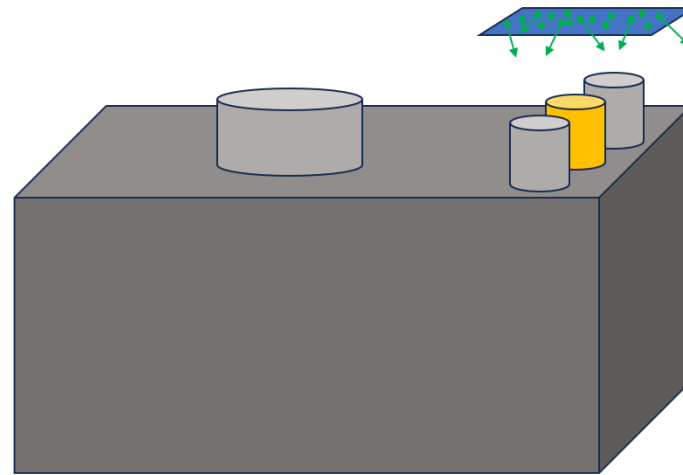
(a) Wide view.
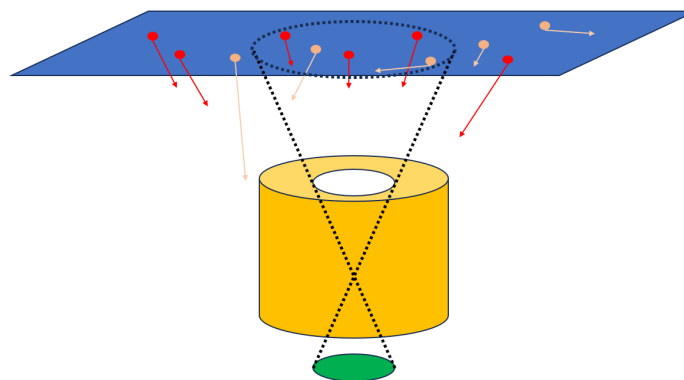
(b) Focus on the HIDH.

Figure 21: Graphical representation of the plane source setting. Panel (a): wide view of the whole RADEM monitor with the detector heads. The HIDH is in orange and the blue plane represents the virtual source plane with primary particles in green originating from it. The arrows indicate the particles' velocities. Panel (b): close-up view of the HIDH with the virtual source plane. The dashed black lines indicate the theoretical field of view defined from the green diode as in Figure 14. The particles have different initial directions represented by the arrows and different energies represented by their lengths. Their colors indicate whether they will hit the diode (red) or not (beige). The red particles are either well oriented and inside the field of view, or energetic enough to penetrate the collimator and interact with the diode.

While this setup is more realistic, it remains a simplified version of the actual configuration in space. Because of the three-dimensional nature of the environment, particles can come from multiple sides of the monitor and penetrate the shielding with enough energy. This is not captured by a simple 2D simulation with a plane source. However, these represent a minority of hits when compared to the ones induced by particles entering the detector through the aperture. This will be further investigated in subsubsection 4.3.3.

38

4.3.2 Deposited energy

As for the point source, the mean deposited energy can be plotted against the primary energy of a particle from the plane simulation results. Note that the first order framework does not allow to take into account a plane source setting and particle trajectories different than a straight beam. Therefore, comparing its output to the `Geant4` plane simulations output should yield significant differences. These results are displayed in Figure 22. The plot visuals are the same as in Figure 20. The four colored lines each represent an element: Helium (purple), Carbon (blue), Nitrogen (orange) and Oxygen (green) for the HIDH diodes 1 (left subplot) and 2 (right subplot). The two linestyles correspond to the `Geant4` (simple solid lines) and `FOCom-PDI` (lighter lines with black outlines) simulations.
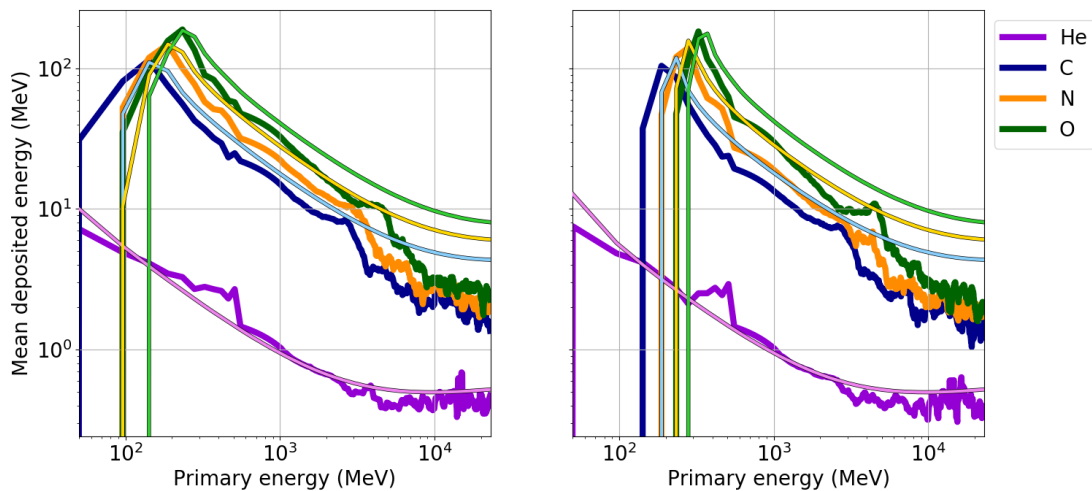
Figure 22: Particle-detector interaction simulation with `Geant4` (simple solid lines) and `FOCom-PDI` (lighter lines with black outlines). `FOCom-PDI` simulates a simple straight beam of GCRs particles and `Geant4` a plane source set as in Table 4. The subplots correspond to the HIDH diodes 1 (left) and 2 (right). The `Geant4` curves corresponding to primary energies greater than 3 GeV are smoothed out to increase readability. No lower threshold is set on the diodes.

While Figure 22 is very similar to Figure 20, it can be seen that higher energy particles deposit less mean energy in the case of the plane source. This comes from the two-dimensional nature of this setting. As described in the previous subsection, particles coming from the plane source can penetrate the collimator and hit the diodes if they are energetic enough. However, high energy particles also deposit less energy because of the stopping power trend (cf Figure 13). This means that they deposit less energy on the diodes, which brings down the mean deposited energy. The statistics are also notably lower than before for these energies, as only a few of these randomly generated particles are initialized with the right set of parameters to match these conditions.

The observations in this subsubsection further cement the importance of running first order simulations with a simple setting. The beam source setting was fast to implement with these principles and could be run in a few minutes. However, they also demonstrate why this approach is not sufficient for accurate simulations, as the three-dimensional nature of the space environment implies that particles follow more complex trajectories than a simple

straight line through the aperture. This results in different interactions with the radiation monitors which have to be accurately modelled for precise characterization of their detector's properties. Therefore, the rest of the analysis only relies on the `Geant4` simulation results.

4.3.3 Field of view

As previously described in subsubsection 2.3.3, the HIDH's field of view is $\eta = 45°$ and the incidence angle of the particles hitting the two diodes is $\theta = \frac{1}{2}\eta$ (cf Figure 15). Therefore, computing θ from the output of the plane simulation should yield a normal distribution centered around $\frac{1}{2}\theta = 11.25°$. However, this only takes into account particles going through the aperture, not high energy particles able to go through the collimator, as those can reach the diodes even without being inside of the field of view. In order to validate the field of view of the detector, the incidence angles have been computed from the output of a simulation with a reduced energy range $[0.05, 1]$ GeV and with the full range $[0.05, 23]$ GeV for comparison. The results are displayed in Figure 23. The angle of incident particles is plotted as a histogram for each element in a GCRs flux. The counts are normalized to ease the comparison of the various elements. Both simulations were run considering a zero-thresholds configuration on the detector.

From Figure 23a, the incidence angle of Carbon, Nitrogen and Oygen particles interacting with diodes 1 and 2 is shaped like a normal distribution in the range $[0°, 22.5°]$, which is half of the field of view, as expected. The Helium particles reach higher values, with a distribution in the range $[0°, 40°]$. This is due to the fact that lighter particles like Helium interact less with the medium with respect to heavier particles. They deposit less energy and are hence able to travel greater distances through dense mediums. Thus, even with a reduced energy range, Helium particles outside the field of view are still able to penetrate the collimator and reach the diodes by going through it. Therefore, for the same energy, the collimator is more efficient for heavier particles. Another aspect to note is that the angle reaches slightly higher values for the first diode than for the second diode. This is explained by the fact that the field of view is defined from the second diode. Note that even if the count values for the second diode are higher than for the first one in Figure 23a, this does not mean that more particles hit the second diode. The complete density distribution is normalized here, so that the counts appear higher when in reality the total number of counts is smaller for diode 2 than for diode 1.
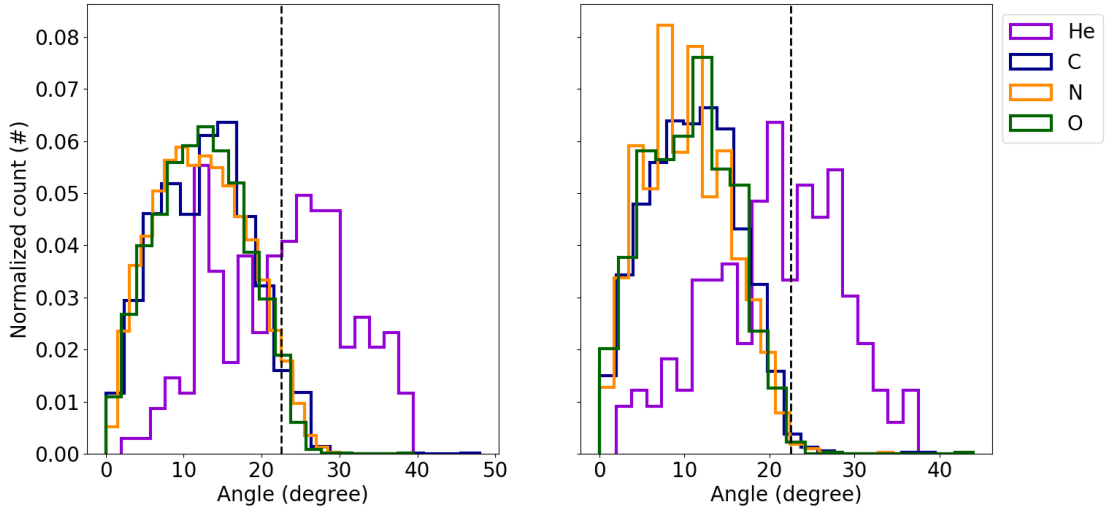
(a) Reduced range $[0.05, 1]$ GeV.
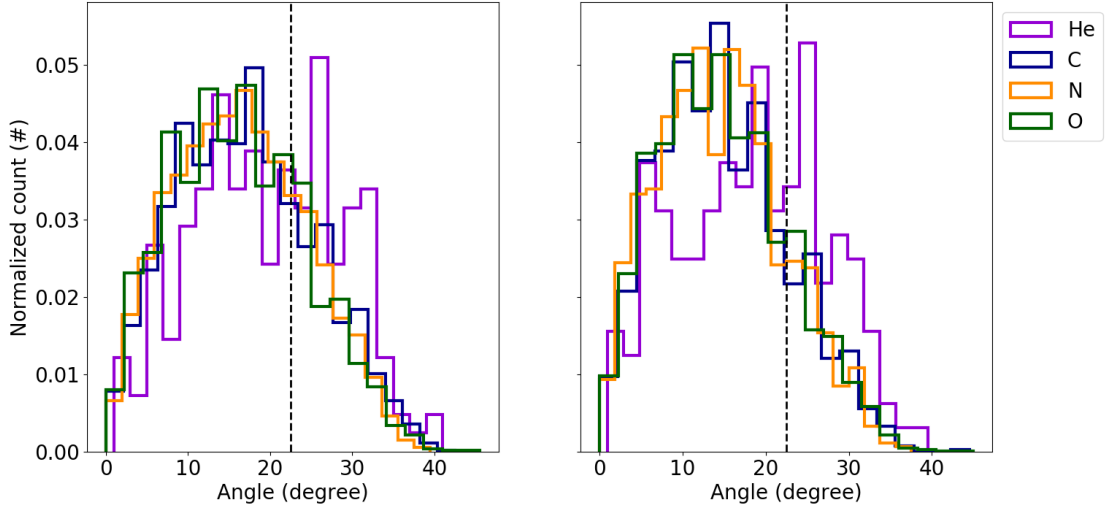
(b) Full range $[0.05, 23]$ GeV.

Figure 23: Normalized distribution of the primary angle of source particles hitting diodes 1 (left) and 2 (right). Top: reduced energy range $[0.05, 1]$ GeV *to only take particles going through the aperture. Bottom: full energy range* $[0.05, 23]$ GeV. *No lower threshold is set on the diodes.*

Penetrating heavy ions can also go through the collimator and hit the diodes even though they started from outside the field of view of the detector. This is especially visible in Figure 23b with the full energy range. In this case, the incidence angle of the particles reaches values much higher than the expected $\theta = 22.5°$. Particles with energies of several GeV are indeed more likely to fully go through the collimator and hit the diode afterwards. However, the distribution is still a bell shape centered around $\frac{1}{2}\theta$, only with a bigger tail for higher values of the angle. Note that these computations were run considering a zero-thresholds configuration on the detector, so that even particles depositing a negligible amount of energy will register as a hit.

41

While the primary particles' direction allows to validate the detector's field of view, their position on the starting plane source yields informative results as well. Displaying these positions on a grid as in Figure 24 allows to determine the spatial distribution of interacting particles. The two circles represent the detector head geometry from a top view: aperture (green) and collimator (black). Note that these figures do not display the positions of the particles on the detector itself, but on the source plane (blue rectangle in Figure 21). The circles are obtained by projecting the detector geometry onto the source plane. These plots are density plots of the position of particles hitting both diodes. In other words, if a particle with given starting position (x, y) on the source plane hits a diode after simulation, its position is added to a two-dimensional histogram. These datapoints are then plotted as a two-dimensional density distribution over the coordinates x, y on the source plane, represented by the colorscale. The circles are just projections of the detector geometry for visualization purposes. The resulting plots are expected to form a two-dimensional Gaussian distribution centered on the detector's aperture, as particles closer to the center are more likely to hit both diodes than particles on the side.

As can be seen on Figure 24, the position of source particles hitting the diodes indeed forms a two-dimensional Gaussian distribution centered on the aperture. Particles outside the aperture can be nonetheless within the field of view and still hit the diodes. Finally, high-energy particles can go through the collimator and register a hit even though they are far from the center. This is especially visible on the top subplots corresponding to the lighter Helium particles. Since light elements interact less with the medium, they can travel further inside and reach the diodes from the side. This correlates to the higher values of the angle for Helium particles found in Figure 23. Note that this effect decreases as the atomic number increases. Carbon particles are more centered around the aperture than Helium, but less than Nitrogen and Oxygen. In addition, as this figure displays the position on the source plane, the actual extent of the dispersion is dependent on the placement of the source. Since the field of view is fixed, a plane source placed higher would result in a wider dispersion around the head, not necessarily contained in the collimator circle.
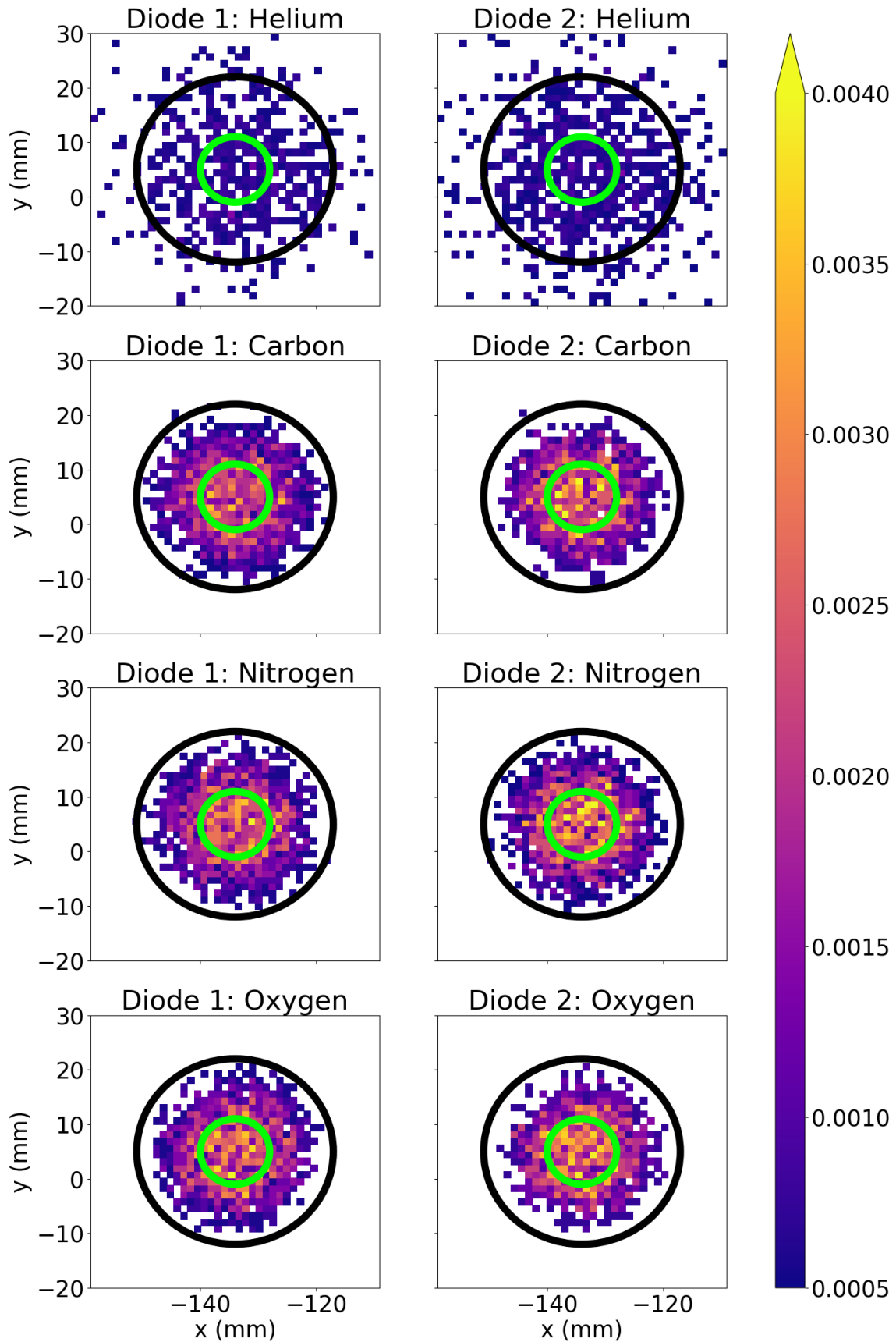
Figure 24: Normalized density distribution of the primary position of source particles hitting diodes 1 and 2. Top view of the HIDH. The circles represent the detector's aperture (green) and collimator (black) projected onto the source plane.

4.3.4 Geometric factor

The geometric factor has been described in subsubsection 2.3.4. As a reminder, the theoretical values G_i of each diode $i \in \{1, 2\}$ can be computed from their radii R_i and depths l_i as:

$$G_i \;=\; \frac{1}{2}\pi^2[R_0^2 + R_i^2 + l_i^2 - \sqrt{(R_0^2 + R_i^2 + l_i^2)^2 - 4R_0^2 R_i^2}], \; i = 1, 2. \tag{12}$$

The theoretical values computed from Equation (12) for diodes 1 and 2 are respectively $G_1 = 0.20$ cm^2·sr and $G_2 = 0.15$ cm^2·sr. G_2 is smaller than G_1 since more particles hit the first diode than the second one and the latter is deeper inside the detector than the former.

These values are theoretical and correspond to an ideal setup. In practice, the geometric factors can be computed from the simulation results as weighted ratios of the particles hitting the diodes $N_i(E)$ over the total number of incident particles $N(E)$. They are functions of the primary energy of the particles and can be computed via:

$$\tilde{G}_i(E) \;=\; A\pi\frac{N_i(E)}{N(E)}, \tag{13}$$

In this setting, the source area is $A = 5 \times 5 = 25$ cm^2.

The effective values of the geometric factors as a function of the particles' primary energy were computed from Equation (13). Figure 25 displays the theoretical and computed geometric factors of the two HIDH channels for the main GCRs particles (Helium, Carbon, Nitrogen and Oxygen). Since the geometric factors depend on the effective threshold of the channels, different plots are obtained depending on the chosen combination. Figure 25a reports the results for no threshold ($t_1 = 0$ DAC, $t_2 = 0$ DAC) and Figure 25b the current setting on the HIDH ($t_1 = 52$ DAC, $t_2 = 244$ DAC). The black dashed lines represent the theoretical values computed from Equation (12).
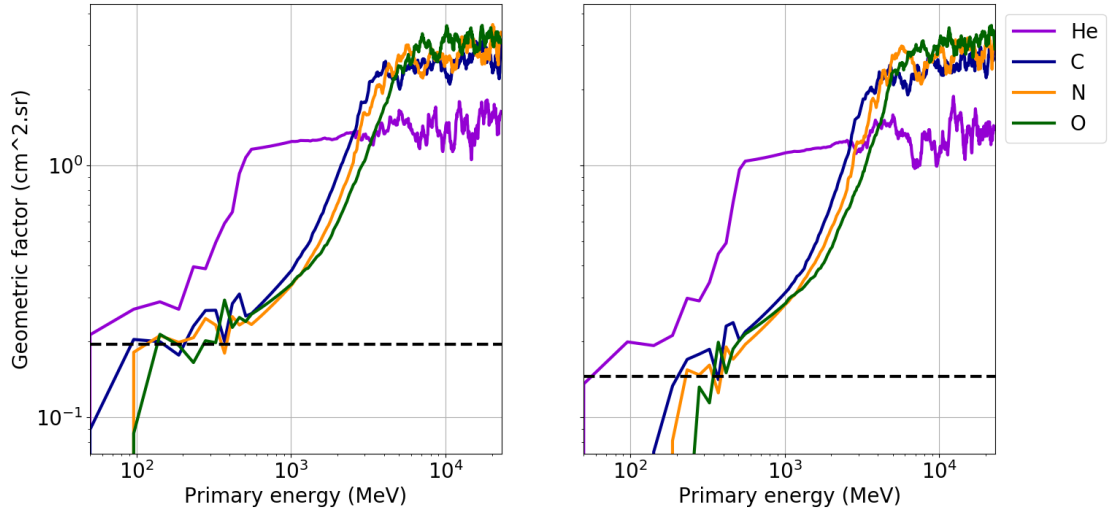
(a) No thresholds on the diodes: $t_1 = 0$ DAC, $t_2 = 0$ DAC.
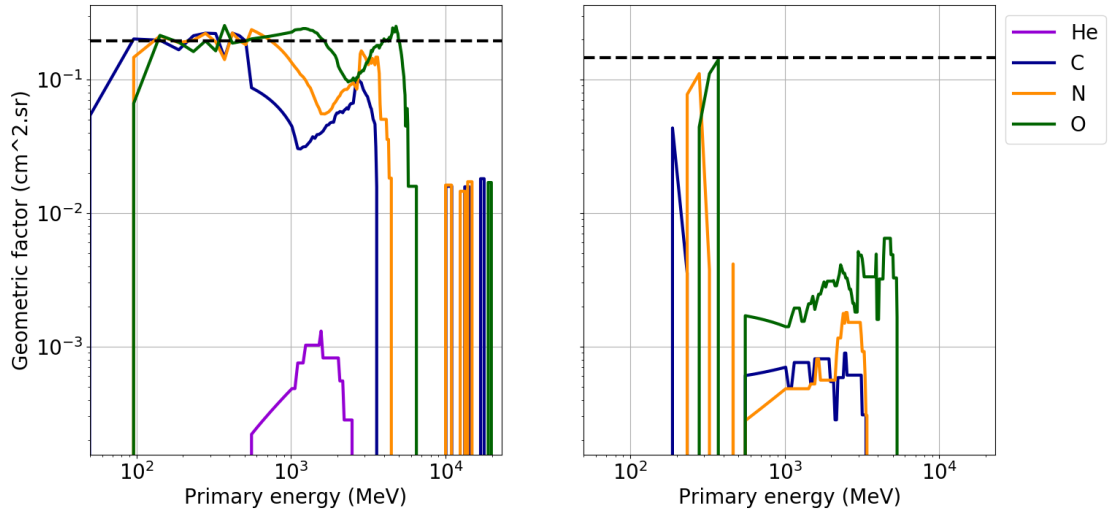
(b) Current thresholds on the diodes: $t_1 = 52$ DAC, $t_2 = 244$ DAC.

Figure 25: Geometric factors computed from the plane simulations with Equation (13). The subplots correspond to the HIDH diodes 1 (left) and 2 (right) and different lower thresholds combinations on the diodes (top: no thresholds, bottom: current thresholds). The part of the curves corresponding to primary energies greater than 3 GeV are smoothed out to increase readability. The black dashed lines represent the theoretical values G_1 and G_2 computed from Equation (12).

The computations with no thresholds (Figure 25a) yield a curve with a step function-like shape for low energies, corresponding to the minimum required energy to reach the diodes. The effective geometric factors match the theoretical values for low energy particles. For higher energies, the computed geometric factors increase above this value. This is because highly energetic particles can penetrate the collimator and still interact with the diodes, even if they do not go through the aperture. This creates a variation in the theoretical setting considered in Equation (12). As particles outside the aperture can reach the diodes, this is effectively the same as increasing the value of the radius of aperture R_0 in the theoretical setting, which would increase the value of the theoretical geometric factor. The relative posi-

tions of the curves are also interesting to study. For low primary energy, the geometric factor decreases with the atomic number (the Oxygen curve is below the Carbon, which is below the Helium). This trend is then reversed for higher primary energies. This can be explained by the physics of particle interaction with matter. Firstly, lighter particles interact less with the medium, so that they can penetrate the first Aluminium absorber more easily. This is visible for low primary energies. Secondly, as the energy increases, the stopping power of the elements in the medium decreases, so that particles interact more with the diodes (cf Figure 13). This decrease is different from one element to another because heavier elements lose energy faster than lighter ones. The geometric factor curves for heavier elements corroborate this assumption, as they stabilize after higher primary energies than for Helium elements. For high energy, the curves are also higher for heavy elements. It is thought to be due once again to the fact that heavier elements interact more with the medium, and in particular the diodes. This results in more hits and thus higher values of the geometric factor.

On the other hand, the non-zero thresholds combinations plots (Figure 25b) exhibit a square-like shape with a first spike to a constant value, later followed by a drop and a lower valued tail. The initial spike corresponds to the minimum primary energy needed to deposit enough energy on the diode for the hit to be registered. The following drop represents the trend of the stopping power for highly energetic particles (cf Figure 13): as these go faster and interact less with the matter, they deposit less energy. Therefore, particles with energy above a certain value will not deposit as much energy as the low energy ones and trigger less response in the diodes, leading to a smaller geometric factor. This also explains why the geometric factors remain constant around the theoretical values in that case, as highly energetic particles do not necessarily trigger more readings in the diodes. The geometric factors are much lower for Helium particles, and even zero for the second diode. This is because they deposit less energy than heavier particles (cf Figure 22). Since this configuration involves non-zero thresholds, their deposited energy is below the threshold and the interaction is not registered as a hit, resulting in a zero geometric factor.

In both cases, the geometric factor values are lower for diode 2 than for diode 1. As for the deposited energy, this is explained by the fact that more particles hit the first diode than the second since they need more energy to reach the latter. As the geometric factor is proportional to the number of particles hitting the diode, it is lower for diode 2 than for diode 1. This phenomenon is amplified by the higher threshold on the second diode in the current thresholds configuration.

4.3.5 Count rates

The expected count rates R_i of the diodes can be inferred from the local particle flux $\varphi(E)$ and the geometric factors $G_i(E)$ via:

$$R_i \quad = \quad \int_0^\infty \varphi(E) G_i(E) \mathrm{d}E. \tag{14}$$

This formula can be used to compute the effective count rates $\tilde{R}_i$ of each channel from the simulation results. The geometric factor $\tilde{G}_i$ was obtained from Equation (13) in the previous subsubsection and the flux $\varphi(E)$ was recovered from the `PyCREME` output in subsection 4.1. The numerical integration was performed using the trapezoidal rule with primary energy E ranging in the previously defined interval $[E_{\min}, E_{\max}] = [0.05, 23]$ GeV.

$$\tilde{R}_i = \int_{E_{\min}}^{E_{\max}} \varphi(E)\tilde{G}_i(E)\mathrm{d}E$$

$$\simeq \sum_{k=1}^{N} \frac{\varphi(E_{k-1})\tilde{G}_i(E_{k-1}) + \varphi(E_k)\tilde{G}_i(E_k)}{2}\Delta E_k. \tag{15}$$

Equation (15) yields a single number representing the number of counts per second on the channel. As previously discussed, the goal of this work is to describe the influence of the detector's lower thresholds on its readings. Therefore, the count rates were computed with thresholds varying in the range allowed by the Digital Analog Converter $[C_{\min}, C_{\max}]$ (cf subsubsection 2.3.3). This allowed to describe each diode's count rates as a function of its lower threshold. Since increasing the lower threshold is equivalent to increasing the minimal required deposited energy of a particle to register a hit, the count rates are expected to decrease with the thresholds.

Figure 26 displays the two HIDH channels count rates as functions of their respective lower thresholds. As expected, increasing the thresholds induces a decrease in the count rates, until a threshold too high is reached and no count is registered. Moreover, the maximum threshold value reached for diode 2 before the count rates drop to 0 is lower than for diode 1. This is due to the fact that more particles reach the first diode than the second one since they have to go through more matter to reach the latter. This trend was already visible on the deposited energy (Figure 22) and geometric factors (Figure 25b) plots.
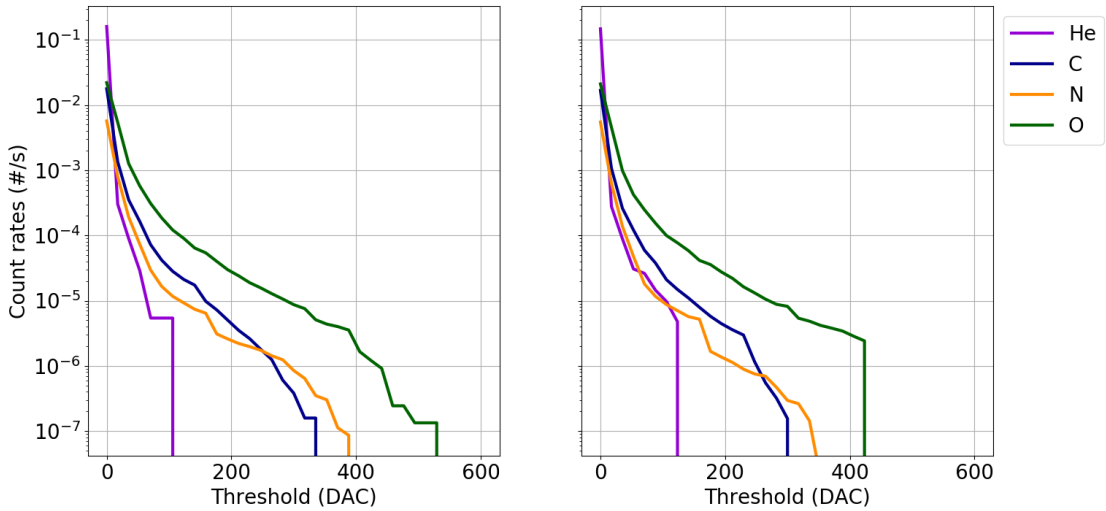
Figure 26: Count rates computed from the plane simulations with Equation (14) as a function of the diodes' lower thresholds. The subplots correspond to the HIDH diodes 1 (left) and 2 (right).

The relative positions of the curves carry information as well. Firstly, the count rates corresponding to lighter elements drop faster than for heavier elements (the purple Helium curve drops to 0 count/s for $t_1 \simeq 120$ DAC against $t_1 \simeq 530$ DAC for the green Oxygen curve). This is explained by the results presented in Figure 22: lighter elements deposit less energy, so that increasing the diodes' lower thresholds influences them faster than heavier elements. Secondly, while not perfectly apparent from the plots, the actual values of the count rates

first follow the atomic number in descending order before quickly inverting the trend to follow it in ascending order for bigger thresholds. Another way to see it is that for low threshold values, lighter elements induce more hits; then, as the thresholds increase, the heavier elements curve drop slower and reach higher values of the threshold before not interacting with the diodes anymore. This is explained by the fact that heavier elements interact more with the medium and deposit more energy. Even with a high threshold value, interactions with high energy particles are still registered as they deposit a lot of energy, allowing them to overcome the thresholds.

4.3.6 Validation of the energy range

In subsection 4.1, the interval $[0.05, 23]$ GeV was defined as reference energy range for the simulations. As high energy cosmic rays are particularly dangerous, it is reasonable to question this choice. This subsubsection is dedicated to its justification and explains what considerations were made to settle on this interval, as well as why it is believed to be enough for this analysis.

Firstly, as previously mentioned, simulations with a high number of high energy particles require long computation times. The limited resources did not allow to run all desired simulations in the timeframe of this project, hence choices had to be made. It was already described how simulations 11 to 20 with high energy elements were run with significantly less particles in order to get the results in a reasonable amount of time. This reduces the statistics of these results, but these are nonetheless satisfying and allow to get a good estimate of the detector properties studied in this work. Limiting the energy range to $[0.05, 23]$ GeV was also a part of these compromises. As described in the previous subsections, the detector's field of view, geometric factors and count rates were well computed and characterized. While additional simulations could improve the results, the project goals were achieved here.

Secondly, quantitatively studying the role of higher energy particles shows that this range is indeed enough to yield satisfying results. Note that the numerical computation of the count rates in Equation (15) depends on the upper bound $E_{\max}$, so that $\tilde{R}_i = \tilde{R}_i(E_{\max})$. If $E_{\max}$ is increased, the integration is done on a wider range of energies, so that the count rate increases and the computation gets more accurate. However, as the GCRs particles flux decreases for high energy (cf Figure 18) and the stopping power for high energy particles decreases too (cf Figure 13), $\tilde{R}_i(E_{\max})$ is expected to converge at a given energy, meaning that particles with energy above a certain value do not modify the value of the count rates anymore. This behaviour is also expected for the numerical geometric factor. As described in Equation (13), $\tilde{G}_i(E)$ is a function of the primary energy E of a particle. With the same considerations, $\tilde{G}_i(E)$ is expected to stabilize for E greater than a certain value.

To assess this hypothesis, the count rates $\tilde{R}_i(E_{\max})$ have been computed as a function of the maximal energy used in the numerical integration in Equation (15) $E_{\max} \in [0.05, 23]$ GeV. Figure 27 and Figure 28 display the results for the zero-thresholds and current thresholds configuration. The top subplots report the count rates, while the bottom subplots report their numerical derivatives computed by finite central difference. The colors represent the usual GCRs elements: Helium (purple), Carbon (blue), Nitrogen (orange) and Oxygen (green).
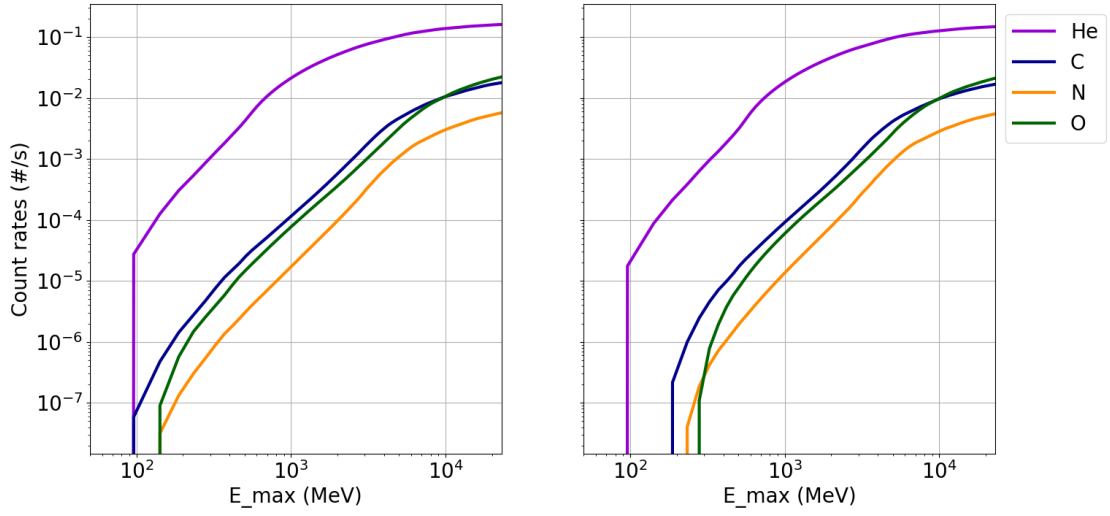
(a) Count rates.
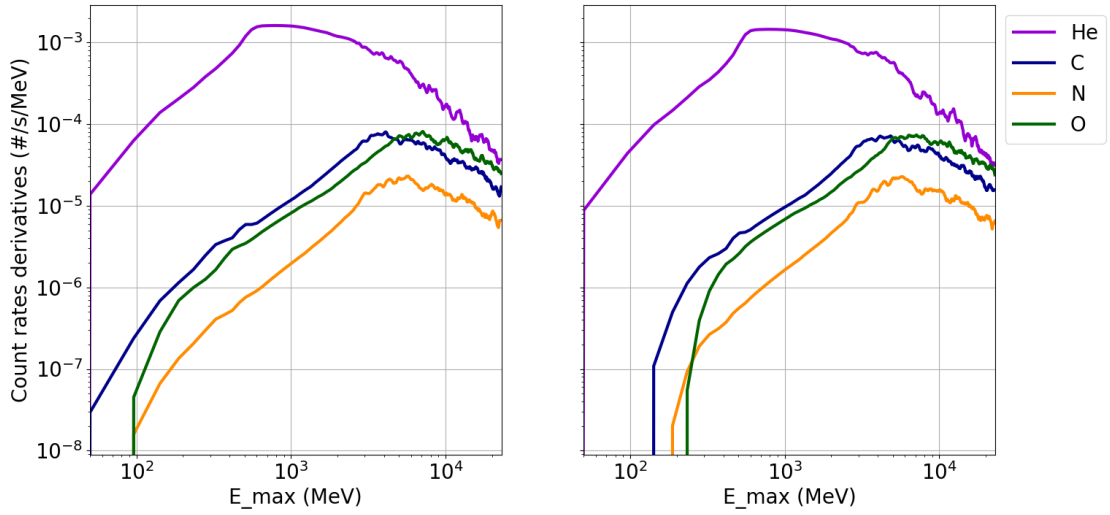
(b) Count rates derivatives.

Figure 27: Count rates and their numerical derivatives computed from the plane simulations as a function of the maximal energy used for numerical integration in Equation (15). The subplots correspond to the HIDH diodes 1 (left) and 2 (right). Top: count rates. Bottom: count rates numerical derivatives. No thresholds are set: $t_1 = 0$ DAC, $t_2 = 0$ DAC.

The results from the zero-thresholds configuration show that, as expected, the count rates increase when E_{max} increases. At some point, they start stabilizing, and their derivative decreases. This inflexion point is found around 400 MeV for Helium particles and around 3 GeV for Carbon, Nitrogen and Oxygen. The derivatives steadily decrease and the count rates stabilize more and more after that. This stabilization is also visible on the geometric factors in Figure 25a, where the values clearly stabilize after the primary energy E of the particles reaches the values mentioned above. It is interesting to note that heavier elements stabilize later than lighter elements. This is explained by the results displayed in Figure 18. The differential flux in this figure is expressed as a function of the energy per nucleon. Heavier elements possess more nucleons, so that the total energy of a particle can reach higher values for these elements before their corresponding GCRs flux sufficiently decreases. In Figure 27, the count rates converge after the maximum energy $E_{max} = 23$ GeV, which could indicate that this value is not high enough for this analysis. However, note that these results depend on the thresholds configuration. As previously mentioned, high energy particles can penetrate the collimator from outside the detector's field of view and still deposit some energy on the diodes, increasing the count rate. Moreover, the count rates values are always higher for light elements than for heavy elements. This was already visible in Figure 26 and described in subsubsection 4.3.4 and is simply a consequence of the results in Figure 18, as the Helium flux is much higher than the others, inducing more counts. They however deposit a minimal amount of energy, so that this effect would not be visible with a realistic non-zero-threshold configuration. In practice, this is why the zero-thresholds configuration is not used. Rather, the current thresholds configuration $t_1 = 52$ DAC, $t_2 = 244$ DAC is more appropriate for this analysis. Figure 28 displays the results of the count rates computation for the current non-zero thresholds combination.

The stabilization of the count rates is more apparent than on Figure 27. The curves clearly reach a constant value after a certain value of E_{max} (around 600 MeV for Helium and 4 GeV for Carbon, Nitrogen and Oxygen) and stabilize around it for the rest of the energy range. The derivatives plots are slightly less readable because of the sporadic small increases in the curves after stabilization. Nonetheless, it is clear that the derivatives drop to 0 for most of the energy range after the inflexion point. As expected, the curves for heavier elements are above the ones for lighter elements. As mentioned in the previous analysis on the zero-thresholds configuration, this is because light particles do not deposit enough energy to register as many hits as the heavier elements. Finally, as seen in Figure 25b, the computed geometric factors are also negligible after this point, further justifying this choice of the energy range.
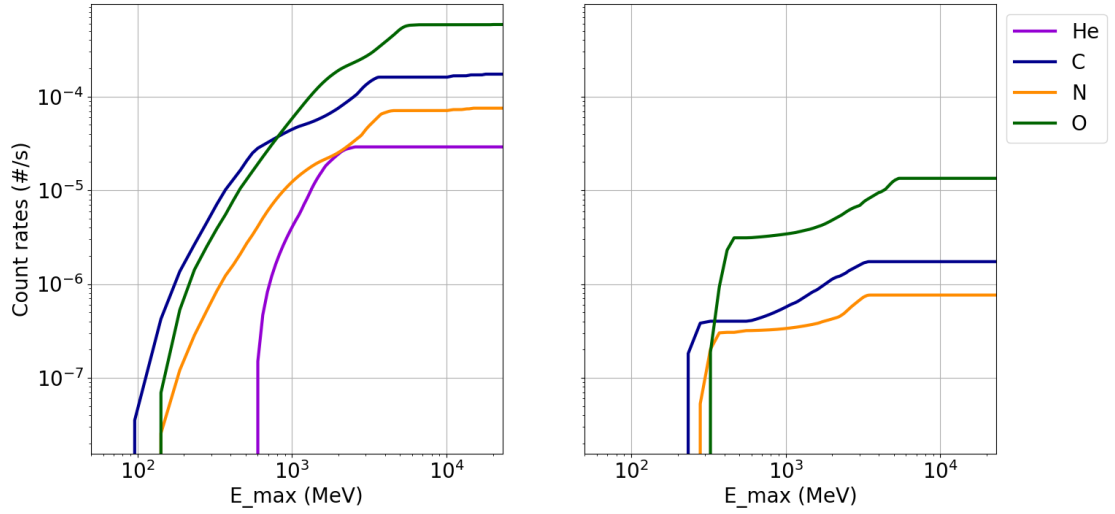
(a) Count rates.

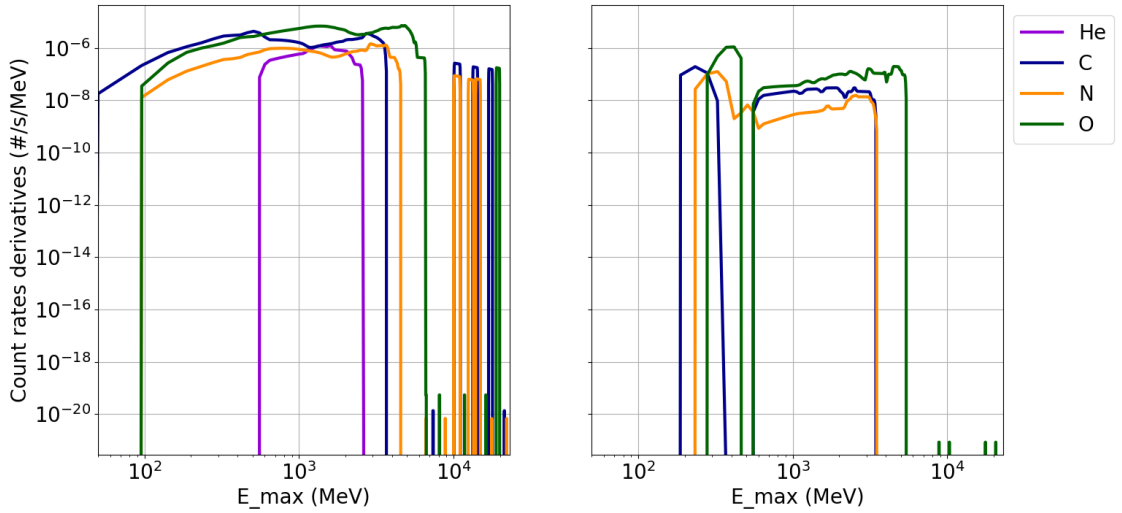*(b) Count rates derivatives.*

Figure 28: Count rates and their numerical derivatives computed from the plane simulations as a function of the maximal energy used for numerical integration in Equation (15). The subplots correspond to the HIDH diodes 1 (left) and 2 (right). Top: count rates. Bottom: count rates' numerical derivatives. Thresholds are set in the current configuration: $t_1 = 52$ DAC, $t_2 = 244$ DAC.

These considerations allow to be confident on the choice of the energy range $[0.05, 23]$ GeV for the analysis in this thesis. While a wider interval would improve the results slightly, the stabilization of the physical processes in these simulations shows that the main detector characteristics can be confidently described using these values. Practical constraints are also unavoidable and must be taken into account. A more in-depth analysis of the errors stemming from these simulations results is reported in subsection 4.5.

4.4 Long-term temporal and spatial variation of measured count rates with simulated GCRs data

The results in the previous subsections allow to characterize the detector's properties from simulation outputs. One goal of this project was to compare these findings to the first flight data coming from the JUICE spacecraft, in particular during the commissioning phase. However, at the time of writing this thesis, the available data is very limited and does not allow for accurate comparison. Nonetheless, it is possible to further extend the simulation results and investigate RADEM's properties over a long period of time by generating GCRs fluxes with PyCREME as in subsection 4.1. This subsection is dedicated to the analysis of two kinds of modulation on the GCRs intensity and their influence on the detector's count rates. The temporal modulation due to the solar cycle is first investigated, followed by the spatial modulation resulting from variations in the distance of the spacecraft to the Sun. These phenomena will also be investigated with different data coming from *Venus Express* in section 5. To mimic the more realistic configuration of the detector, the thresholds are set in the current configuration $t_1 = 52$ DAC, $t_2 = 244$ DAC.

4.4.1 Temporal modulation from the solar activity

In the previous subsections, the results were computed from a GCRs flux generated for a given date. However, as described in subsubsection 2.1.2, the solar cycle exerts a temporal modulation on the GCRs intensity via an anti-correlation relationship. As the count rates of the detector are obtained by convolving the flux with the geometric factors (Equation (14)), this modulation should also be visible in the count rates values computed over a longer period of time. To this end, the GCRs flux was simulated with PyCREME for the whole solar cycle 24 which lasted from December 2008 to December 2019. One datapoint per month was generated during these 11 years. From each of them, the count rates were computed using the same methods as in the previous subsections. The results are displayed in Figure 29. As the two diodes yield similar shifted profiles from this analysis, the count rates for each element are reported for the HIDH first diode only. To mimic the detector outputting the total count registered without discriminating between elements, the total count rates are also reported as black lines. These were obtained by summing up all results from the single elements.
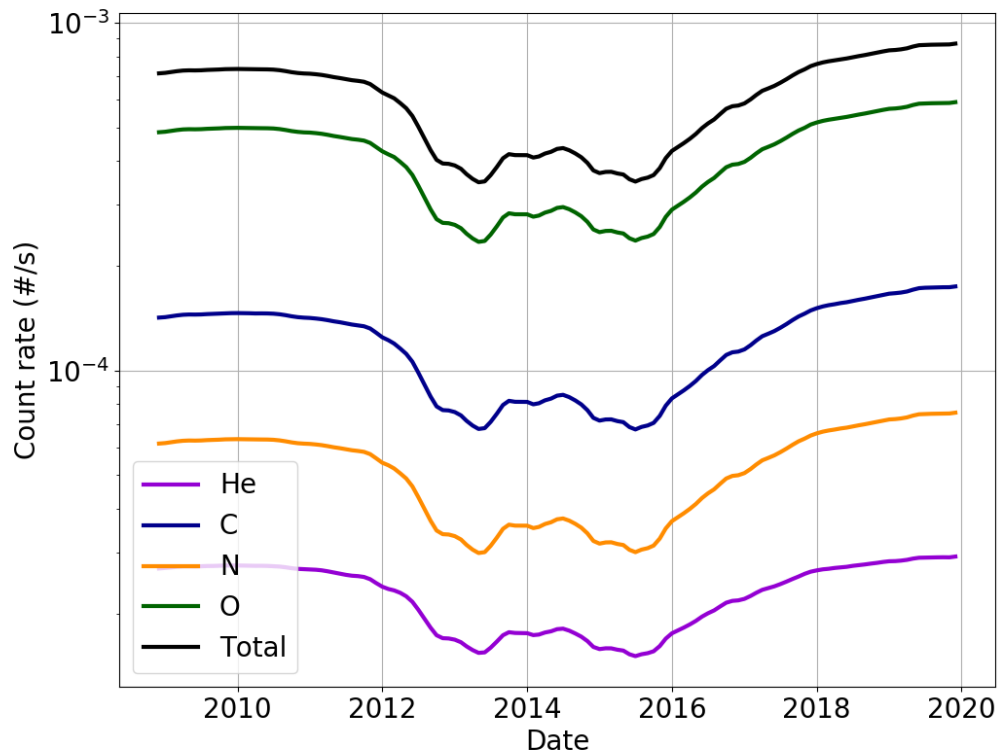
Figure 29: Count rates on the HIDH first diode computed from a PyCREME-generated GCRs flux. The 4 colored curves correspond to the count rates computed for each element and the black one is their sum. The flux was generated by PyCREME for each month between December 2008 and December 2019, which is the time period corresponding to the solar cycle 24. Thresholds are set in the current configuration $t_1 = 52$ DAC, $t_2 = 244$ DAC.

It can be seen from Figure 29 that the count rate increases with the atomic number of the elements. The curve corresponding to Helium ($z = 2$) is the lowest, followed by Carbon ($z = 6$) and Oxygen ($z = 8$). This is because a particle's deposited energy increases with its atomic number, so that heavy particles are more likely to be registered as hits on the diodes (cf Figure 22). However, it can be seen that the Nitrogen ($z = 7$) curve is below Carbon's. This comes from the difference in flux between these particles. As seen on Figure 18, Nitrogen particles are much less abundant than the others, so that less counts are registered overall. The Oxygen count rates are one order of magnitude higher than the Helium ones so that the total count rates (black curve) mostly come from Oxygen. In practice, the detector only outputs one value corresponding to the total count rates. Therefore, only the corresponding data (black curve) will be used in the following analysis. It is reported in Figure 30 together with the solar activity using the Sunspots Number (yellow curve) during this same period.
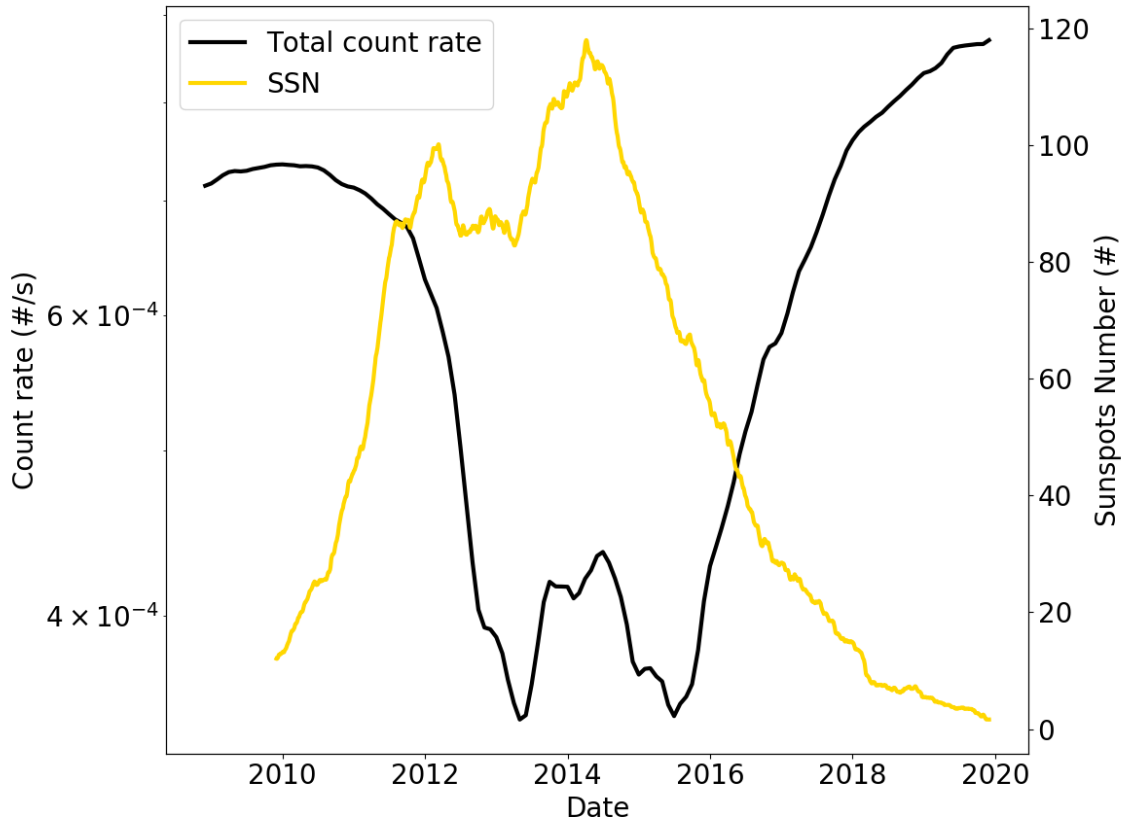
Figure 30: Total count rates on the HIDH first diode (black curve) and Sunspots number (yellow curve) during the solar cycle 24. The flux was generated by `PyCREME` for each month between December 2008 and December 2019, which is the time period corresponding to the solar cycle 24. Thresholds are set in the current configuration t_1 = 52 DAC, t_2 = 244 DAC.

The expected anti-correlation between the detector's count rates and the Sunspots Number is clearly visible on Figure 30, representative of the relationship between galactic cosmic rays and the solar activity. The minimum value of the count rates, which corresponds to the maximal solar activity, is about 60% lower than the maximum value found at minimal solar activity. This value is much larger than the one reported in subsubsection 2.1.2 for the GCRs modulation (20%). This is because the count rates do not vary in the same way as the GCRs flux. As stated before, the solar activity also modifies the particles' energy spectra, which have an additional influence on the hits registered on the diodes. In particular, there is almost no modulation on very high energies, which are also the ones corresponding to low deposited energy (because of a smaller stopping power). By cutting-off low deposited energies, the non-modulated high energy particles are the most affected. It thus seems reasonable that the variation in solar activity has a more extreme impact on the count rates and exerts a bigger modulation. Note that these results also depend on the thresholds configuration as these dictate how the diodes react to energetic charged particles. For reference, the zero-thresholds configuration yields a variation of about 35%. This corroborates the above considerations as the zero-thresholds configuration is less sensitive to changes in the particles' energy spectra.

Comparing the two curves in Figure 30, it can be seen that the anti-correlation is shifted as the count rates variation lags behind the solar activity's. The value of the lag here is about 11 months, which is close to the results reported in the literature for the GCRs time-lag at Earth ([37, 38, 3]). Cross-correlation was used to infer this value and this method will be further investigated in section 5 for the time-lag at Venus. The conclusion is that the total count rates computed with the methods described in the previous subsections and from a simulated GCRs flux over a long period of time exhibit the expected behavior for a GCRs-focused radiation monitor. Hence, the GCRs temporal variation can be inferred from the count rates measured by RADEM.

4.4.2 Spatial modulation with the heliocentric radial distance

In addition to a temporal modulation, the GCRs intensity is known to exhibit a spatial variation of about $4\%.\mathrm{A\,U}^{-1}$ with heliocentric distance [43]. Since the solar activity influences the GCRs intensity, this modulation is more important closer to the Sun than far from it. In mathematical terms, let g_1 and g_2 be the GCRs intensity in two points aligned with the Sun; and d_1 and d_2 their heliocentric distance. A simple graphical representation of this setup is displayed in Figure 31. Let $\gamma = 0.04$. Then, the spatial modulation translates in mathematical terms in the following way:

$$g_2 = g_1(1 + \gamma(d_2 - d_1)). \tag{16}$$
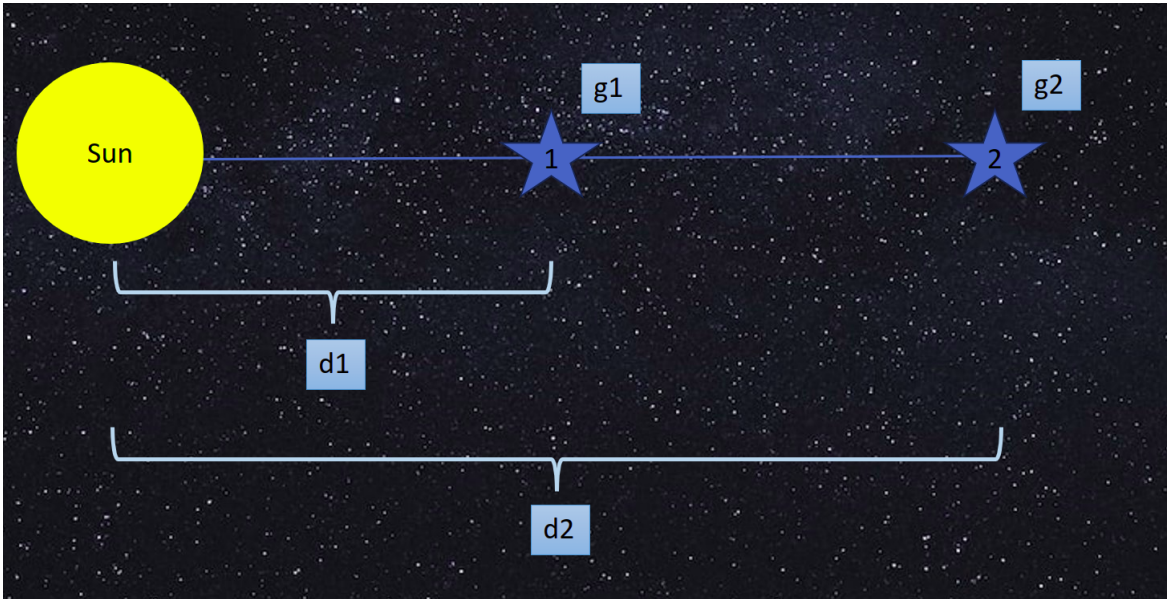
Figure 31: Graphical representation of Equation (16). The two blue stars correspond to two points in space with distances d_1 and d_2 from the Sun (yellow circle) and with GCRs intensities g_1 and g_2.

As before, this spatial modulation should be visible on the count rates output from the detector. To assess this, a GCRs flux was simulated for 4 different planets using PyCREME and Equation (16). By default, PyCREME generates the flux at Earth g_{Earth} with heliocentric distance $d_{\mathrm{Earth}} = 1\,\mathrm{A\,U}$. To generate the flux g_{planet} at another planet at the same time, this information together with the planet's heliocentric distance d_{planet} were input in Equation (16). To link the results with the next section on *Venus Express* and *Mars Express*, this was done for Venus ($d_{\mathrm{Venus}} = 0.7\,\mathrm{A\,U}$), Mars ($d_{\mathrm{Mars}} = 1.5\,\mathrm{A\,U}$) and Jupiter ($d_{\mathrm{Jupiter}} = 5.2\,\mathrm{A\,U}$).

For instance, Jupiter is 4.2 A U further from the Sun than Earth, so that Equation (16) yields a corresponding GCRs flux $g_{\text{Jupiter}} = (1 + 0.04 * 4.2)g_{\text{Earth}} = 1,168 g_{\text{Earth}}$. The flux at Jupiter is thus about 16.8% higher than at Earth. The total count rates were then simulated from these generated GCRs fluxes and the resulting curves are displayed in Figure 32. The lines are black because they correspond to the total count rates. Their linestyles represent the 4 planets: Venus (dotted), Earth (solid), Mars (dashed) and Jupiter (dashdotted).
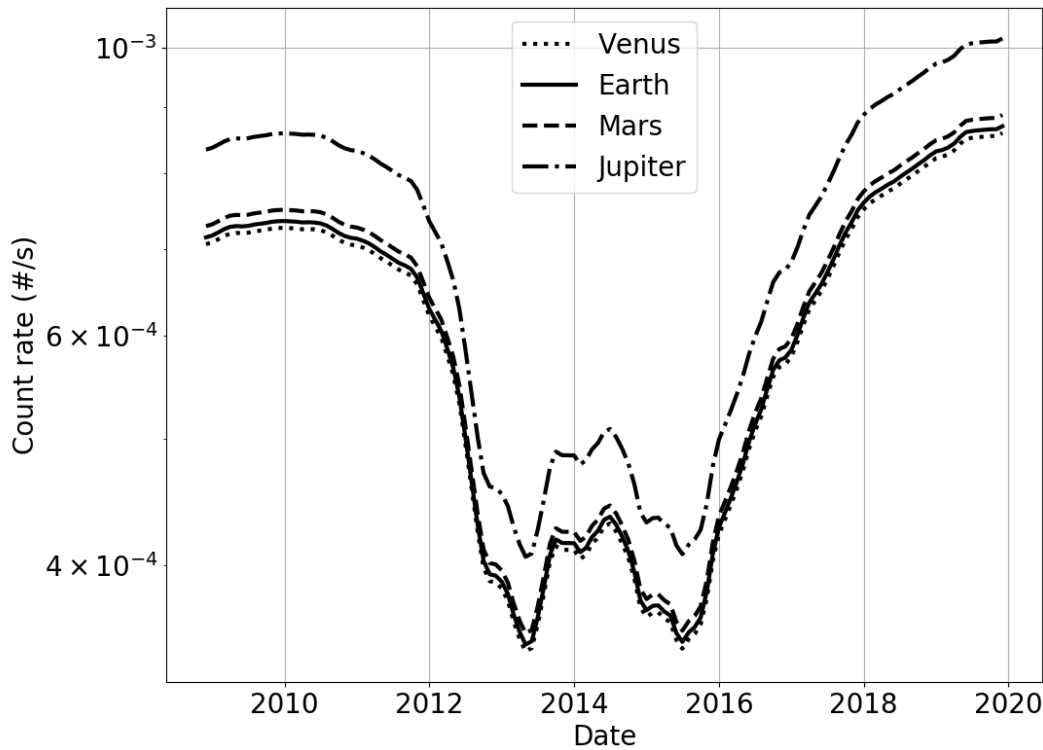
Figure 32: Total count rates on the HIDH first diode computed from a simulated GCRs flux at different heliocentric distances during the solar cycle 24. The 4 lines correspond to 4 planets of interest: Venus (0.7 A.U.), Earth (1 A.U.), Mars (1.5 A.U.) and Jupiter (5.2 A.U.). The fluxes at Earth was generated by `PyCREME`, and the flux at the other planets were recomputed from it using the theoretical heliocentric radial gradient $\gamma = 4\%/A.U.$. Thresholds are set in the current configuration $t_1 = 52$ DAC, $t_2 = 244$ DAC.

Since the count rates are inherently proportional to the flux, the resulting curves are simply ordered according to the heliocentric distances. The Venus count rates are the lowest, followed by Earth's, Mars' and finally Jupiter's. Moreover, computing the ratio between these count rates and the Earth count rates yields the factor between the GCRs fluxes. For instance, the resulting count rates at Jupiter are exactly 16.8% higher than at Earth, which is the same factor used to compute the corresponding GCRs fluxes. This analysis therefore shows how the spatial modulation of GCRs fluxes can be captured from the output of the radiation monitor. This phenomenon will be further investigated at Venus in section 5. Note that the setup displayed in Figure 31 and the considerations made here assume that the points at which the flux is measured (*i.e.* the planets) are all aligned together with the Sun. This is obviously not the case, but the latitudinal and longitudinal gradients of the GCRs fluxes are considered negligible with respect to the radial gradients [37]. The results presented here thus use a simplification of the actual planetary configuration and are expected to be valid in this context.

4.5   Error analysis

The above-described analysis is based on results from the `Geant4` Monte-Carlo simulations. As these are based on a random process, statistical errors are bound to be present and must be taken into account to assess the validity of the results' interpretation. This subsection is dedicated to this analysis.

The Monte-Carlo simulations used in this thesis output the counts, *i.e.* the number of particles registered as hits on a given diode. Properties like the geometric factor or the count rates are then inferred from these counts. If the count is denoted as N, then the 95% confidence interval for a given property P_N computed from this count is given by $P_N \pm \frac{1}{\sqrt{N}} P_N$. The count values depend on physical simulated processes like the solar modulation, but also on simulation constraints like the total number of simulated particles. In order to confidently draw conclusions from the computed results, it is therefore necessary to evaluate these confidence intervals and compare them to the properties to infer. For instance, the geometric factor curves in Figure 25 are significantly close to one another for the different particles. If the expected error from the Monte-Carlo simulation is bigger than or equal to this difference, it is not possible to confidently distinguish between these curves.

In order to assess this, the $\frac{1}{\sqrt{N}}$-errors were computed for the HIDH's diodes, where N denotes the number of registered hits used to compute the geometric factors for each energy. Results are displayed in Figure 33. The left plots are the same as in Figure 25, with one colored line per element. The only difference is that errors bars were added to represent the $\frac{1}{\sqrt{N}}$-error. This error is displayed in percentage in the right subplots as a function of the primary energy of each particle type. The top plot corresponds to the first diode and the bottom plot to the second diode. The colors follow the color scheme used in the previous figures, and the thresholds are set in the current configuration $t_1 = 52$ DAC, $t_2 = 244$ DAC.
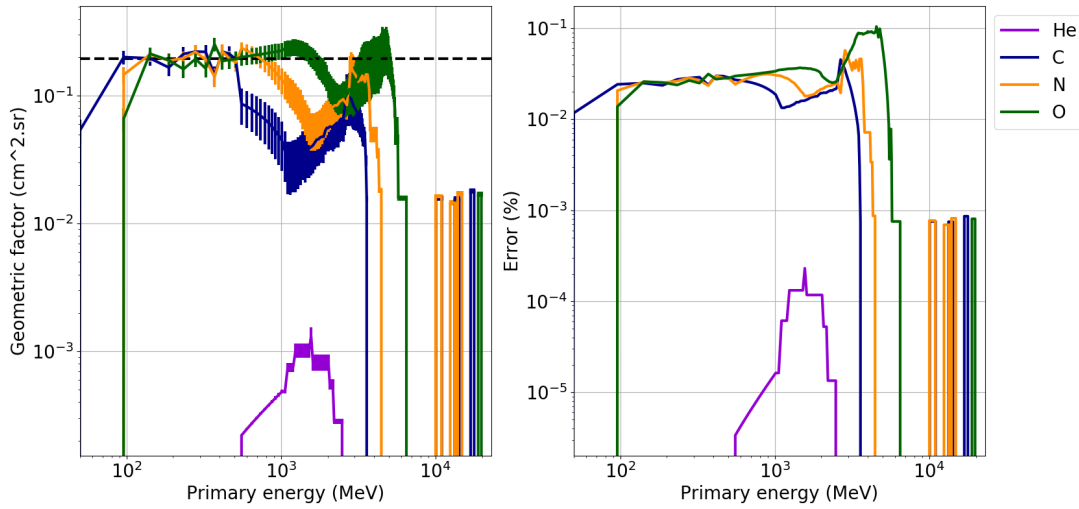
(a) Diode 1.
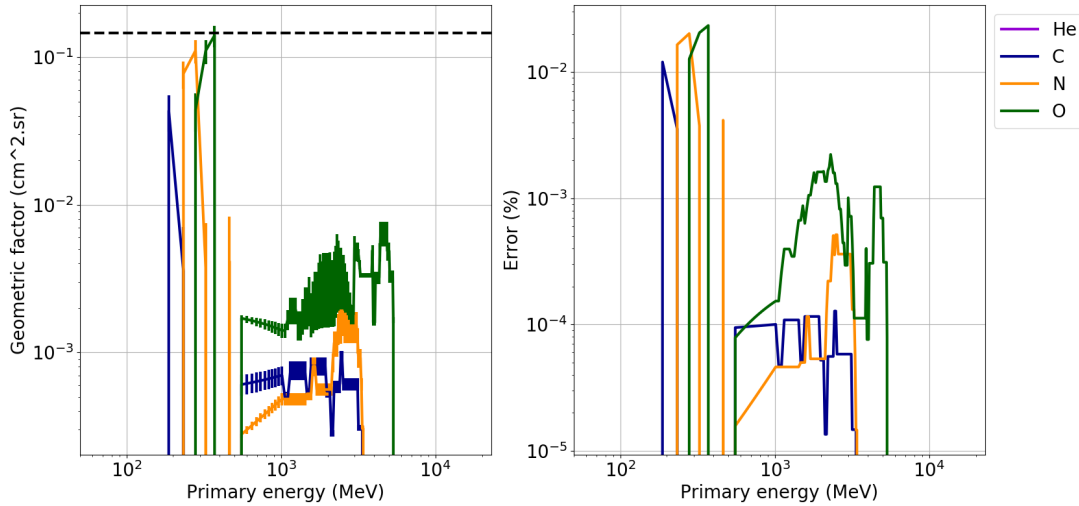
(b) Diode 2.

Figure 33: Geometric factors and corresponding errors as functions of the primary energy for both diodes. The geometric factors are computed from the simulation results. The error is computed as the $\frac{1}{\sqrt{N}}$- statistical error for the total number of hits on diodes based on the simulation results. Thresholds are set in the current configuration t_1 = 52 DAC, t_2 = 244 DAC.

In Figure 33, the error profiles are the same as the geometric factors'. Indeed, both quantities are inverse proportional to N, the number of registered hits on the diodes. This implies that higher values of the geometric factors can be studied with more confidence than lower ones. On Figure 33a's left plot, the error bars overlap quite significantly for heavy elements with primary energies between 1 GeV and 5 GeV. This makes elements in this energy range hard to differentiate. Longer simulations with more particles would increase the statistics and the accuracy of these computations. However, two diodes are available, each with their own threshold configuration. Note that these uncertainties are not present anymore for the second diode (cf Figure 33b). Here, the error is acceptable to differentiate between elements. This analysis on the geometric factor allows to assess the confidence of the simulation results.

In practice, the geometric factor is however not visible from the detector's output. Only counts are available, and they are related to the geometric factors via Equation (14). These counts can be used to assess another interesting property: the spatial modulation described in subsubsection 4.4.2. According to the results, it is in the order of 1.2% between Earth and Venus and 16.8% between Earth and Jupiter. If the statistical error computed from the counts is above these values, it is not possible to confidently deduce these properties from the simulations.

To assess this, the counts per month were computed from the count rates by multiplying them by the average number of seconds per month $M = 2\,628\,288$. From these counts, the errors have been computed using the $\frac{1}{\sqrt{N}}$ formula. Figure 34 displays the results. The black curve in the top plot is the total counts obtained by multiplying the total count rates by M. Error bars were computed using the $\frac{1}{\sqrt{N}}$ formula. The actual value of the error in % is reported in the bottom plot as a function of time, with one datapoint per month for the whole solar cycle 24. Thresholds are set in the current configuration $t_1 = 52$ DAC, $t_2 = 244$ DAC.
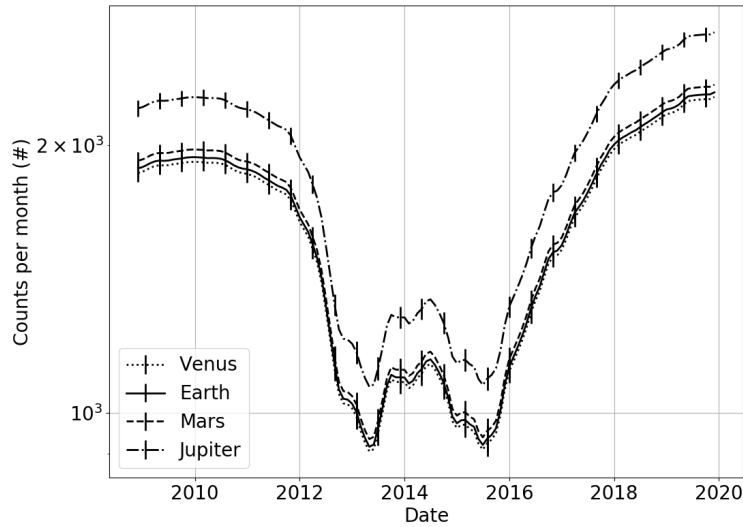
(a) Total counts per month with error bars.
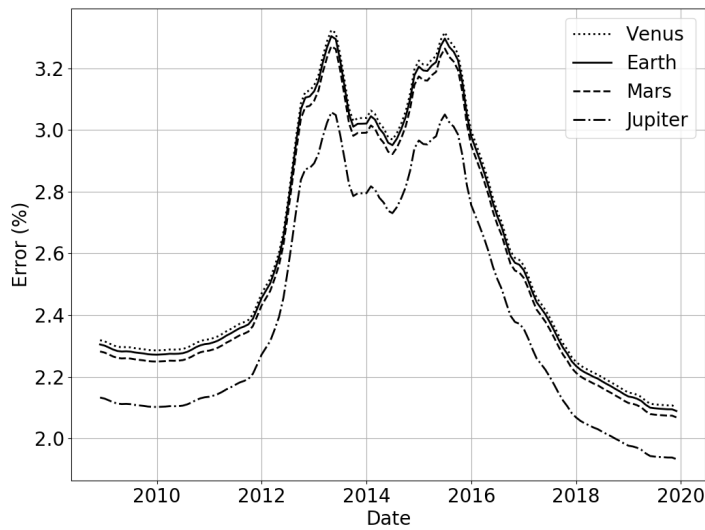
(b) Error computed as the inverse of the square root of the counts.

Figure 34: Total counts per month and statistical error expected with a Monte-Carlo simulation. Top: total counts per month computed from the count rates. Thresholds are set in the current configuration $t_1 = 52$ DAC, $t_2 = 244$ DAC. Bottom: statistical $\frac{1}{\sqrt{N}}$- error for the total counts per month based on the Monte-Carlo simulation.

From Figure 34b, it is clear that the solar modulation influences the error. Indeed, errors are maximal during the maximal solar activity in the period 2013-2016 (after lag) and minimal during the minimal solar activity (cf solar activity plot in Figure 30). This is due to the anti-correlation between count rates (or GCRs) and solar activity. As the GCRs intensity is lower during the peak of the solar activity, the corresponding counts are lower, so that $\frac{1}{\sqrt{N}}$ takes higher values and the error increases. The error takes values between 2% and 3.5%. This is bigger than the spatial modulation between Earth and Venus and Earth and Mars. Therefore, this property cannot be confidently inferred from these simulations results. This

60

is especially visible on Figure 34a as the error bars for the Venus, Earth and Mars curve clearly overlap. The main reason is the low number of simulated particles for the high energy ranges. Longer and denser simulations would significantly increase the statistics and allow for more accurate conclusions. On the other hand, the errors are below the spatial modulation between Earth and Jupiter (16.8%), so that the same analysis can be confidently conducted on this property. Finally, the temporal modulation (studied in subsubsection 4.4.1 between 20% and 60%) satisfies this condition as well and is within the confidence interval.

To conclude this subsection, the errors arising from the Monte-Carlo simulations mainly stem from the technical constraints linked to the computation times for simulations involving a high number of particles with high energies. Longer simulations would increase the accuracy of the results and allow to stay within the confidence interval for small-scale properties. An alternative would be to consider the counts over a longer period of time. For instance, using the counts per year instead of per month would reduce the errors by a factor of $\sqrt{12} \simeq 3.4$ which would make the analysis of the spatial modulation between Earth and Venus more confident.

4.6 Alternative setting: $0 \, \mathrm{DAC} \leftrightarrow 260 \, \mathrm{fC}$

The parameter values for the HIDH are reported in Table 2. These were taken from technical reports on the HIDH and used for the simulations in this thesis. In particular, the minimum charge threshold value $C_{\min}$ corresponding to $t = 0 \, \mathrm{DAC}$ is set to $C_{\min} = 0 \, \mathrm{fC}$. In other words, if the threshold is set to 0 DAC, the corresponding charge threshold is equal to 0 fC. This is what has been used in all the previous computation. However, there is an uncertainty on this value, as the information is not always consistent from one report to the other. In particular, the value $C_{\min} = 260 \, \mathrm{fC}$ was found in some of them. As the threshold values are highly relevant in this study, this point needs to be addressed. This subsection is dedicated to this analysis. Also, proper calibration to obtain the energy to charge conversion factors has yet to be done. The processing in this thesis relied instead on first principle calculations.

The impact of this change is minimal for high non-zero thresholds configuration like the current one $t_1 = 52 \, \mathrm{DAC}$, $t_2 = 244 \, \mathrm{DAC}$. Indeed, since these thresholds are already high, changing the minimum charge only slightly affects their actual values and can be straightforwardly compensated by increasing the DAC parameters. The curves profiles for these alternative configurations are thus similar to the ones already presented in the previous subsections. However, this impact gets more important for lower values of the DAC thresholds, especially the zero-thresholds configuration $t_1 = 0 \, \mathrm{DAC}$, $t_2 = 0 \, \mathrm{DAC}$. These no longer correspond to $C_1 = C_2 = 0 \, \mathrm{fC}$ but to a non-zero configuration $C_1 = C_2 = 260 \, \mathrm{fC}$. Thus, this subsection focuses on this case. In particular, the influence of this change on the deposited energy, the geometric factors and the count rates is investigated. In the following, the *0-threshold formalism* denotes the convention $0 \, \mathrm{DAC} \leftrightarrow 0 \, \mathrm{fC}$ used in the previous subsections, and the *260-threshold formalism* denotes the alternative convention $0 \, \mathrm{DAC} \leftrightarrow 260 \, \mathrm{fC}$. In both cases, no DAC threshold is set on the diodes, *i.e.* $t_1 = 0 \, \mathrm{DAC}$, $t_2 = 0 \, \mathrm{DAC}$.

The first straightforward impact of the thresholds on the simulation results is found on the deposited energy. The usual two phenomena are taking place. On the one hand, lighter elements interact less with the medium and deposit less energy. Thus, the impact of the threshold on them is more important than on heavier elements. On the other hand, the

stopping power decreases with the primary energy. Thus, after some energy value, the curve of the mean deposited energy is expected to drop faster than before for high energies. As light elements deposit less energy, this should be more visible for them. Recall that because lighter elements interact less with the material, they are also more likely to penetrate the collimator and still interact with the diodes. However, if the threshold is non-zero, this effect is expected to be minimized because these particles do not deposit much energy on the diodes. To study these effects, the results of the deposited energy computation are displayed in Figure 35. The subplots represent the 0-threshold formalism (Top) and the 260-threshold formalism (Bottom). The curves and axes are the same as in Figure 22.
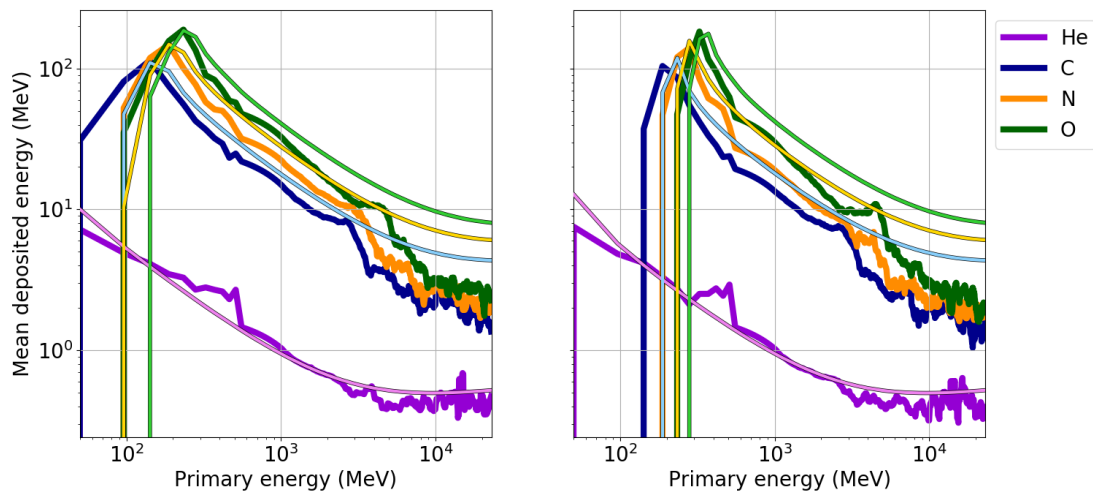
(a) 0-threshold formalism: $C_{\min} = 0$ fC.
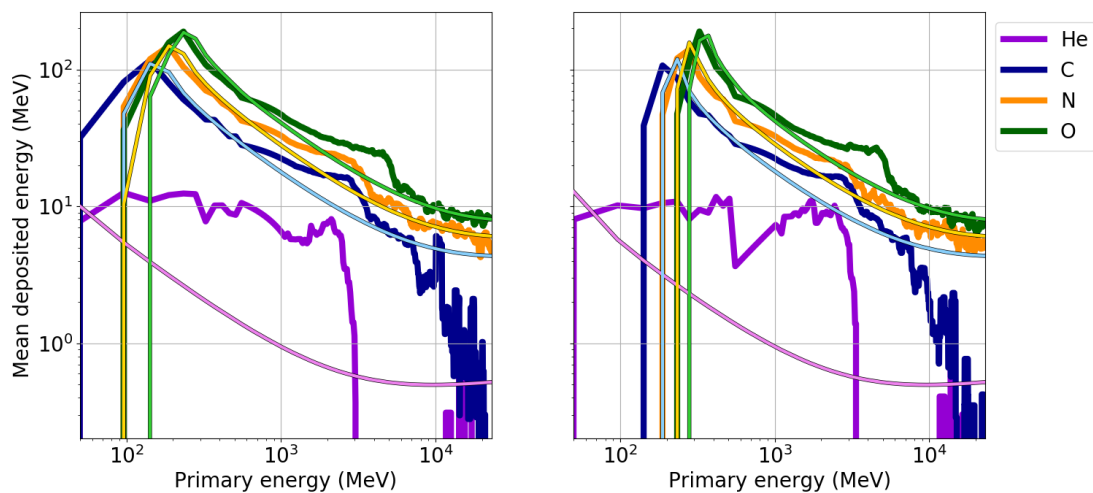
(b) 260-threshold formalism: $C_{\min} = 260$ fC.

Figure 35: Particle-detector interaction simulation with `Geant4` *(simple solid lines) and* `FOCom-PDI` *(lighter lines with black outlines) for the two thresholds formalism. Plots are as in Figure 22. No lower threshold is set on the diodes.*

The above considerations can be validated from Figure 35. The curves for lighter elements like Helium indeed drop much faster than before. This is visible from the Carbon curve as well. Note also that the values for Helium are higher. They seem to stabilize at a constant value around 10 MeV. This is thought to be due once again to the limited interaction between Helium particles and matter. With the 0-threshold formalism, they were able to deposit even negligible amounts of energy on the diode and still register as a hit, which would bring the mean deposited energy down (cf Figure 36a). With the 260-threshold formalism *i.e.* a non-zero threshold, only Helium particles coming through the aperture can register as hits on the diodes. This brings the mean deposited energy up to a constant value because the stopping power compensates the increase in primary energy as well.

The second impact of this change of formalism can be studied in terms of the geometric factor. As it is directly related to the number of registered hits on the diodes, the effect is straightforward from the previous analysis. The geometric factors corresponding to lighter elements are expected to drop for high energies and the stable values for heavier elements should be lower than before, as less hits are registered. The results are displayed in Figure 36 and corroborate these considerations. The curves' colors follow the same element convention as in the previous subsections, and the black dashed lines represent the theoretical values.

Once again, the values for Helium are the most impacted by this change. The geometric factors are overall lower, as less hits are registered to contribute to Equation (13). The curve drops to 0 around 2000 MeV, as the stopping power for this energy is too low for the particles to deposit enough energy on the diode to trigger a reading. A similar phenomenon is visible on the Carbon curve. Comparing the top and bottom plots, it can be seen that the stabilized values for Oxygen and Nitrogen are also lower than before.
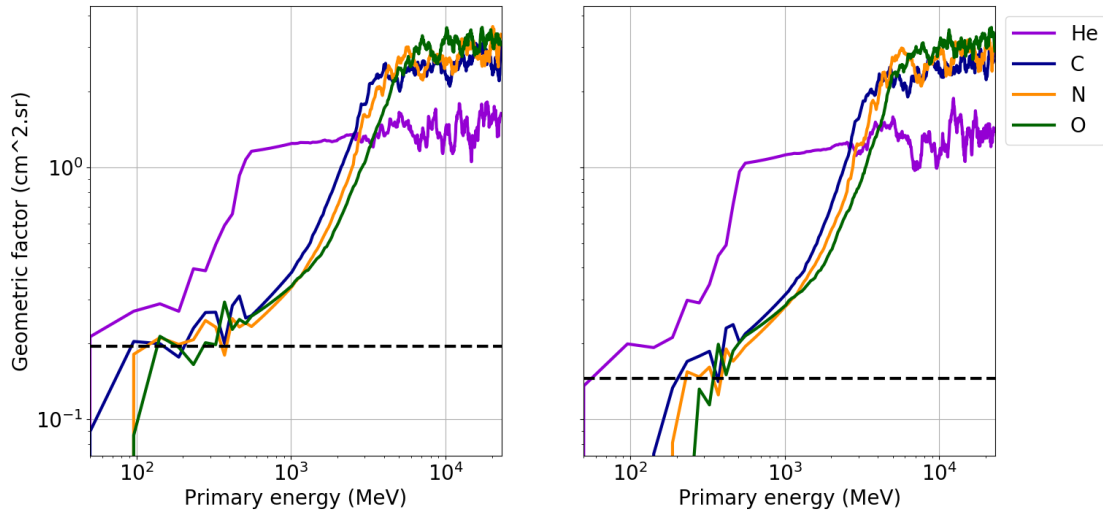
(a) 0-threshold formalism: $C_{\min} = 0$ fC.
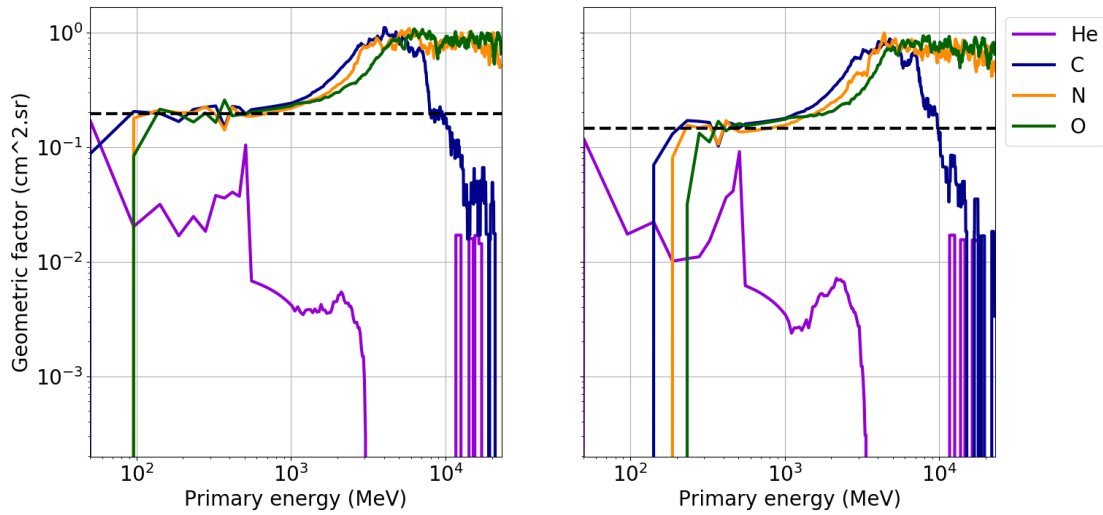
(b) 260-threshold formalism: $C_{\min} = 260$ fC.

Figure 36: Geometric factors computed from the plane simulations with Equation (13) for the two thresholds formalism. Plots are as in Figure 25a. No lower threshold is set on the diodes.

Finally, similar considerations can be made regarding the count rates. The effect of increasing the thresholds has already been investigated in Figure 26 and is a direct consequence of the changes in the geometric factors. As less hits are registered, the resulting count rates are lower. Regarding the count rates as functions of the maximum energy used in the integration as in subsubsection 4.3.6, the results lie between Figure 27 and Figure 28. They correspond to a simple downshift of the curves and a displacement of the Helium curves below the others.

4.7 Conclusion

This section was dedicated to the numerical simulations conducted on the JUICE radiation monitor to characterize its response to GCRs particle fluxes. The main goal was to simulate the interactions of the most abundant elements in galactic cosmic rays with the *Heavy-Ion Detector Head*, compute some of the detector properties and estimate its response during the mission cruise to Jupiter. The influence of the lower thresholds was investigated as well. These results are now available for reference to the scientific teams who will be working on future JUICE data.

First of all, the GCRs particle flux was simulated using `PyCREME` to understand the most abundant elements in GCRs fluxes and their energy range. Helium ($z = 2$), Carbon ($z = 6$), Nitrogen ($z = 7$) and Oxygen ($z = 8$) were the main contributing elements, with energy in $[10^1, 10^3]$ MeV/AMU. Using these results, simulations were run for a simple point source with a first order framework (`FOCom-PDI`) and a dedicated particle-through-matter simulation software (`Geant4`). These allowed to gain a first insight on the deposited energy profiles and the underlying processes behind particles-detector interactions. The first order framework resulted very satisfying for this simple setup, but its limits were revealed when more complex settings were used. A more realistic plane source was afterwards used with `Geant4` to capture some of the detector's properties. Its field of view and geometric factors were computed from the simulation results and compared to the theoretical values. In general, these match pretty well. However, the results depend on several factors, the two main ones being the thresholds configuration and the energy of the particles. It was shown in several instances that particles with higher energies can penetrate the collimator and interact with the diodes, directly impacting the field of view and geometric factor computations. The effects of these high energy particles can be mitigated using different thresholds configurations on the HIDH, as these particles tend to deposit less energy on the diodes. The current thresholds configuration $t_1 = 52$ DAC, $t_2 = 244$ DAC seems to be rather effective in this regard as it allows to narrow down the primary energy range of the particles to consider, as well as to force most of them to go through the aperture. Finally, the channels' count rates were computed by convolving the geometric factors with the particles fluxes. The influence of the lower thresholds on these was studied and matched the expected behaviours.

One of the original goals of this project was to compare these simulation results to data coming from the JUICE spacecraft after its launch in April 2023. As the available data at the time of writing this thesis is limited, `PyCREME` was reused to generate long term GCRs fluxes and assess the influence of the GCRs temporal and spatial modulation on the count rates. The temporal modulation was investigated by generating a GCRs flux over the 11 years of the solar cycle 24. It appears that this temporal variation has a greater impact on the count rates than on the GCRs flux (30% to 60% difference between the minimum and maximum values of the count rates against 20% for the GCRs fluxes). This was explained by the fact that the count rates not only depend on the flux, but also on the energy spectra of the particles and the response of the detector to these. The spatial modulation was studied in a purely ideal way by manually generating a GCRs flux at Venus, Mars and Jupiter based on the theoretical value of the radial gradient $\gamma = 4\%\,\mathrm{A\,U}^{-1}$. Because of this ideal scenario, the spatial modulation was straightforwardly derived from the count rates profiles and matched the theoretical gradient values.

The above considerations should also take into account several uncertainties stemming from the simulations. First of all, the energy range $[0.05, 23]$ GeV used in the simulations reduces the accuracy of the results, as high energy particles are known to have a significant impact on the detector's readings. However, this choice was justified by conducting a quantitative analysis on the stabilization of the computed properties. The conclusion was that this range was sufficient to get a very good estimate on these. Moreover, the thresholds configuration was again proved to have a significant impact on this uncertainty, as the current thresholds configuration yields a very satisfying stabilization. The number of particles used in the simulations is a source of error as well, since too few particles in the random Monte-Carlo process would not allow to draw confident conclusions from the reported findings. This was assessed and shown to be acceptable for the cases of interest. Some ways of increasing the statistics include combining the two diodes and computing the counts over a longer period of time. A more straightforward fix would be to increase the number of particles used in the simulations. However, this is associated to longer computation times which were not achievable in the timeframe of this thesis. Nevertheless, it is believed that the results presented here are enough for the objectives of this project. Finally, uncertainties on the actual configuration of the HIDH were addressed using an alternative thresholds setting. The influence of this change was estimated to be minimal for high thresholds configuration but significant for low ones, especially the zero-thresholds configuration.

To conclude this section, the main goal of this project was attained. The simulations run allowed to understand the main components of GCRs, their energy range and their interactions with RADEM. The first order framework yielded very satisfying and fast results, allowing to get a good initial guess on these interactions. The more complex simulations with `Geant4` allowed to characterize the detector's field of view and compute its geometric factors and count rates. The influence of the Sun's temporal and spatial modulation on GCRs intensity was then investigated by generating a wider range of GCRs fluxes. Uncertainties and errors coming from the limited nature of the simulations were studied and found to be acceptable within the requirements of this thesis. Nonetheless, it would be interesting to run longer and denser simulations in order to improve on these results. These findings should also be compared against real JUICE data when available, especially in 2032 when it has reached the Jovian system.

5 Using EDAC counters for GCRs characterization with *Venus Express* data

As previously introduced, the EDAC counter, as engineering data, is in principle not used for scientific purposes. However, the relationship between the EDAC counter and GCRs fluxes has been established for a long time and was exploited in [37], where the relationship between the solar cycle modulation on GCRs and the EDAC counter was investigated. In [37], a procedure was developed using data acquired from *Mars Express* (MEX) and *Rosetta* (ROS) and could be applied to other spacecrafts.

This section investigates this procedure more in details and showcases how it was applied to the *Venus Express* (VEX) data and compared to the MEX and ROS data studied in [37]. Two main points were investigated, as in subsection 4.4. First, the relationship between the EDAC slope and the solar activity was studied in order to link it to the temporal modulation of GCRs fluxes. The results of this analysis indicate that the influence of the solar modulation is near-instantaneous at Venus. Then, focus was set on the spatial modulation of the GCRs intensity with heliocentric distance. To this end, [37] used the ratio between the EDACs to disentangle these two modulations and focus on the spatial one. This is further investigated here. Note that these findings are currently being compiled in a paper for publication in *Planetary and Space Science* and that this section is based on this paper.

5.1 Data processing

This section describes the data processing procedure developed in [37]. It was applied to data coming from MEX, VEX and ROS in order to reproduce the results in the previous study and analyse the new data coming from *Venus Express*. The comparison between these various missions is made more interesting by their different orbit profiles, as displayed in Figure 37. *Rosetta* presents a wider trajectory, reaching far from our host star, while *Venus Express* and *Mars Express* orbit their respective planets in a stable elliptic motion around the Sun. This figure also reports the Mars flyby of *Rosetta* on February 24th 2007, which will be referred to later in this work.

First, starting from the raw EDAC data, the zero-resets performed during the mission were corrected to keep a monotonically increasing counter. This step is straightforward, as the counter simply needs to be turned back to its previous value when reset to zero. Then, the SEP events corresponding to sudden big increases in the EDAC counter [53] were removed. As illustrated in Figure 38a, they were detected by computing the discrete derivative via finite backward difference. Once these rates were computed, their distribution (Figure 38b) was studied. The jumps with values above the 99th percentile, which resulted to be 2.5 day^{-1}, were then considered to be due to SEP events and removed from the EDAC curve. Table 5 lists some of these major events for each mission and whether they have been documented in the literature. The main reference source is the *SpaceWeatherLive* [48] website, which regroups information about all past and present solar activity. Some reference papers are also listed in the table. It can be seen that out of the 19 principal detected and removed solar events, 13 are documented. In particular the very important solar flare events of December 2006 and March 2012 were well detected. The other corrections may be artifacts of the detection procedure, or actual low intensity events, not documented to this day. Finally, the data was smoothed by applying a Savitzky-Golay [55] filter with a 365-days window.
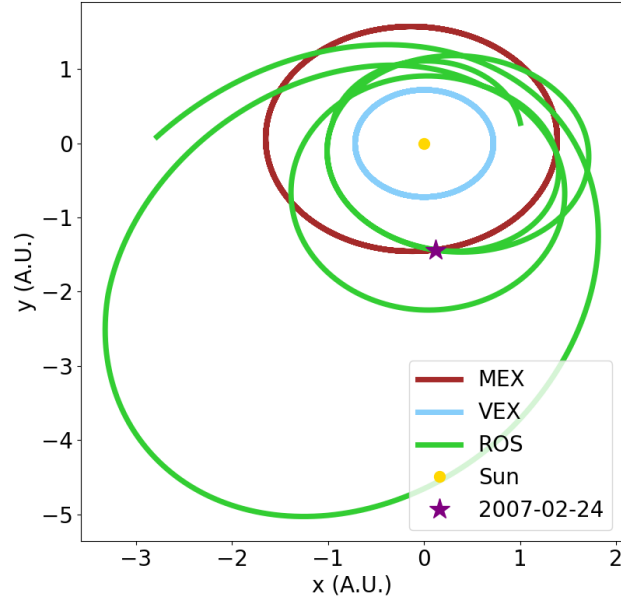
Figure 37: MEX, VEX and ROS orbits in the equatorial plane around the Sun. The purple star-shaped marker indicates the Rosetta Mars flyby in February 2007.

Table 5: Removed SEP events during the data processing phase.

Date	Mission	Space weather known event
2004-04	*Rosetta*	No
2004-06	*Rosetta*	No
2004-07	*Rosetta*	Yes, X1.8
2005-01	*Rosetta*	Yes, X7.1 [28]
2005-03	*Rosetta*	No
2005-09	*Rosetta*	Yes, X17+ [20]
2006-01	*Mars Express*	Yes, C4.1
2006-05	*Mars Express*	No
2006-09	*Venus Express*	No
2006-10	*Venus Express*	No
2006-12	*Venus Express*	Yes, X9.0 [29]
2008-01	*Venus Express*	Yes, C1.4
2009-09	*Rosetta*	Yes, C2
2011-06	*Rosetta, Venus Express*	Yes, M2.5 [39]
2012-03	*Mars Express, Venus Express*	Yes, X5.4 [49]
2014-01	*Rosetta*	Yes, X1.2 [41]
2014-09	*Venus Express*	Yes, X1.6
2017-09	*Mars Express*	Yes, X9.3 [65]
2018-04	*Mars Express*	Yes, B9

Note that the original approach in [37] places the smoothing after the computation of the slope, rather than on the processed counter as done here. This minor update was chosen as it produces constant boundary artifacts which are very easily removable in a systematic manner (smoothing the slope instead generates linear artifacts). Note that the resulting data is the same in both cases.

This yields the processed EDAC counter, from which the slope can be compared with the solar cycle. Additional steps must be taken in order to uniformize the datasets coming from the three missions. As listed in Table 6, the operating periods of the three missions are not identical. Moreover, *Rosetta* was in hibernation between June 2011 and January 2014. Finally, some data points were missing, *i.e.* some dates did not have value for certain missions. Those were completed by the data in the previous available date. Combining this with the above-described data processing scheme yields the final procedure.

Table 6: Time periods for the three considered missions.

Mission	Start date	End date
Mars Express	January 2005	January 2018
Rosetta	March 2004	September 2016
Venus Express	November 2005	November 2014

Figure 38 showcases the result of the data processing on the VEX EDAC. Panel (a) displays the raw data compensated for the zero-resets, together with the numerical derivative computed to detect the SEP events. The distribution of the numerical derivative is displayed in panel (b). Panel (c) reports the final smoothed counter where the SEP events have been removed and panel (d) displays the computed slope where constant boundary artifacts were removed. Note that the date ranges between panels (a) and (c) are slightly different since missing datapoints have been inserted.
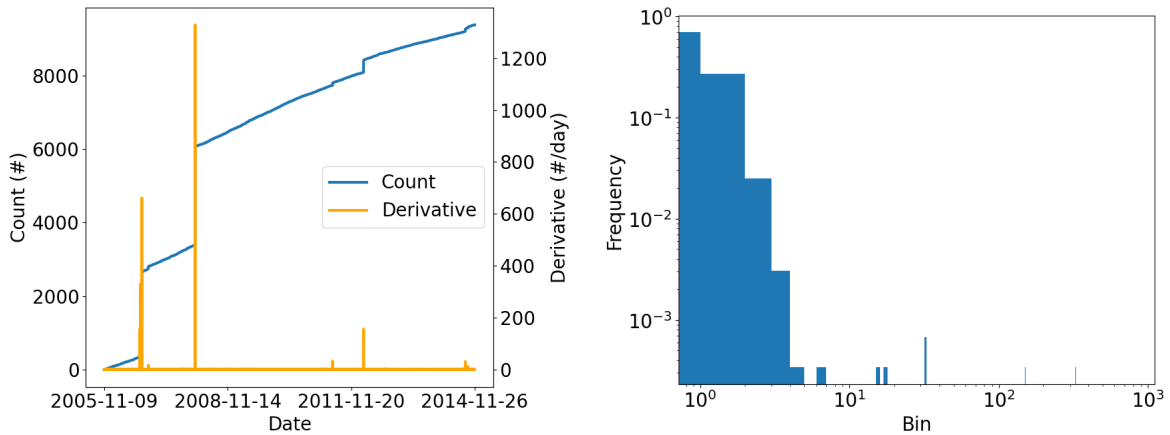
(a) Raw counter and numerical derivative.

(b) Distribution of the numerical derivative.
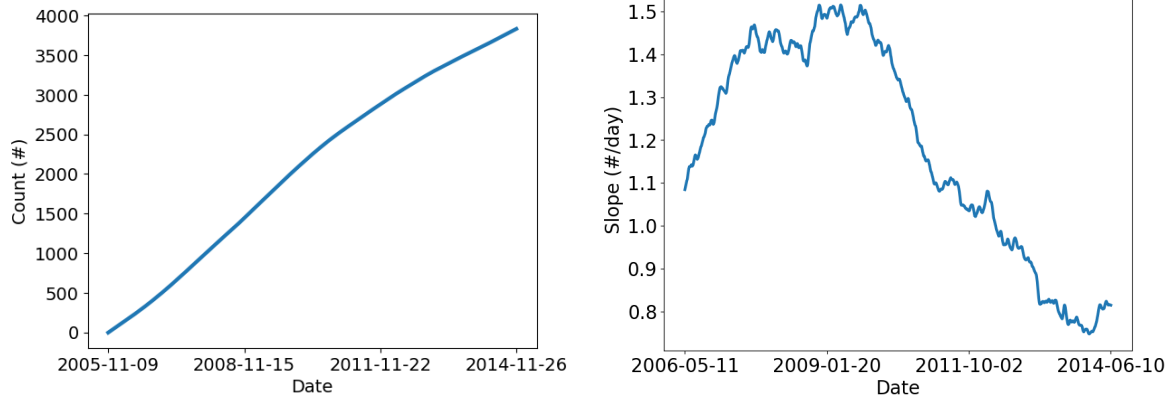
(c) Processed smoothed counter.

(d) Computed slope.

Figure 38: Data processing on the VEX EDAC counter. Panel (a): Raw counter where the zero-resets have been removed (blue curve) and its numerical derivative (orange curve). The big spikes represent SEP events which will be subsequently removed. Panel (b): Distribution of the numerical derivative of the VEX EDAC counter. The axes are in log-scale to represent the wide range of values. The highest values correspond to SEP events to be removed. Panel (c): Processed counter, in which the SEP events previously detected have been removed and a smoothing has been applied. Panel (d): EDAC slope, computed as the numerical derivative.

5.2 GCRs characterization with EDAC slope

The slope of the EDAC counter is computed with a backward finite-difference scheme using a 2-weeks (14 days) window. Figure 39a displays the EDAC slope computation against the Sunspots number for MEX, VEX and ROS. *Rosetta*'s hibernation between 2011 and 2014 is visible, as the green curve stops due to absence of data. The expected anti-correlation shape is visible, as seen in Figure 39b.

Figure 39c displays the cross-correlation between the VEX EDAC slope and the Sunspots number representing the solar cycle. The minimum of the curve (red line) corresponds to the maximum anti-correlation. As explained in [37], this gives an estimate of the time-lag between galactic cosmic rays and solar cycle. As mentioned in subsubsection 2.1.2, values for this time-lag at Earth vary from one source to another. Here, the computed time-lag is negligible, with a value of -0.033 months, or 1 day. This could indicate that the influence of the Sun on the GCRs fluxes is near-instantaneous at Venus.
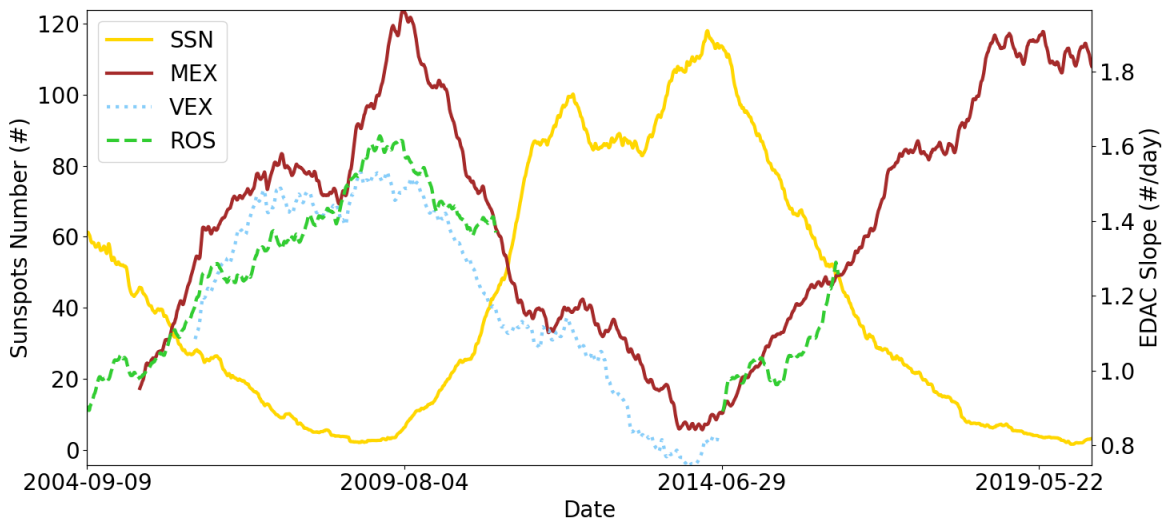
(a) EDAC slope for the three missions (Mars Express, Rosetta, Venus Express) and Sunspots number.
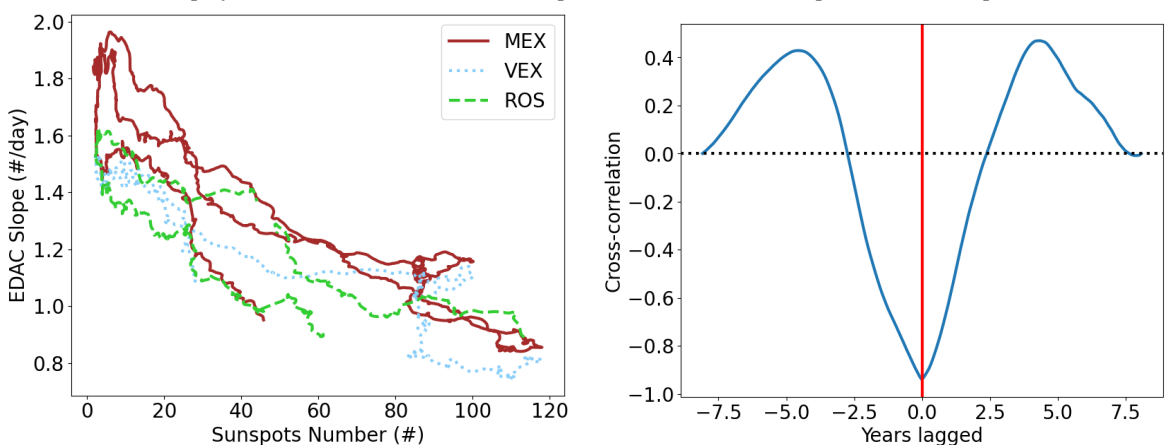
(b) Anti-correlation between the EDAC slopes and the Sunspots number.

(c) Cross-correlation between the VEX EDAC and the Sunspots number.

Figure 39: Relationship between EDAC slopes and solar cycle. Panel (a): EDAC slopes for MEX, VEX and ROS (right y-axis) with the Sunspots number (left y-axis) as a function of time. Panel (b): the same quantities plotted against each other to emphasize their anti-correlation. Panel (c): time-lag between the GCRs intensity at Venus and the Sunspots number computed by cross-correlation.

71

5.3 Comparison between the missions and link to the heliocentric distance

As described in subsubsection 4.4.2, the GCRs intensity is known to exhibit a variation of about $4\%.\mathrm{A\,U}^{-1}$ with heliocentric distance [43]. Recall that the GCRs fluxes g_1 and g_2 for two points with heliocentric distances d_1 and d_2 are related via:

$$g_2 = g_1(1 + \gamma(d_2 - d_1)). \tag{17}$$

With numbers, assume that the spacecraft is initially situated in point 1, at a distance $d_1 = 1\mathrm{A\,U}$ from the Sun, and moves radially outwards to get to point 2, at a distance $d_2 = 2\mathrm{A\,U}$, so that it moves exactly $1\mathrm{A\,U}$ away from the Sun. Then $g_2 = g_1(1 + \gamma) = 1.04g_1$. In other words, the GCRs intensity 1 A U further away from the Sun is $\gamma = 4\%$ more than initially.

As previously shown, the EDAC slopes are a good representation of the GCRs intensity. It is therefore natural to expect a similar variation in the EDAC slopes: about $4\%.\mathrm{A\,U}^{-1}$. However, as the spacecraft is moving both through space and time, the GCRs intensity (or equivalently the EDAC slope) is affected both by the spatial modulation and the temporal modulation. In order to isolate the former from the later, it is necessary to consider the counter at different locations in space but at the same time. In this regard, [37] uses a procedure described in [63, 64], where the ratios of two corresponding detectors are taken. Assuming that the effect of solar modulation is the same on two spacecrafts, taking the ratio between the two counters will cancel this effect and leave only the effect of heliocentric distance.

To this end, the ratios between EDAC slopes for the three pairs of missions have been computed for their longest common period. Plotting them as a function of the difference in heliocentric distance and fitting the resulting curve to a straight line should then yield a slope of about $4\%.\mathrm{A\,U}^{-1}$. In Figure 40, the blue curves are the ratios plotted against the difference in heliocentric distance and the orange lines are the fitted linear curves.
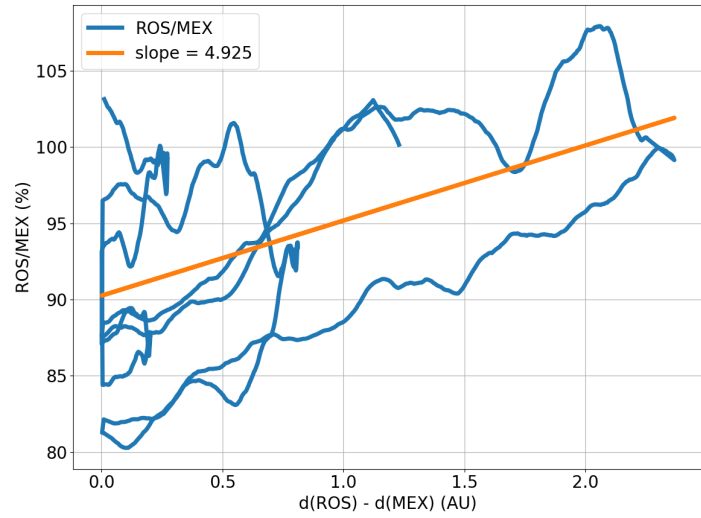
(a) ROS/MEX
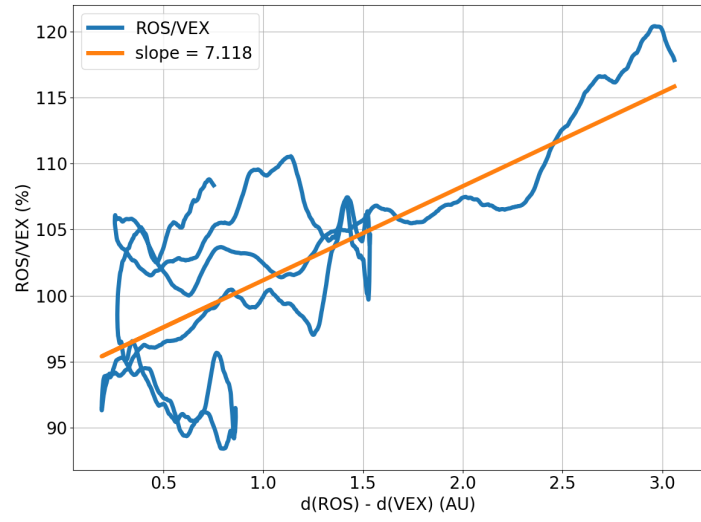
(b) ROS/VEX
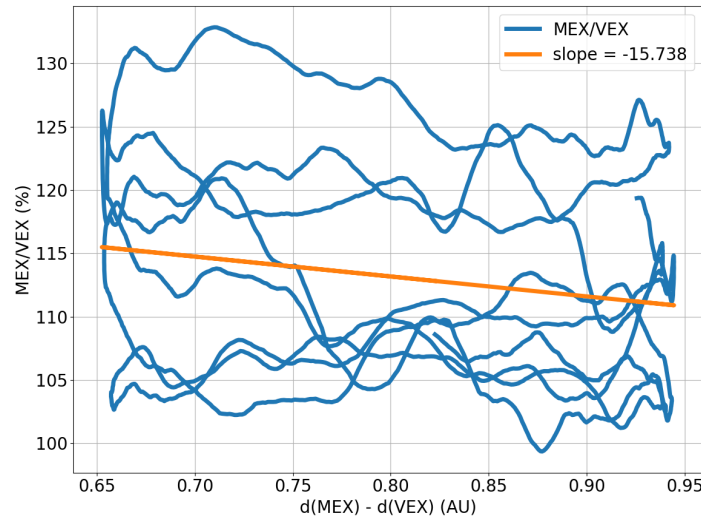
(c) MEX/VEX

Figure 40: Ratio of the EDAC slope as a function of the difference in heliocentric distance. The orange lines are the corresponding fitted linear curves. The ratios are computed for the maximum common time periods between missions.

The slope increase values computed for the different ratios are:

- 4.9%.A U^{-1} for ROS/MEX;

- 7.1%.A U^{-1} for ROS/VEX;

- −15.7%.A U^{-1} for MEX/VEX.

On the one hand, the value of 4.9%.A U^{-1} for ROS/MEX is similar to the one found in [37], indicating that the reproduced procedure is correct. On the other hand, the results involving VEX are not so satisfying. The value for ROS/VEX is too high. One possibility is that this linear 4%.A U^{-1} law might not hold when getting closer to the Sun, which is the case for VEX as Venus is close to the center of our Solar System. The negative value for MEX/VEX is unexplained at the moment. One feature to notice is that the x-axis range is much smaller in this case, spanning only 0.3A U against the 3A U when involving *Rosetta*. It might be that the variation in this range is different than with bigger ones and yields different results. This is especially visible on Figure 40c, as the ratio exhibits a large variation without any defined trend. The beginnings of the two other plots exhibit a similar range of variation in the interval [0, 0.7] A U. At the time of writing this thesis, significant conclusions cannot be drawn from these results.

5.4 Discussion

The procedure described in [37] was expanded on with data from VEX. The results show that the EDAC slope exhibits a very clear anti-correlation with the Sunspots Number (with a correlation coefficient of −0.95 at minimum lag). The VEX curve clearly follows the ones of MEX and ROS previously derived, confirming that the solar modulation exhibits a similar pattern at Venus. It is mainly always below the other two curves, which matches the assumption that the GCRs fluxes at Venus are expected to be lower than at Mars and *Rosetta*'s comet since Venus is closer to the Sun. However, a small portion between 2006 and 2008 does not match this observation. This can be due to possible differences in spacecraft shielding and memory sensitivity which can have an influence on the EDAC response. The GCRs behaviour in the proximity of the Sun is also less known, so that local uncertainties are expected. Nevertheless, the curve profiles match the theoretical anti-correlation relationship between GCRs fluxes and solar activity and correspond to the curves in Figure 30.

Cross-correlating the EDAC slope with the Sunspots Number results in an almost zero time-lag, which could indicate that the solar activity has a near instantaneous influence on the GCRs fluxes at the orbit of Venus. This clearly differs from the reported value at Earth which, depending on the study, is estimated to be between 2 and 8 months. Comparing the available data shows that VEX records less SEP events than MEX at the same period, indicating that the VEX EDAC is sensitive only to particles in the most energetic part of the GCRs spectrum. This could have an impact on the response of the VEX EDAC to solar modulation and bias the computed lag. These findings need to be further checked with theoretical considerations and models since the distance between the Earth and Venus is relatively small (0.3 A U).

The GCRs intensity variation was investigated in [31] using background counts of onboard microchannel plates. The procedure developed here is similar in idea and results, as both approaches used the constant flux of highly energetic particles on spacecraft devices to infer GCRs variation. The anti-correlation with the solar cycle was found in both cases as well. These studies complement each other since the procedure in [31] did not yield significant results regarding the time lag at Venus.

Planetary shielding is known to affect the GCRs intensity measured on a spacecraft, as the flux is intercepted on the solid angle of the planet. This prevents it from reaching the spacecraft and effectively reduces the flux. However, *Venus Express* followed a highly elliptical orbit and was most of the time at a distance greater than 8000 km from Venus. As described in [37], this is above the recommended value in [40], making this effect negligible for this work.

Regarding the ratios, the results found with the VEX data lead to believe that the underlying systems are more complex than previously hypothesized. The high variations in the ratio values do not allow to draw confident conclusions and the fitted slope values do not match the theoretical $4\%.\mathrm{A\,U}^{-1}$. The previously mentioned drop in the MEX data might have some influence here. Another interesting feature to investigate is the relative position of the spacecrafts with respect to the Sun. Indeed, while the GCRs radial dependence on the heliocentric distance has been characterized, this is not the case for the longitudinal variation, as an isotropic constant flux is assumed. In addition, different zones around the Sun could have some impact there. However, it is more likely that taking the ratios between EDAC slopes is actually not correct. As mentioned, this procedure comes from [63], in which the ratios of corresponding particle detectors on the *Pioneer 10* and *Pioneer 11* spacecrafts are taken to remove the effect of solar modulation. In this case, the instruments are rigorously identical, hence the solar modulation indeed has the exact same effect on them. In the case of MEX, VEX and ROS, the exact configurations are not documented and might differ. This would lead to significant differences in the effect of particles on the EDAC due to their varying energy ranges. In subsubsection 4.4.2, the spatial modulation was studied using ideal generated GCRs data from `PyCREME`. Having access to simultaneous data from two strictly identical spacecrafts would contribute to the use of EDAC data for similar studies.

Rosetta performed a flyby at Mars on February 24th 2007 (cf Figure 37). This could be used to calibrate the ROS EDAC slope to the MEX one [35]. Empirical shifting and scaling method were investigated to match the two curves, but this did not induce significant changes in the results.

As discussed in [37], comparing EDAC data coming from different spacecrafts is not straightforward. The solar modulation of GCRs intensity is rigidity-dependent and particle energies causing SEUs might differ from one spacecraft to another, depending on the location of the onboard computer and the device's shielding. However, the similarities between *Rosetta*, *Mars Express* and *Venus Express* in terms of subsystems and memory devices make us confident that the results coming from this empirical approach hold value. Nonetheless it is important to validate this procedure on future missions carrying both EDAC counters and radiation monitors.

5.5 Conclusion

This section was dedicated to the second focus of this thesis: characterizing galactic cosmic rays at the orbit of Venus from EDAC data with the *Venus Express* mission. In particular, the goal was to use the approach developed in [37] and compare MEX, ROS and VEX.

The procedure developed on MEX and ROS was shown to be applicable to VEX as well and yields comparable results, further demonstrating the ability of EDAC counters to describe GCRs intensity variation. This is particularly interesting as it opens up the way to GCRs characterization in places less studied than Earth. The results of this study at Venus indicate a similar solar modulation, with a clear anti-correlation between the EDAC slope and the Sunspots number. They also inform on the time-lag at Venus, which is negligible, suggesting that the solar activity has a near-instantaneous influence on the galactic cosmic rays intensity close to the Sun. The use of EDAC slopes ratio to characterize spatial modulation of GCRs fluxes was also investigated but found inconclusive with the available data.

In order to improve the use of EDAC data, future work will need to accurately describe the internal data processing from the spacecraft and the hardware implementation of the instrument. Moreover, cross-calibration methods between different spacecraft could be used to improve the method. This procedure could be carried out with data acquired on other and future missions, especially the ones like JUICE exploring less known regions of the solar system.

6 Conclusion

This Master Thesis project was dedicated to the characterization of galactic cosmic rays with planetary missions from the *European Space Agency* (ESA). After an introduction on the space radiation environment and the particle-detector interactions in space monitoring, two main studies were conducted in this regard. They were both dedicated to the investigation of an instrument's response to galactic cosmic rays (GCRs) fluxes and allowed to characterize the properties of these engineering and scientific systems.

The focus was initially set on the main mission of interest: ESA's *JUpiter ICy moons Explorer* (JUICE) and in particular its radiation monitor, the *RADiation-hard Electron Monitor* (RADEM). A complete simulation pipeline involving several models was developed in order to characterize the response of the *Heavy-Ion Detector Head* (HIDH) to galactic cosmic rays particle fluxes. `PyCREME`, based on the ISO15390 model, was used to specify the most abundant elements in GCRs fluxes: Helium, Carbon, Nitrogen and Oxygen; and their energy range: $[10^1, 10^3]$ MeV/nucleon. Then, a first order model, `FOCom-PDI`, was developed in `Python3` to get an initial estimate on the response of the HIDH diodes to a straight beam of GCRs particles. This framework implemented a very satisfying approximation of the physical processes involved in the particle detector functioning but was limited to a simple approximation of a GCRs point source. A dedicated CERN-developed software based on Monte-Carlo for particle physics, `Geant4`, was then used to run larger and more complex simulations. The results of these simulations were processed with `ROOT` and `Python3` to investigate the detector's response to cosmic rays fluxes generated by `PyCREME`.

Thanks to these, the field of view, geometric factors and count rates were characterized, together with the influence of the diodes' lower thresholds on them. The conclusions drawn from these results are consistent with the expected values and profiles of the detector's properties. The field of view matches the engineering value of $45°$ and the geometric factors match the theoretical values $0.20\text{cm}^2\cdot\text{sr}$ and $0.15\text{cm}^2\cdot\text{sr}$ for diodes 1 and 2 respectively. However, these conclusions are only valid for particles in a limited energy range, as high energy charged particles can penetrate the collimator of the detector and interact with the diodes without going through the aperture, effectively increasing the number of readings on the detector. This effect was shown to be reduced by an appropriate thresholds configuration such as the one currently in use on the JUICE spacecraft: $t_1 = 52$ DAC, $t_2 = 244$ DAC. Studying the count rates as functions of these thresholds allowed to understand better the number of hits registered on each diode with different thresholds configuration as well. Finally, these computations were extended to a wider range of GCRs fluxes by using `PyCREME` to simulate the solar cycle 24. In particular, this analysis showed that the influence of the solar temporal modulation is more important on the count rates than on the GCRs flux intensity, with a difference between the minimum and maximum values of the count rates of 30% to 60% against 20% for the GCRs fluxes. The spatial modulation was also investigated through an ideal setup which simulated the GCRs fluxes at Venus, Mars and Jupiter from the `PyCREME`-generated flux at Earth. The resulting variation on the count rates matched the expected influence of the theoretical radial gradient $4\%.\text{A U}^{-1}$.

Three types of uncertainties were studied regarding these simulations. Firstly, the choice of the finite energy range $[0.05, 23]$ GeV was justified through stabilization analysis of the detector's properties computed from the simulation outputs. Secondly, the limited number of simulated particles, especially for higher energy ranges, is a significant source of uncertainty for the Monte-Carlo random process. An analysis of the error based on the 95% confidence interval associated to Monte-Carlo simulations was conducted and resulted satisfying for most of the results presented here. These limitations are both linked to the practical constraints that unavoidably come with such complex simulations. Larger simulations with more particles and a wider energy range would have increased the accuracy of the results and the confidence of the conclusions drawn from them. However, they come with an added cost in computation time which had to be taken into account in the limited timeframe of this project. Nevertheless, the results reported in this thesis are satisfying in the context of this thesis. Thirdly, uncertainties on the actual configuration of the HIDH were addressed using an alternative thresholds setting where 0 DAC corresponds to an effective charge threshold of 260 fC. While this change does not affect most of the thresholds configurations used in practice, an accurate documentation of the detector's settings is necessary to confidently describe its properties.

The last section in this thesis was dedicated to another planetary mission: *Venus Express*; and another system: the *Error Detection And Correction* algorithm (EDAC). The procedure developed in this work allowed to reproduce the results found on *Mars Express* and *Rosetta* in [37] and study the temporal and spatial modulation of GCRs from another point of view. The computed EDAC slope exhibited a clear anti-correlation with the solar cycle, further cementing the use of EDACs for galactic cosmic rays characterization. This was especially interesting as the available GCRs data at the Venus orbit is very limited. The results from this analysis suggest that the known time-lag between GCRs intensity and solar activity is negligible at Venus, which is the first conclusion of this kind derived from long-term data at 0.7 A U. The spatial modulation of GCRs fluxes with heliocentric distance was investigated as well but found inconclusive with this data. Additional studies should be conducted to further analyse this property, but the difference in the spacecrafts implementations is considered the most likely cause of uncertainty here. Nevertheless, it is clear that EDAC counters hold some scientific values and that similar studies should be pursued with future missions like JUICE to further investigate them.

In conclusion, this thesis investigated two ways of characterizing GCRs with planetary missions. The first one relied on simulations of particle-detector interactions with a specialized scientific instrument, while the second one involved a more novel analysis of engineering data coming from an instrument dedicated to spacecraft housekeeping. Both allowed to study galactic cosmic rays and their variations in the solar system. The results presented in this thesis should however be validated with further studies. JUICE will arrive to the Jovian system in 2032 and a future mission to Venus might give more insight on the GCRs fluxes closer to the Sun. In the meantime, the considerations described here could be built upon with more advanced simulations. A deeper analysis of the thresholds configuration on RADEM would be useful to set the optimal parameters for the radiation environment at Jupiter, and the novel findings on the time-lag at Venus should be compared with theoretical models to assess their validity within the scientific community.

References

[1] H. Alfvén. Existence of Electromagnetic-Hydrodynamic Waves. *Nature*, 150:405–406, 1942.

[2] Elena Amato. The origin of galactic cosmic rays. *International Journal of Modern Physics D*, 23:1430013, 2014.

[3] Badruddin, Singh, M., and Singh, Y. P. *Astronomy and Astrophysics*, 466:697–704, 2007.

[4] Jean-Loup Bertaux, François Leblanc, Olivier Witasse, Eric Quemerais, Jean Lilensten, S Stern, B Sandel, and O. Korablev. Discovery of an aurora on mars. *Nature*, 435:790–4, 07 2005.

[5] Jeffrey R.S. Brownson. Chapter 03 - laws of light. In Jeffrey R.S. Brownson, editor, *Solar Energy Conversion Systems*, pages 41–66. Academic Press, Boston, 2014.

[6] C. Cardoso. Flight data analysis of the BERM radiation monitor aboard the Bepi-Colombo mission to Mercury, 2022.

[7] CERN. `Geant4`. https://geant4.web.cern.ch/. Accessed: 2023-08-02.

[8] CERN. `ROOT`. https://root.cern/. Accessed: 2023-08-02.

[9] João R. T. de Mello Neto. Ultra high energy cosmic rays: the highest energy frontier. *Journal of Physics: Conference Series*, 706:042009, 2016.

[10] DLR. Mars Express, High Resolution Stereo Camera. Institute of Planetary Research, 2008.

[11] ESA. JUICE factsheet. https://www.esa.int/Science_Exploration/Space_Science/Juice_factsheet. Accessed: 2023-08-02.

[12] ESA. Looking back at the JUICE launch @ ESA mission control. https://esoc.esa.int. Accessed: 2023-08-02.

[13] ESA. Mars Express overview. https://www.esa.int. Accessed: 2023-08-02.

[14] ESA. Rosetta overview. https://www.esa.int. Accessed: 2023-08-02.

[15] ESA. Venus Express overview. https://www.esa.int. Accessed: 2023-08-02.

[16] ESA. JUICE Definition Study Report, 2014.

[17] J. Allison et al. Geant4 developments and applications. *IEEE Transactions on Nuclear Science*, 53:270–278, 02 2006.

[18] J. Allison et al. Recent developments in geant4. *Nuclear Instruments and Methods in Physics Research Section A: Accelerators, Spectrometers, Detectors and Associated Equipment*, 835:186–225, 2016.

[19] J. Fang et al. Understanding the Average Electron–Hole Pair-Creation Energy in Silicon and Germanium Based on Full-Band Monte Carlo Simulations. *IEEE Transactions on Nuclear Science*, 66:444–451, 2019.

[20] J. Pettit et al. Effects of the September 2005 Solar Flares and Solar Proton Events on the Middle Atmosphere in WACCM. *Journal of Geophysical Research: Space Physics*, 123:5747–5763, 2018.

[21] L. Arruda et al. Sep protons in geo measured with the esa multifunctional spectrometer. *IEEE Transactions on Nuclear Science*, 64(8):2333–2339, 2017.

[22] M. Carr et al. Evidence for a subsurface ocean on europa. *Nature*, 391:363–5, 01 1998.

[23] M. Pinto et al. The BepiColombo Environment Radiation Monitor, BERM. *Space Science Reviews*, 218, 09 2022.

[24] Marcelli et al. Helium fluxes measured by the PAMELA experiment from the minimum to the maximum solar activity for solar cycle 24. *The Astrophysical Journal*, 2022.

[25] O. Grasset et al. Jupiter icy moons explorer (juice): An esa mission to orbit ganymede and to characterise the jupiter system. *Planetary and Space Science*, 78:1–21, 2013.

[26] S. Agostinelli et al. Geant4—a simulation toolkit. *Nuclear Instruments and Methods in Physics Research Section A: Accelerators, Spectrometers, Detectors and Associated Equipment*, 506(3):250–303, 2003.

[27] Shirvani et al. Software-Implemented EDAC Protection Against SEUs. *IEEE Transactions on Reliability*, 2000.

[28] V. V. Grechnev et al. An Extreme Solar Event of 20 January 2005: Properties of the Flare and the Origin of Energetic Particles. *Solar Physics*, 252:149–177, 2008.

[29] Y. Futaana et al. Mars Express and Venus Express multi-point observations of geoeffective solar flare events in December 2006. *Planetary and Space Science*, 56:873–880, 2008.

[30] S. E. Forbush. On World-Wide Changes in Cosmic-Ray Intensity. *Phys. Rev.*, 54:975–988, 1938.

[31] Yoshifumi Futaana, Manabu Shimoyama, Martin Wieser, Stefan Karlsson, Herman Andersson, Hans Nilsson, Xiao-Dong Wang, Andrey Fedorov, Nicolas André , Mats Holmström, and Stas Barabash. *The Astrophysical Journal*, 940(2):178, 2022.

[32] Geant4 Collaboration. *Geant4: Book For Application Developers*. CERN, 2022.

[33] George E. Hale, Ferdinand Ellerman, S. B. Nicholson, and A. H. Joy. The Magnetic Polarity of Sun-Spots. *The Astrophysical Journal*, 49:153, 1919.

[34] H.H. Anderson, M.J Berger et al. NIST. https://physics.nist.gov. Accessed: 2023-08-02.

[35] T. Honig, O. G. Witasse, H. Evans, P. Nieminen, E. Kuulkers, M. G. G. T. Taylor, B. Heber, J. Guo, and B. Sánchez-Cano. *Annales Geophysicae*, 37(5):903–918, 2019.

[36] Krishan K. Khurana. Euler potential models of jupiter's magnetospheric field. *Journal of Geophysical Research: Space Physics*, 102:11295–11306, 1997.

[37] E.W. Knutsen, O. Witasse, B. Sanchez-Cano, M. Lester, R. F. Wimmer-Schweingruber, M. Denis, J. Godfrey, and A. Johnstone. Galactic cosmic ray modulation at Mars and beyond measured with EDACs on Mars Express and Rosetta. *Astronomy and Astrophysics*, 650:A165, 2021.

[38] Sergey Koldobskiy, Riikka Kähkönen, Bernhard Hofer, Natalie Krivova, Gennady Kovaltsov, and Ilya Usoskin. *Solar Physics*, 297, 2022.

[39] Yu. A. Kupryakov, A. B. Gorshkov, P. Kotrč, and L. K. Kashapova. Analysis of the Eruptive Event after the Solar Flare of June 7, 2011. *Astronomy Reports*, 65:876–883, 2021.

[40] David J. Lawrence. *Journal of Geophysical Research: Planets*, 122:21–52, 2017.

[41] M. Mays, Barbara Thompson, Lan Jian, Robin Colaninno, Dusan Odstrcil, C. Möstl, M. Temmer, Neel Savani, A. Taktakishvili, P. MacNeice, and Yanqiang Zheng. Propagation of the 7 January 2014 CME and Resulting Geomagnetic Non-Event. *The Astrophysical Journal*, 812, 2015.

[42] A. Mohammadzadeh, H. Evans, P. Nieminen, E. Daly, P. Vuilleumier, P. Buhler, C. Eggel, W. Hajdas, N. Schlumpf, A. Zehnder, J. Schneider, and R. Fear. The ESA Standard Radiation Environment Monitor program first results from PROBA-I and INTEGRAL. *IEEE Transactions on Nuclear Science*, 50:2272–2277, 2003.

[43] N., V. Di Felice, J. Gieseler, M. Boezio, M. Casolino, P. Picozza, B Heber, and PAMELA Collaboration. Latitudinal and radial gradients of galactic cosmic ray protons in the inner heliosphere – PAMELA and Ulysses observations. *Astrophysics and Space Sciences Transactions*, 7:425–434, 2011.

[44] NASA. Gas Giants. https://exoplanets.nasa.gov. Accessed: 2023-08-02.

[45] NASA. Why Space Radiation Matters. https://www.nasa.gov/analogs/nsrl/why-space-radiation-matters. Accessed: 2023-08-18.

[46] E. N. Parker. Dynamical Theory of the Solar Wind. *Space Science Reviews*, 4:666–708, 1965.

[47] E.N. Parker. The passage of energetic charged particles through interplanetary space. *Planetary and Space Science*, 13(1):9–49, 1965.

[48] Parsec vzw. SpaceWeatherLive. https://www.spaceweatherlive.com/en.html.

[49] S. et al. Patsourakos. The Major Geoeffective Solar Eruptions of 2012 March 7: Comprehensive Sun-to-Earth Analysis. *The Astrophysical Journal*, 817:14, 2016.

[50] M. Pinto. *Development of a Directionality Detector and Radiation Hardness Assurance for RADEM, the ESA JUICE mission Radiation Monitor*. PhD thesis, Universidade de Lisboa, 2019.

[51] M. Pinto, P Gonçalves, A. Marques, J. Pinto, and Wiktor Hajdas. Development of a Directionality Detector for RADEM, the Radiation Hard Electron Monitor aboard the JUICE Mission. *IEEE Transactions on Nuclear Science*, PP:1–1, 02 2019.

[52] M. Pinto, C. Poivey, V. Gupta, A. Pesce, M. Poizat, M. Vuolo, and H. Evans. Parametric evaluation of the see rate on the seu and sel monitors aboard the alphasat using the irpp model. *IEEE Transactions on Nuclear Science*, pages 1–1, 2023.

[53] Beatriz. Sanchez-Cano. *Space Weather*, 2023.

[54] G. Santin. Section III: Space Radiation Transport Models. *2014 IEEE NSREC short course notes*, 2014.

[55] A. Savitzky and M. J. E. Golay. Smoothing and differentiation of data by simplified least squares procedures. *Analytical Chemistry*, 36:1627–1639, 1964.

[56] James R. Schwank, Marty R. Shaneyfelt, and Paul E. Dodd. Radiation hardness assurance testing of microelectronic devices and integrated circuits: Radiation environments, physical mechanisms, and foundations for hardness assurance. *IEEE Transactions on Nuclear Science*, 60(3):2074–2100, 2013.

[57] N. Srimanobhas. Introduction to Monte Carlo for Particle Physics Study. CERN Indico, 2010.

[58] Timo A. et al. Stein. Front-end readout ASIC for charged particle counting with the RADEM instrument on the ESA JUICE mission. In *Space Telescopes and Instrumentation 2016: Ultraviolet to Gamma Ray*, volume 9905, page 990546, July 2016.

[59] J.D. Sullivan. Geometric factor and directional response of single and multi-element particle telescopes. *Nuclear Instruments and Methods*, 95:5–11, 1971.

[60] Technical Committee ISO/TC 20. ISO 15390:2004 Space environment (natural and artificial) — Galactic cosmic ray model. https://www.iso.org/standard/37095.html. Accessed: 2023-08-02.

[61] Thoudam, S., Rachen, J. P., van Vliet, A., Achterberg, A., Buitink, S., Falcke, H., and Hörandel, J. R. Cosmic-ray energy spectrum and composition up to the ankle: the case for a second Galactic component . *A&A*, 595:A33, 2016.

[62] Ilya G. Usoskin. A History of Solar Activity over Millennia. *Living Reviews in Solar Physics*, 5, 2008.

[63] J. A. Van Allen. Galactic cosmic ray intensity from 1 to 9 A.U. *Geophysical Research Letters*, 3:425–428, 1976.

[64] J. A. Van Allen. Galactic cosmic ray intensity to a heliocentric distance of 18 AU. *The Astrophysical Journal*, 238:763–767, 1980.

[65] Chin-Chun Wu, Kan Liou, Ronald P. Lepping, and Lynn Hutting. The 04 - 10 September 2017 Sun-Earth Connection Events: Solar Flares, Coronal Mass Ejections/Magnetic Clouds, and Geomagnetic Storms, journal = Springer, Solar Physics. 294:110, 2019.

Appendix A   Acronyms

Several acronyms are used for simplicity in this thesis report. Here are the most important ones with their meaning for reference.

Table 7: Acronyms used in this thesis.

Acronym	Meaning
ASIC	Application-Specific Integrated Circuit
CERN	Conseil Européen pour la Recherche Nucléaire
DAC	Digital Analog Convertor
DDH	Directionality Detector Head
EDAC	Error Detection And Correction
EDH	Electron Detector Head
ESA	European Space Agency
FOV	Field Of View
GCRs	Galactic Cosmic Rays
HIDH	Heavy-Ion Detector Head
ICME	Interplanetary Coronal Mass Ejection
JUICE	JUpiter ICy moons Explorer
MEX	Mars EXpress
NASA	National Aeronautics and Space Administration
PDH	Proton Detector Head
RADEM	RADiation-hard Electron Monitor
ROS	ROSetta
SEPs	Solar Energetic Particles
SEU	Single Event Upset
SREM	Standard Radiation Environment Monitor
SSN	SunSpots Number
VEX	Venus EXpress

Appendix B Simulation files

This appendix reports the files used for the plane source simulations. The *macro* file is the one read by `Geant4` to initialize the simulation parameters, and the `Bash` script was developed to easily run a sequence of simulations with different initialization parameters.

B.1 Macro files

```
 1  ##################################################
 2  #                                                #
 3  #   macro  file  for  Space  Application          #
 4  #                                                #
 5  ##################################################
 6  /tracking/verbose 0
 7
 8  /run/initialize
 9
10  #######################################
11  #                                     #
12  # Primary  generator                  #
13  #                                     #
14  #######################################
15  # Plane  source  position  and  dimensions
16  /gps/position −134 110 5 mm
17  /gps/pos/type  Plane
18  /gps/pos/shape  Rectangle
19  /gps/pos/halfx  25 mm
20  /gps/pos/halfy  25 mm
21  /gps/pos/rot1  1 0 0
22  /gps/pos/rot2  0 0 1
23
24  # Particles  angular  distribution
25  /gps/ang/surfnorm 1
26  /gps/ang/mintheta 0 deg
27  /gps/ang/maxtheta 90 deg
28  /gps/ang/minphi 0 deg
29  /gps/ang/maxphi 360 deg
30
31  # Particle  type
32  /gps/particle ion
33  /gps/ion 7 14 0 0
34
35  # Particles  energy  distribution
36  /gps/ene/type Pow
37  /gps/ene/min  21000 MeV
38  /gps/ene/max  23000 MeV
39  /gps/ene/alpha 0
40
41  ###################
42  #
43  # Run
44  #
45  ###################
46  /mysetrun/SetRunID 20
47  /run/beamOn 10000
```

Listing 5: Macro file used for the plane source simulations.

B.2 Bash script

```bash
#!/bin/bash

#############################
## Help
Help()
{
  # Display help
  echo "Run particle simulations on the HIDH."
  echo "Syntax: run_script [-h|p|P|n|N|m|M|s]"
  ...
}

#############################
## Main program
# Initialize options variables
...

# Read options
while getopts ":h:p:P:n:N:m:M:s:" option; do
   case $option in
      h) # display Help
         Help
         exit;;
      p) # Particle Name
         name_particle=$OPTARG
         ;;
      P) # Nb particles
         nb_particles=$OPTARG
         ;;
      n) # Start index simulations
         start_sim=$OPTARG
         ;;
      N) # End index simulations
         end_sim=$OPTARG
         ;;
      m) # Min energy
         min_energy=$OPTARG
         ;;
      M) # Max energy
         max_energy=$OPTARG
         ;;
      s) # Source shape
         source_shape=$OPTARG
         ;;
     \?) # Invalid option
         echo "${OPTARG} Error: Invalid option"
         exit;;
   esac
done

echo "Running simulations ${start_sim} to ${end_sim} with ${nb_particles}
      ${name_particle} particles from a ${source_shape} source. Energy
     range = ${min_energy} to ${max_energy} MeV."
echo
```

```bash
55  # Select particle
56  Z_particle=1
57  case $name_particle in
58    He)
59      Z_particle=2
60      ;;
61    C)
62      Z_particle=6
63      ;;
64      ...
65  esac
66
67  # Define file path
68  macro_file="macros/General_macros/${source_shape}.mac"
69
70  #### Set simulations parameters in the macro file ####
71  # Particle
72  line_Z_particle="^/gps/ion.*"
73  new_line_Z_particle="/gps/ion ${Z_particle} ${Z_particle_2} 0 0"
74  sed -i "s~$line_Z_particle~$new_line_Z_particle~" $macro_file
75  # Nb particles
76  line_nb_particles="^/run/beamOn.*"
77  new_line_nb_particles="/run/beamOn ${nb_particles}"
78  sed -i "s~$line_nb_particles~$new_line_nb_particles~" $macro_file
79  # Min energy
80  line_min_energy="^/gps/ene/min.*"
81  new_line_min_energy="/gps/ene/min ${min_energy} MeV"
82  sed -i "s~$line_min_energy~$new_line_min_energy~" $macro_file
83  # Max energy
84  line_max_energy="^/gps/ene/max.*"
85  new_line_max_energy="/gps/ene/max ${max_energy} MeV"
86  sed -i "s~$line_max_energy~$new_line_max_energy~" $macro_file
87  # Runid
88  line_run_id="^/mysetrun/SetRunID.*"
89
90  # Start loop
91  for n in $(seq $start_sim 1 $end_sim)
92  do
93      # Replace runid by format
94      new_id=${n}
95      new_line_run_id="/mysetrun/SetRunID ${new_id}"
96      sed -i "s~$line_run_id~$new_line_run_id~" $macro_file
97
98      echo "Starting simulation $n/$end_sim at $(date)"
99      ./Space $macro_file > "Output/Logs/log_$(date)_${new_id}"
100
101     # Move output files to output folder
102     mv HistoFile_r${new_id}.root Output/General_output/${source_shape}/${name_particle}/InvPowLaw/HistoFile_r${new_id}.root
103     mv Space_output${new_id} Output/General_output/${source_shape}/${name_particle}/Space_output${new_id}
104 done
105 echo "Simulations complete, output files have been saved in Output/General_output/${source_shape}/${name_particle}/InvPowLaw/."
```

Listing 6: Bash script used to run multiple simulations.

Appendix C Processing scripts

Several scripts have been written during this thesis to compute all quantities used in the analysis. This appendix reports one of them developed using PyROOT to compute the geometric factor. Note that it was simplified for readability and does not compile in this state.

```python
# Geometry parameters
A_plane = (2*2.5) * (2*2.5) # Plane source area = 25 cm^2
R_aperture = 0.6
A_aperture = np.pi * R_aperture**2
R_diode = 0.6
A_diode = np.pi * R_diode**2
l0 = 2.42 # depth of first diode
l1 = 2.84 # depth of second diode
# Detector parameters
nb_diodes = 2
nb_bins = 500
xlow = 50
xup = 23000
# Thresholds parameters
min_threshold = 0      #fC
max_threshold = 22800 #fC
nb_bits_DAC = 10
min_DAC = 0
max_DAC = 2**nb_bits_DAC - 1
conversion_factor_DAC2fC = (max_threshold - min_threshold)/max_DAC
conversion_factor_charge2energy = (3.6/1.60217663)*10**-2

#### PARTICLES HISTOGRAMS (HIT and INCIDENT)
def compute_histograms_particles_total_hit():
    '''Function used to read the Geant4 output, aggregate it into ROOT
    histograms and convert it to numpy arrays'''

    # Total particles
    hist_total_particles = ROOT.TH1D(particle_name, title, nb_bins, xlow,
    xup)

    # Hit particles
    for n in range(nb_diodes):
        hist_hit_particles.append(ROOT.TH1D(particle_name, title, nb_bins,
    xlow, xup))

    for n in range(start_sim, end_sim+1):
        # Open the ROOT file and recover the relevant information
        SimSpectrum = file.Get("PrimEnergy")

        # Fill histogram with total count
        for i in range(SimSpectrum.GetNbinsX()):
            hist_total_particles.Fill(SimSpectrum.GetBinLowEdge(i),
    SimSpectrum.GetBinContent(i))

        for event in file.Get("RADEM"):
            primary_nrj = event.GetLeaf("fPrimaryEnergy").GetValue()
            deposited_nrjs = event.GetLeaf("fEdepDet")

            for n_det in range(nb_diodes): # Loop through diode detector
```

```
47                      deposited_nrj = deposited_nrjs.GetValue(detectors_idx[
        n_det]) # Get deposited energy by this particle in this detector
48
49                      # Fill histogram with hit count
50                      if (deposited_nrj > energy_cut_offs[n_det]): #cutoff
51                          hist_hit_particles[n_det].Fill(primary_nrj, 1)
52
53              file.Close()
54
55          # Convert to python variables
56          return primary_energies, particles_histograms_array
57
58  #### GEOMETRIC FACTOR
59  def compute_theoretical_geom_fact(index_diode):
60      '''Function used to compute the theoretical geometric factor'''
61      return 1/2 * np.pi**2 * (R_aperture**2 + R_diode**2 + l**2 - np.sqrt
        ((R_aperture**2 + R_diode**2 + l**2)**2 - 4 * R_aperture**2 * R_diode
        **2))
62
63  def compute_geometric_factor(particles_histograms_array):
64      '''Function used to compute the effective geometric factor'''
65      for n_det in range(1, nb_diodes+1): # Loop through each detector
66          for i_bin in range(nb_bins): # Loop through primary energy bins
67              N_channel = particles_histograms_array[n_det][i_bin]
68              N_inc = particles_histograms_array[0][i_bin]
69
70              geometric_factor = A_plane*np.pi*N_channel/N_inc
71              geom_fact_array[n_det-1].append(geometric_factor)
72
73      ### SMOOTHING for low-statistics
74      for n in range(nb_diodes):
75          geom_fact_array[n][10^6:] = savgol_filter(geom_fact_array[n
        ][10^6:], 21, 1)
76
77      return geom_fact_array
78
79  def main():
80      threshold_d1_DAC = 52
81      threshold_d2_DAC = 244
82      compute_energy_thresholds(threshold_d1_DAC, threshold_d2_DAC)
83
84      for particle_name in particle_names:
85          Z_particle = particles_dict[particle_name]
86
87          ##### PARTICLES HISTOGRAMS #####
88          primary_energies, particles_histograms_array =
        compute_histograms_particles_total_hit()
89          #### GEOMETRIC FACTOR #####
90          geom_fact_array = compute_geometric_factor(
        particles_histograms_array)
91
92          prim_nrjs[particle_name] = primary_energies.copy()
93          geom_fcts[particle_name] = geom_fact_array.copy()
```

Listing 7: Simplified PyROOT processing script used to compute the geometric factor from the simulation results.